universitätbonn

2-D Anisotropic Inversion of Frequency-Domain Induced Polarization Data

Dissertation

zur

Erlangung des Doktorgrades (Dr. rer. nat.)

der

Mathematisch-Naturwissenschaftlichen Fakultät

der

Rheinischen Friedrich-Wilhelms-Universität Bonn

vorgelegt von

Johannes Kenkel

aus

Ostercappeln

2018

1. Gutachter: Prof. Dr. A. Kemna,
Fachbereich Geophysik,
Universität Bonn

2. Gutachter: Prof. Dr. J. van der Kruk,
Institute for Bio- and Geosciences,
Forschungszentrum Jülich

Tag der Promotion: 27.7.2017

Erscheinungsjahr: 2018

Contents

List of Figures

List of Tables

Kurzzusammenfassung

Die gemessene Daten des Messverfahrens Induzierte Polarisation (IP) im Zeit- oder Frequenzbereich werden üblicherweise mit Inversionsalgorithmen interpretiert, die auf stochastischen oder iterativen Ansätzen zum Finden eines optimalen, an die Daten angepassten Modells basieren können. Trotz der häufigen Präsenz von Anisotropie in der Natur, beispielsweise auf Grund von Schichtlagerungen oder Rissstrukturen, sind IP-Inversionsalgorithmen typischerweise auf isotrope Zielparameter beschränkt. Als Motivation für die Verwendung einer anisotropen Inversion in der IP werden die Inversionsartefakte präsentiert, die bei Nichtbeachtung von Anisotropie entstehen.

In der vorliegenden Arbeit wird ein auf Anisotropie erweiterter Inversionsalgorithmus für komplexe Leitfähigkeiten präsentiert. Im Laufe der Herleitung wird die Modellierung synthetischer Daten von Modellen mit beliebiger Verteilung der anisotropen komplexen Leitfähigkeiten und beliebigen Elektrodenpositionen wiedergegeben. Der Modellierungsalgorithmus basiert auf der Methode der Finiten Elemente und unterstützt die Diskretisierung in drei- und viereckige Teilbereiche und No-Flow- (Neumann-) sowie Dirichlet-Randbedingungen. Die Sensitivitäten bezüglich anisotroper komplexer Leitfähigkeiten, die für den iterativen Inversionsalgorithmus benötigt werden, werden mit direkter Anwendung auf den Modellierungsalgorithmus präsentiert und gegen eine auf Greenschen Funktionen basierenden analytische Lösung validiert. Mit besonderem Fokus auf die Rekonstruktion von Anisotropie durch einen Inversionsalgorithmus werden verschiedene Sensitivitätsmuster präsentiert. Die für die iterative Inversion grundlegende anisotrope Modellupdatefunktion wird ausführlich dargestellt. In diesem Prozess wird auf die Kostenfunktion für die Behandlung der durch Anisotropie zugewonnenen Freiheitsgrade sowie auf die Implementierung der Updatefunktion eingegangen. Schließlich wird eine synthetische Studie durchgeführt, die die Möglichkeiten des neuen anisotropen Inversionsalgorithmus zur korrekten Modell-Rekonstruktion auf Basis von Daten adressiert und diskutiert, die über isotropen und verschiedenen anisotropen Modellen aufgenommen wurden. Eine Felddemonstration mit einem Vergleich von invertierten und in-situ anisotropen komplexen Leitfähigkeiten wird am Schluss präsentiert.

Die Ergebnisse dieser Arbeit umfassen erfolgreiche und fehlgeschlagene Inversionsszenarien. Unzufriedenstellende Inversionen zeigen sich insbesondere, wenn die Daten nur in einer Dimension – also entlang einer Linie – aufgenommen werden, wobei es unerheblich erscheint, ob an der Oberfläche oder in einem Bohrloch gemessen wird. Erfolgreiche Inversionen zeichnen sich in den präsentierten Beispielen dadurch aus, dass sie aus gemessenen Daten von aus zwei Dimensionen stammen, z.B. zwei parallele Bohrlöcher mit Cross-Borehole-Messungen oder Borehole-to-Surface-Messungen mit senkrecht zueinander stehenden Linien von Messpunkten. Die synthetischen Inversionen zeigen weiterhin, dass die Unterstützung von Anisotropie dazu führen kann, dass Mess-

daten konsistenter interpretiert werden können. So sind sie insbesondere in der Lage, Rekonstruktionen mit geringerem Misfit zwischen Mess- und modellierten Daten sowie mit weniger Artefakten zu erzeugen. Offene Fragen umfassen die Behandlung der durch die Anisotropie in die Inversion eingeführten Mehrdeutigkeit mit drei komplexwertigen Leitfähigkeiten pro Modellzelle statt einer bei Isotropie. Die in dieser Arbeit eingeführte Penaltyfunktion für Anisotropie, die hier manuell nach potentiell subjektiven Kriterien festgelegt wird, sollte in einer zukünftigen Stufe durch einen konsistenten und automatischen Mechanismus festgelegt werden können. Eine weitere offene Frage ist, ob eine erneute anisotrope Auswertung von gemessenen Daten, die bei isotroper Inversion starke Artefakte und einen schlechten Misfit aufweisen (bei guter Datenlage), in der Lage ist, konsistentere Rekonstruktionen zu erzeugen.

Abstract

Measured data in IP (time or frequency domain) are usually interpreted with inversion algorithms, which may be based on stochastic or iterative schemes for finding an optimal data-associated model of the subsurface. Despite the common presence of anisotropy in nature, for example due to layers and fractures, inversion algorithms in IP are usually constrained to isotropic parameters. To support the motivation for anisotropic inversion in IP, it is presented that its neglect leads to inversion artifacts.

This thesis introduces an anisotropy-extended complex conductivity inversion algorithm. In the course of deriving, the modeling of synthetic data from models with arbitrary distributions of anisotropic complex conductivities and arbitrary electrode positions is depicted. The modeling algorithm is based on the method of finite elements and supports discretized triangular and quadrilateral sub-regions and no-flow (Neumann) and Dirichlet boundaries. The sensitivities with respect to anisotropic complex conductivities - which are required by the iterative inversion algorithm - are presented with a direct application to the modeling algorithm and validated analytically with an adapted Greens function. Various sensitivity patterns are shown with a special focus on reconstructing anisotropy in an inversion algorithm. The essential anisotropic model update function for the iterative inversion is delineated and, in this process, penalty functions constraining the additional anisotropy-related degrees of freedom are presented and implemented. Finally, a synthetic study is executed, addressing and discussing the ability of the new anisotropic inversion algorithm to correctly reconstruct corresponding models from data that was recorded over isotropic and various anisotropic models. This thesis also gives a field demonstration that concludes with a comparison of inverted and in-situ anisotropic conductivities

The results of the presented work show successful and failed inversion scenarios. Unsatisfying inversions particularly appear if the underlying measurement data was recorded solely in one dimension (i.e., along one line), albeit insignificant if at the surface or in a borehole. In the presented examples, successful inversions are based on measured data from two dimensions, e.g. two parallel boreholes with cross-borehole measurements or combined surface and borehole setups with borehole-to-surface measurements and perpendicular electrode lines. The synthetic inversions further reveal that anisotropy support may lead to an improved and more consistent interpretation of measured data. Particularly, the anisotropic inversion has the ability to compute reconstructions with less misfit between measured and modeled data as well as with fewer artifacts. Open questions include the treatment of ambiguity that is added through the introduction of anisotropy in the inversion algorithm (i.e., three complex conductivity valued per model cell instead of one in the isotropic case). The also introduced anisotropy penalty function that is configured manually with potentially subjective criteria should be, in a

future step, replaced with a more consistent and automatic mechanism. A further open question is if the anisotropic re-interpretation of already measured data that exhibits strong artifacts and a insufficient model-data misfit in an isotropic inversion (despite good data quality) can improve reconstructions in terms of consistency.

1

Introduction

1.1 Overview

1.1.1 Induced Polarization

Induced Polarization (IP) is a technique that can be utilized for characterizing the subsurface properties in terms of the location and strength of the electrical conductivity and the corresponding polarization. These properties are usually of interest in surroundings with high parameter contrast together with bad accessibility, such as exploration of natural resources like oil, gas or ore deposits (Dakhnov *et al.*, 1952; Bleil, 1953; Marshall & Madden, 1959; Keller & Frischknecht, 1966; Wong & Strangway, 1981; Telford *et al.*, 1990). More recently, IP is used in near-surface applications to characterize hydrogeological systems where empirical relations between IP parameters and the hydraulic conductivity are exploited (see for instance, Kemna *et al.* (2004); Hördt *et al.* (2007)).

Similar to geoelectrics, IP induced an electrical current system in the ground and records the resulting spherical potential distribution. Emerging from this, frequency-domain IP employs an alternating subsurface current system and focuses on the resulting phase shift between injected current and measured potential (see e.g., Telford *et al.* (1990); Knödel (2005)). The measured signal is an electrical impedance alongside with the measurement setup.

1.1.2 Inversion

Traditionally, IP as well as geoelectrics data were interpreted with two- or multi-layer analytical solutions and corresponding *master curves* (DC geoelectrics, e.g., Bhattacharyya & Patra (1968); Keller & Frischknecht (1966) Telford *et al.* (1990, p.539), induced polarization, e.g., Anderson & Keller (1964)) specifically for different measurement setups and layer structures (i.e., number of layers, thickness and contrast). This interpretation is mostly restricted to one-dimensional ”soundings”, e.g., the Schlumberger sounding (see Fig. 1.1) or the Wenner sounding. IP data were interpreted through empirical measures like the (percent) frequency effect, metal factor or chargeability (Marshall & Madden, 1959).

In principle, the 1-D layer interpretation can be utilized for more complex situations, i.e., subsurfaces with varying layer thickness, layer conductivity or even layer quantity. An example is shown in Fig. 1.2, where a geological subsurface interpretation is de-

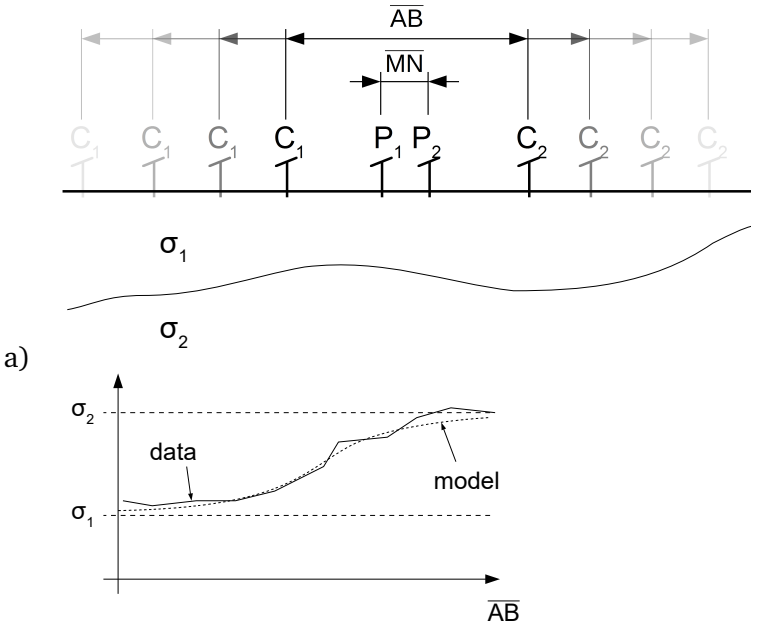

Figure 1.1: a) sketch of a Schlumberger sounding over a two-layer subsurface with σ_1 and σ_2. The potential electrodes P_1 and P_2 are held fixed (distance $\overline{MN}$), the current electrodes C_1 and C_2 are moved outward (distances $\overline{AB}$, in "fading" direction). b) possible Schlumberger sounding data (solid line) and synthetic model for a two-layer case (dotted line). The synthetic model is close to the lower conductivity of the first layer (σ_1) at small distances $\overline{AB}$ and approaches the higher σ_2 at greater distances $\overline{AB}$. Modified after Telford *et al.* (1990)

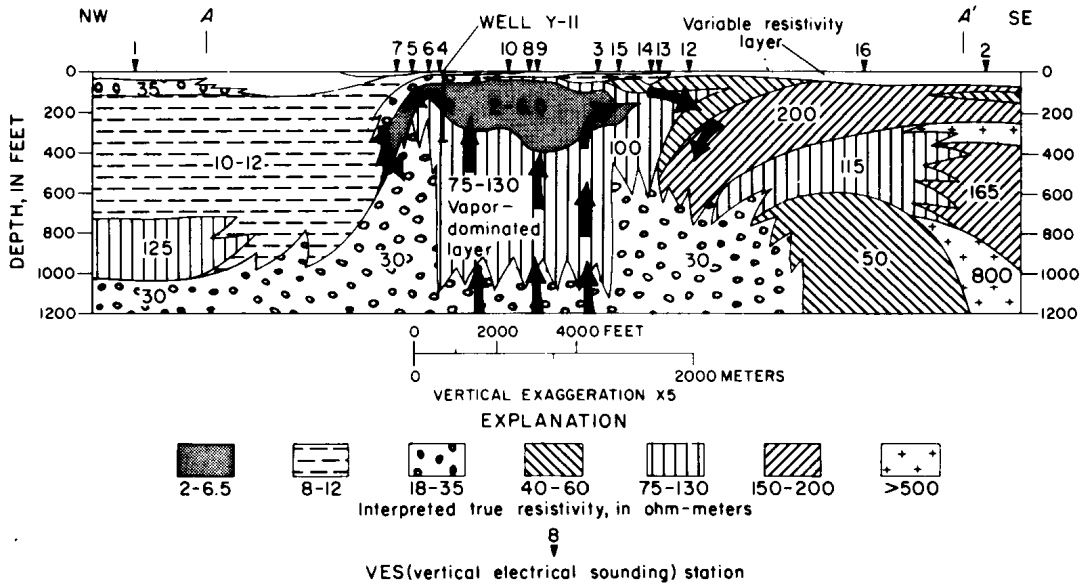

Figure 1.2: Subsurface section of a geothermal system in the Yellowstone National Park, USA. The depicted geological interpretation is based upon 16 Schlumberger vertical soundings. The individual sounding data were fitted to 1-D models. From Zohdy *et al.* (1973).

duced from multiple 1-D fittings of Schlumberger soundings. This approach may lead to artifacts if the important premise of 1-D layers is not met in the targeted area, i.e., due to dipping layers, topography, general non layer-like inhomogeneities. An example of topography effects is shown in Fig. 1.3.

As shown above, the restriction of locally fitting 1-D layers to measured data is the limited ability to accurately resolve 2-D subsurface sections and assign a distribution of the electrical conductivity and polarization. To overcome this, IP data are usually interpreted with inversion algorithms that transform the measured impedances and the geometry information (i.e. the setup) into a spatial distribution of conductivities. To accomplish this, typical inversion algorithms rely on a synthetic modeling algorithm of measurements with respect to a specific measurement configuration and given distribution of the electrical conductivity and the polarization. This algorithm might be an analytical solution for homogeneous half-spaces or 1-D layered media (see e.g., Telford *et al.* (1990)). A computationally more intensive alternative is the application of numerical techniques for solving Poisson's equation (eq. 2.28) for arbitrary conductivity distributions. 2-D conductivity modeling originates to Coggon (1971), who derives the finite element method for geoelectrics and induced polarization. He shows effects of 2-dimensional subsurface anomalies, such as dikes, vertical faults and buried structures (see Fig. 1.3). Usually, synthetic modeled and measured data are then compared to gather an improved conductivity and polarization distribution. Inversion algorithms generally utilize a linearized approach to find the fit of synthetic and measured data, e.g., Ward *et al.* (1974); Jupp & Vozoff (1975); Pelton *et al.* (1978a); Oristaglio & Worthington (1980). The inversion of geoelectrics and IP data is ambiguous (see e.g., Pelton *et al.* (1978a)) and requires the use of *a priori* information (Tikhonov & Arsenin, 1977),

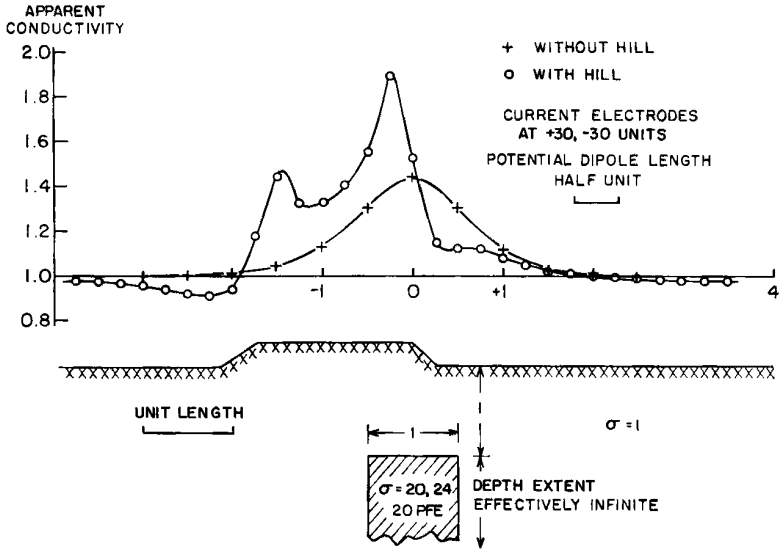

Figure 1.3: Bottom: a dike-like body buried under a surface with topography. Top: simulated "gradient array" apparent conductivity ratios corresponding to the subsurface model either with (o) or without topography (+). From Coggon (1971).

which may be represented through constraints such as smoothness of the model or existence of only few structures/boundaries (Minimum Gradient Support, Portniaguine & Zhdanov (1999); Blaschek (2006)). One version of a smoothness constraint inversion is depicted in LaBrecque *et al.* (1996). This technique uses the principle of Occam's razor* (Occam's inversion as termed by Constable (1987)) stating that, among a variety of possible solutions, the simplest solution is generally better (Baker, 2013). Applied to tomography this implies that only the most necessary structures are to be considered. The inversion problem is generally non-unique, meaning that more than one model may explain a set of data points (see e.g., Parker (1984); Kemna (1995)). This results in the necessity to actively choose a reasonable model. However, the term "reasonable" in this context also is non-unique and requires further definition (see chapter 5. Various choices include the smoothness constraint model (see above) and the minimum gradient support (Portniaguine & Zhdanov (1999)).

The numerical solution of the geoelectrical inversion problem requires the use of partial derivatives of the measured impedances with respect to complex conductivities, which is usually referred to as sensitivities (e.g., Jupp & Vozoff (1975), Kemna (2000)). Depending on the parametrization, the sensitivity contains the response of the measured impedances with respect to perturbations of the complex conductivity in a point, a full or half space or a small volume corresponding to a grid cell. Sensitivities need to be computed for all measurement setups, each implying the computation with respect to all model parameters. An extensible overview was carried out by (McGillivray & Oldenburg, 1990), where they present a review of typical sensitivity computation schemes in the case of isotropic DC (real-valued conductivities) applications. Typically, efficient sensitivity algorithms use the principle of reciprocity, where a swap of current source and potential measurement results in identical measured impedances. In the isotropic

*after William of Ockham (ca. 1287 - 1347).

DC case, the principle of reciprocity was adapted to finite-element modeling (FEM) by Rodi (1976),Tripp *et al.* (1984) and Sasaki (1989). The method was applied to complex conductivity FEM by (Kemna, 2000). In the trivial case of a homogeneous half-space, sensitivities can be expressed analytically (see e.g., Yin & Weidelt (1999); Friedel (2000)).

In the case of models with anisotropic conductivities, the underlying algorithm requires the use of sensitivities with respect to anisotropic conductivities (here *anisotropic sensitivities* as opposed to *isotropic sensitivities*, i.e., sensitivities with respect to isotropic conductivities). In the case of real-valued conductivities (*DC-case*), this problem has been addressed by (Pain *et al.*, 2003; Herwanger *et al.*, 2004). Greenhalgh *et al.* (2009, 2010) conducted a study of anisotropic sensitivities based upon Green's functions that represent the electrical potential field. They use the true source together with the *adjoint* source for the computation.

1.1.3 Anisotropy in Nature

Many materials exhibit anisotropy in their mechanical and electrical properties where the cause can be found at different scales, including molecular anisotropy of minerals such as graphite (e.g., Wallace (1947),see fig. 1.4a), microscopic rock anisotropy, for example due to fractures (e.g., Hill (1972); Zisser & Nover (2009), scale-independent due to distributions of even isotropic rock types (Wong & Strangway, 1981; Winchen *et al.*, 2009), sedimentary (or other) layering, or macro-pores in soils (Moysey & Liu, 2012). The above situations, especially sedimentary layering and fracture zones, occur frequently in natural resource exploration.

Molecular anisotropy occurs at the scale of molecules in the case of non-isotropy, i.e., the composition and/or density of a material is not the same in every direction. One example for this type of anisotropy is graphite, which exhibits strong anisotropic electrical conductivities in crystalline form. Rock and sediment anisotropy is originated in:

- Layering and fractures:
  - Nguyen *et al.* (2007): measurements over a sedimentary fault structure (see fig. 1.4d)). The data were interpreted with synthetic subsurfaces consisting of blocks of thin layers to mimic anisotropy.
  - Moysey & Liu (2012): a system of parallel tubes in a homogeneous background (theoretical study, see fig. 1.4c).
  - Hart & Rudman (1997): measurements in a karst region.
  - J. D. Klein (1997): electrical anisotropy in reservoir beds.
- Texture. A textural composition of the rock material may result in anisotropy. Examples are:
  - Hill (1972): greenstone schist, granite-tourmaline gneiss, graywacke, quartzite
  - Zisser & Nover (2009): sandstone with applied stress in one direction
  - Winchen *et al.* (2009): bimodal material distributions with anisotropic correlation lengths (theoretical study)

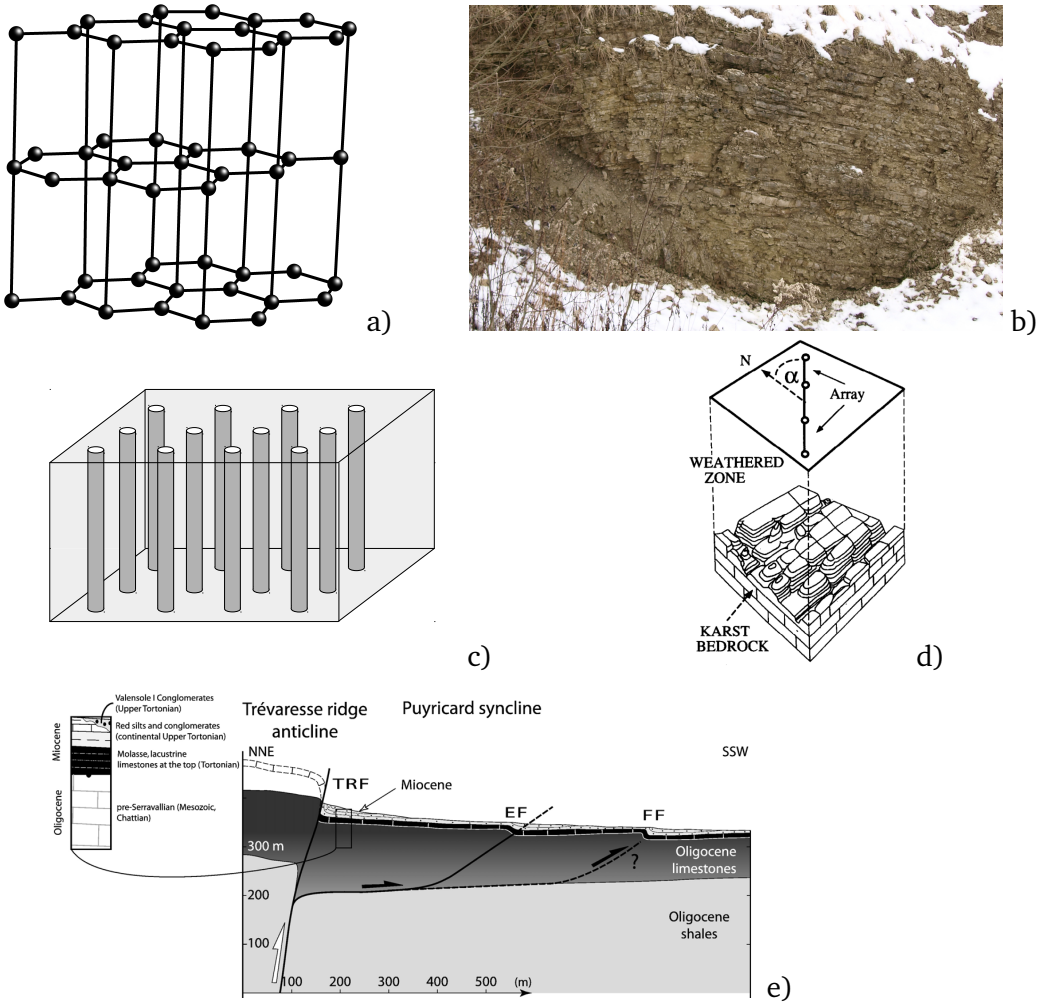

Figure 1.4: a) graphite atomic structure (from Tipler *et al.* (2000)). b) partially folded sedimentary layers. c) macro-scale pores (modified after Moysey & Liu (2012)). d) Karst structure below a weathered zone (from Hart & Rudman (1997)) e) Trévaresse reverse fault (modified after Nguyen *et al.* (2007).

Rock and sediment anisotropy occurs even when the individual materials only exhibit isotropic properties. Consequently, anisotropy may occur in materials that exhibit layers, fractures and/or textures. This implies that anisotropy can be considered ubiquitous in common applications for geoelectrics/IP; thus, its neglect, i.e., the assumption of isotropic material properties, may generally be considered invalid.

Despite the presence of anisotropy, inversion algorithms in geoelectrics and IP are commonly constrained to isotropy (e.g., Günther *et al.* (2006); Johnson *et al.* (2010); Loke *et al.* (2014) for DC resistivity and Kemna (2000); Karaoulis *et al.* (2011) in the case of IP). As mentioned above, anisotropy can be considered a matter of scaling where below a certain scale an isotropic representation may be found, e.g., a fine layering of isotropic materials can lead to anisotropy at a larger scale. However, anisotropy might be necessary due to the weak resolution capability with regard to fine isotropic structures. This becomes crucial especially in conjunction with the widely used smoothness-

constraint inversion schemes smoothing out all small-scale heterogeneity.

1.2 Objectives

The main objective of this thesis is to incorporate anisotropic electrical conductivity and polarization material property (abbreviated to anisotropic conductivity) support into an inversion algorithm. To attain this objective, anisotropic conductivity support needed to be introduced into a forward modeling algorithm (see Kemna (2000); Kenkel *et al.* (2012). Furthermore, linearized gradient information of the synthetic measurement data with respect to the underlying anisotropic conductivity distribution (here sensitivity) needs to be considered to allow for a iterative solution of the ill-posed and non-linear inversion problem (see Kenkel & Kemna (2017)). Because of the added ambiguity due to anisotropy (e.g., more degrees of freedom through horizontal-vertical anisotropy), the final aim of this thesis is to address and discuss anisotropy-constraining methods.

It is beyond this thesis' boundaries to describe the origins of induced polarization data or to interpret this data with regard to their frequency-dependence. A overview on different analytical and empirical models can be found in, e.g., Telford *et al.* (1990); Knödel (2005).

1.3 Thesis Layout

This thesis is outlined as follows:

In chapter 2, the physical fundamentals are laid down in detail starting with introducing the IP measurement principle and common measurement setups. It is followed by a brief summary on the occurrence of anisotropy in nature alongside illustrative examples. Afterwards, the fundamental Poisson equation in its generally anisotropic form is applied to geoelectrics and IP and its validity is discussed. Finally, typical situations with existing analytical solutions are examined.

In chapter 3, the Finite Element modelling of IP measurements over an arbitrary anisotropic subsurface is presented. The chapter covers the application of anisotropy to the Finite Element mechanism and the validation of synthetic computations to certain analytic models.

Chapter 4 introduces and discusses the sensitivity of measured data to alterations of subsurface electrical conductivity.

In chapter 5, the application of anisotropy to the inversion algorithm of Kemna (2000) is presented. The chapter includes a brief history of inversion algorithms with a reference to geophysics. This is followed by the description of the anisotropic forward modeling algorithm. Special focus is put on the sensitivity/linearized gradient section where the computation and the implications of typical sensitivity patterns and simplistic structural subsurface conditions are depicted. Later, the iterative update algorithm is delineated with emphasis on the choice of anisotropy constraint/penalty.

In chapter 6, various examples of inversions of data from synthetic and real-world anisotropic subsurfaces are presented and discussed. The examples include a combined surface and borehole setup with an embedded anisotropic dike structure, a single borehole setup with an embedded anisotropic horizontal layer.

Chapter 7 contains an inversion study of exemplary measured data from the Rollesbroich test site.

In chapter 9, the resolution and restoration capabilities of the newly introduced anisotropic inversion algorithm is discussed.

In chapter 8, a study regarding the performance of the extended inversion algorithm is presented. Here, the potential speed improvements through multi-core parallel code are examined.

The final chapter 10 provides an overall conclusion of this thesis.

2

Induced Polarization

2.1 Geoelectrics

The geoelectrics method relies upon the spatial distribution of currents in a conductive subsurface. This distribution depends on the spatial variation of the subsurface's electrical conductivity. In geoelectrics, current injection and voltage measurement is realized using electrodes; commonly, four-point measurement setups are utilized, i.e., a potential distribution in a target area is created by letting current flow through two electrodes. Two potential electrodes can then be used to record a voltage at a certain location. Exemplary, a classical four-electrode setup is depicted in figure 2.1.

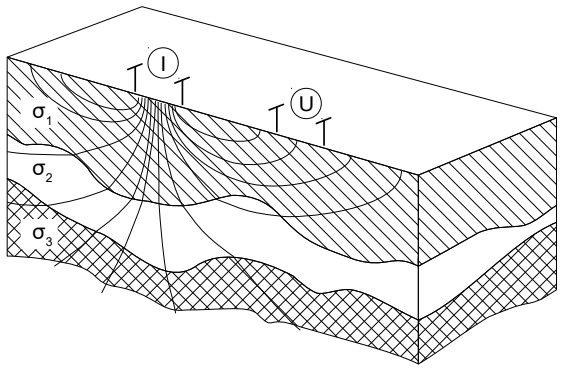

Figure 2.1: Geoelectrics setup: current is injected through two electrodes I and recorded at two other electrodes U. The subsurface conductivities are σ_1, σ_2 and σ_3 in the first, second and third layer. The thin black lines denote lines of constant potential.

2.2 Measurement Setup

Assuming that the measurement in figure 2.2 with four electrodes - two for current injection (C_1 and C_2) and two for voltage measurement (P_1 and P_2) - at the top of a homogeneous half-space, the following relation can be established. Let the potential distribution from equation 2.48 be $\phi = \frac{I}{2\pi\sigma r^2}$, then

$$U = \phi(P_1) - \phi(P_2) = \rho\frac{I}{2\pi}\left(\frac{1}{r_1} - \frac{1}{r_2} - \frac{1}{r_3} + \frac{1}{r_4}\right) \tag{2.1}$$

with the electric current I, the electric conductivity σ and an electrode distance r. Particularly, these distances are: This can be written as

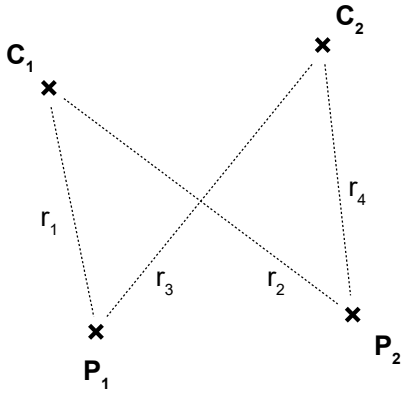

Figure 2.2: Top view of a sketch IP measurement over a homogeneous half space with the current electrodes C_1 and C_2 and the potential electrodes P_1 and P_2.

name	current electrode	potential electrode
r_1	C_1	P_1
r_2	C_2	P_1
r_3	C_1	P_2
r_4	C_2	P_2

$$\begin{aligned}\sigma &= \frac{I}{2\pi U}\left(\frac{1}{r_1} - \frac{1}{r_2} - \frac{1}{r_3} + \frac{1}{r_4}\right) \\ &= \frac{I}{U}k^{-1}\end{aligned} \tag{2.2}$$

with the configuration factor

$$k = 2\pi\left(\frac{1}{r_1} - \frac{1}{r_2} - \frac{1}{r_3} + \frac{1}{r_4}\right)^{-1}. \tag{2.3}$$

The resulting value σ is, in this setting, the conductivity of the corresponding subsurface. However, the conductivity can also be computed for subsurfaces with arbitrary conductivities. In this case, the value is the apparent conductivity σ_a. Due to the dissipative Poisson equation (eq. 2.28), the apparent conductivity is an averaged value which depends on the position of the electrodes and the true conductivity distribution of the subsurface. Due to its location-dependency, a spatial display of surface measurement data can be rendered in a pseudo subsurface section (*pseudo section*). Figure 2.3 shows a basic pseudo section of a dipole-dipole measurement with 8 electrodes. Of all possible intersections, the exemplary points 'a', 'b' and 'c' in figure 2.3 result from the specific configurations in table 2.1.

A pseudo section can be rendered for arbitrary subsurfaces with surface electrodes. It offers a reliable data overview and allows to detect data outliers. Additionally, it allows to detect defective electrodes which, given the case, cause 45° lines in a pseudo section. Commonly, a `skip` value can be used to simulate a larger setup/four-point-configuration. The example `skip-1` then denotes that in the setup of, e.g., a dipole-dipole section, one

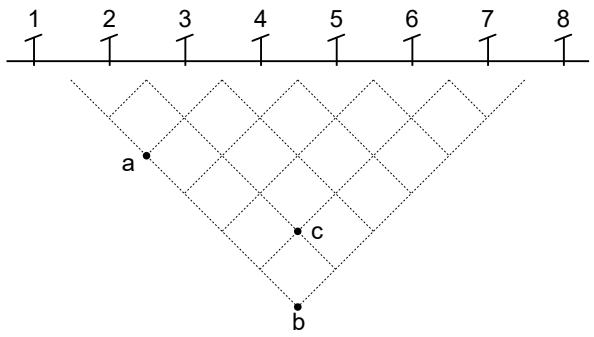

Figure 2.3: Schematic pseudo section structure for a dipole-dipole measurement: at every intersection of the fine-dotted lines a measured value can be assigned (examples 'a','b' and 'c' explained in the text.)

point	$(C_1 - C_2 - P_1 - P_2)$	alternative
a	1-2-3-4	3-4-1-2
b	1-2-7-8	8-7-2-1
c	2-3-6-7	1-4-5-8

Table 2.1: Measurement origins of points 'a','b' and 'c'

electrode between both current injection and voltage measurement dipoles is omitted. Generally, `skip-n` correspondingly omits n electrodes.

2.3 Frequency-Domain Induced Polarization

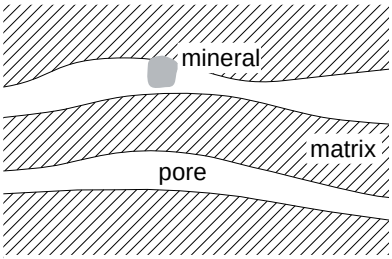

Figure 2.4: Micro-scale ground model with pores with low electrical conductivity in a high-resistive rock matrix. A small mineral is clogging one pore. Modified after (Pelton *et al.*, 1978b).

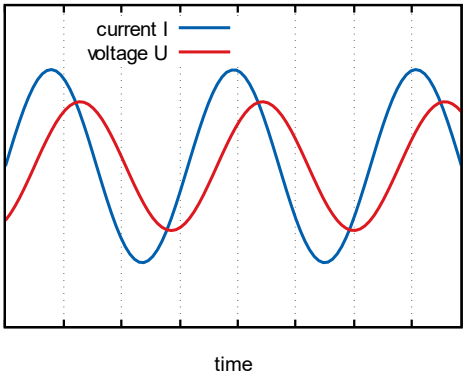

Figure 2.5: Idealized injected current $I(t)$ and recorded voltage $U(t)$ of a typical four-point IP setup at a single frequency plotted as value versus time.

In frequency-domain induced polarization (IP), an alternating current I is injected through current electrodes and a corresponding voltage U is recorded at the potential electrodes (see fig. 2.5). The resulting measurement is the complex-valued impedance

$$Z = \frac{U}{I}$$

with the measured voltage U. The impedance can be written as

$$Z = |Z|e^{i\varphi} \tag{2.4}$$

with the impedance magnitude $|Z|$ and the phase angle φ. If, for example, the recorded signal is influenced by a micro-scale ground similar to fig. 2.4 (meaning that a significant current flows through along the pores), a capacitive effect can become observable as a positive phase difference between measured voltage and injected current (capacitive effect: ”voltage after current”). This principal behavior is usually explained with an equivalent electrical circuit consisting of a parallel connection of a resistor with a series connection of a resistor and a capacitor (see fig. 2.6). Additionally to the described effect, other polarization types were identified and can be found in the literature (see bottom of this section). Figure 2.7 shows an idealized frequency dependence of this principal setup as impedance magnitude and phase angle.

Apart from this very simple model, a commonly utilized empirical model for describing the frequency-dependence of real (non-ideal) IP data is the Cole-Cole model (Cole

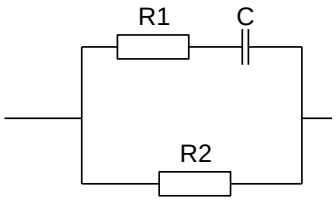

Figure 2.6: Equivalent circuit to describe the frequency dependence of the impedance magnitude and phase angle in fig. 2.7. The model consists of the resistors $R1$ and $R2$ and the capacitor C. Modified after (Pelton *et al.*, 1978b; Bücker, 2011).

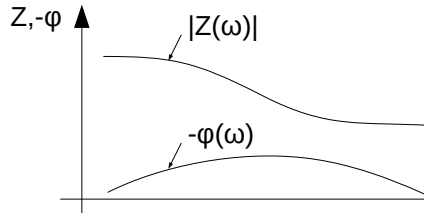

Figure 2.7: Impedance magnitude $|Z|$ and the corresponding impedance phase angle φ versus the measurement frequency ω.

& Cole, 1941). When applied to IP, it describes the impedance Z with respect to the frequency ω (see Pelton *et al.* (1978b)):

$$Z(\omega) = R_0 \left(1 - m \left(1 - \frac{1}{1 + (i\omega\tau)^c}\right)\right) \tag{2.5}$$

with the characteristic parameters

- the DC resistance R_0
- the "chargeability" m
- the frequency ω
- the "time constant" τ
- the "frequency dependence" c.

This section briefly summarized the commonly applied principle of geoelectrics and IP. Since this thesis focuses on the frequency-independent (that is, IP is only regarded at one frequency, see below in section 2.6) modeling and inversion, a detailed introduction to the topics of geoelectrics and IP goes beyond the scope of this thesis. For further information and discussions on the sources of IP, see (Anderson & Keller, 1964; Blaschek, 2006; Bücker, 2011; Knödel, 2005; Marshall & Madden, 1959; Pelton *et al.*, 1978b; Telford *et al.*, 1990; Wong & Strangway, 1981).

2.4 Complex Conductivity

Starting from the complex-valued impedance, Z (eq. 2.4), the geometry-independent material property complex-valued conductivity σ (*complex conductivity*) can be derived.

According to the sketch in fig. 2.8 where current is flowing though a homogeneous cylindrical volume, the complex conductivity may be defined as

$$\sigma = Z^{-1}\frac{L}{A} \tag{2.6}$$

$$= |Z|^{-1}e^{-i\varphi}\frac{L}{A}. \tag{2.7}$$

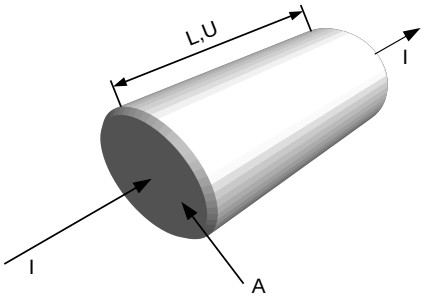

Figure 2.8: Sketch of current I flowing through a homogeneous cylinder with length L, cross-sectional area A and potential difference of front and rear pane U.

Strictly speaking, the complex conductivity may be called *admittivity*, although this term is not commonly used. Since, in this context, mostly complex conductivities are used if not otherwise highlighted, they are abbreviated to *conductivity*.

2.5 Anisotropic Ohm's Law

The general form of Ohm's Law is

$$\vec{j}_C = \underline{\underline{\sigma}}\vec{E}, \tag{2.8}$$

with the electrical conductivity density $\vec{j}_C$ and the electric field $\vec{E}$. The complex conductivity tensor (*admittivity tensor*) $\underline{\underline{\sigma}}$ can be denoted in the general anisotropic case:

$$\underline{\underline{\sigma}} = \begin{pmatrix} \sigma_{xx} & \sigma_{xy} & \sigma_{xz} \\ \sigma_{yx} & \sigma_{yy} & \sigma_{yz} \\ \sigma_{zx} & \sigma_{zy} & \sigma_{zz} \end{pmatrix}. \tag{2.9}$$

In the simple case of anisotropic conductivity due to layering or fractures, the anisotropic conductivity tensor can be composed from a diagonal tensor $\underline{\underline{\sigma}}_d$ that is rotated with corresponding rotation matrices for *yaw*, *pitch* and *roll* angles α, β and γ, i.e.,

$$\begin{aligned} \underline{\underline{\sigma}} &= \begin{pmatrix} \sigma_{xx} & \sigma_{xy} & \sigma_{xz} \\ \sigma_{yx} & \sigma_{yy} & \sigma_{yz} \\ \sigma_{zx} & \sigma_{zy} & \sigma_{zz} \end{pmatrix} \\ &= \begin{pmatrix} \sigma_x & 0 & 0 \\ 0 & \sigma_y & 0 \\ 0 & 0 & \sigma_z \end{pmatrix} \underline{\underline{R}}_x(\alpha)\underline{\underline{R}}_y(\beta)\underline{\underline{R}}_z(\gamma) \end{aligned} \tag{2.10}$$

with

$$\underline{\underline{R}}_x(\phi) = \begin{pmatrix} 1 & 0 & 0 \\ 0 & \cos\phi & -\sin\phi \\ 0 & \sin\phi & \cos\phi \end{pmatrix}$$
$$\underline{\underline{R}}_y(\phi) = \begin{pmatrix} \cos\phi & 0 & \sin\phi \\ 0 & 1 & 0 \\ -\sin\phi & 0 & \cos\phi \end{pmatrix}$$
$$\underline{\underline{R}}_z(\phi) = \begin{pmatrix} \cos\phi & -\sin\phi & 0 \\ \sin\phi & \cos\phi & 0 \\ 0 & 0 & 1 \end{pmatrix}. \tag{2.11}$$

With the above considerations, the exemplary case of rotated layers (i.e., layer direction $\nparallel$ principal direction) can be supported. Figure 2.9 shows the case of rotated layers at the bottom which may be understood through a rotation of the top layer system with a rotation matrix. In terms of conductivity tensors, the top layer system could be characterized with a diagonal matrix $\underline{\underline{\sigma}}_d$ with the three individual conductivities consisting of the horizontal (σ_x and σ_y) and vertical (σ_z) conductivity (see eq. 2.10). Consequently, after rotating this matrix with a rotation matrix, the conductivity tensor is fully populated.

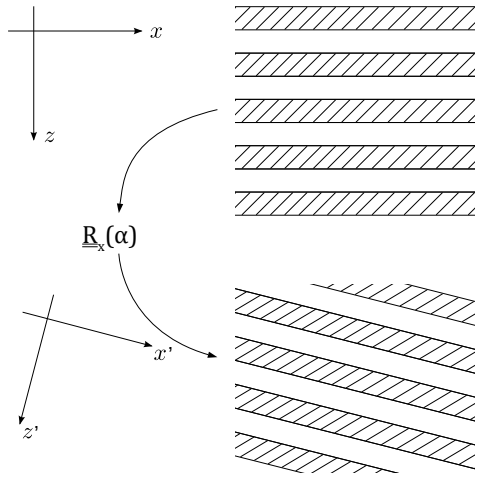

Figure 2.9: Exemplary layering sections. The above layers are parallel to the principal directions, while the bottom layers are rotated. The rotation may be described through a rotation matrix $\underline{\underline{R}}_x(\alpha)$ with the rotation angle α (see eq. 2.11).

Generally, this means that in anisotropic media, the current flow is not necessarily parallel to the excitatory electrical field (see fig. 2.10):

$$\vec{j} = \underline{\underline{\sigma}}\vec{E} \nparallel \vec{E}. \tag{2.12}$$

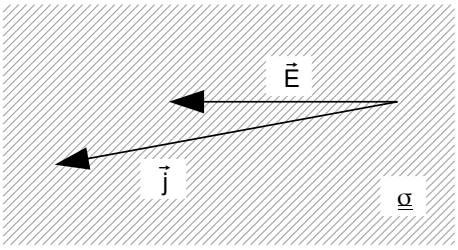

Figure 2.10: Excitatory electrical field $\vec{E}$ and resulting current density $\vec{j}$ in a homogeneous anisotropic medium with high conductivity in vertical direction vs. low conductivity in horizontal direction.

2.6 Poisson Equation

The Poisson equation characterizes the electrical potential distribution in a conductive medium due to injected current. If the assumption of point-sized current injections is applied to the Poisson equation, the potential distributions of single electrodes can be computed. As outlined below, the potential distribution of two current electrodes - i.e., one geoelectrics/IP setup - can be derived through superposition. Consequently, the full geoelectrics/IP measurement can be obtained by evaluating the superposed potential distribution at the locations of the setup's potential electrodes. The following section delineates the derivation of the potential distribution starting with the Maxwell equations in the time-dependent case:

$$rot\ \vec{E} = \nabla \times \vec{E} = -\partial_t \vec{B} \tag{2.13}$$

$$rot\ \vec{H} = \nabla \times \vec{H} = \vec{j} + \partial_t \vec{D} \tag{2.14}$$

$$div\ \vec{D} = \nabla \cdot \vec{D} = \rho_c \tag{2.15}$$

$$div\ \vec{B} = \nabla \cdot \vec{B} = 0. \tag{2.16}$$

Here, the symbols and units are:

- Nabla operator ∇ in $[\mathrm{m}^3]$
- partial time derivative ∂_t in $[\mathrm{s}^{-1}]$
- electric field $\vec{E}$ in $[\mathrm{V\,m}^{-1}]$
- magnetic field $\vec{H}$ in $[\mathrm{A\,m}^{-1}]$
- electric displacement field $\vec{D}$ in $[\mathrm{C\,m}^{-2}]$
- magnetic induction $\vec{B}$ in $[\mathrm{T}]$
- current density $\vec{j}$ in $[\mathrm{A\,m}^{-2}]$
- charge density ρ_c with $[\mathrm{C\,m}^{-3}]$.

The material equations are

$$\vec{D} = \epsilon \vec{E} \tag{2.17}$$

$$\vec{B} = \mu \vec{H} \tag{2.18}$$

Here, $\epsilon = \epsilon_0 \epsilon_r$ is the dielectric permittivity which consists of the vacuum permittivity (vacuum dielectric constant) $\epsilon_0 = 8.85 \times 10^{-12}\mathrm{As/Vm}$ and (material-dependent) relative permittivity ϵ_r in a typical range from 0 to 80. The parameter $\mu = \mu_0 \mu_r$ is the magnetic permeability and $\mu_0 = 4\pi \times 10^{-7}\mathrm{H\,m}^{-1}$ and μ_r is the relative permeability.

Beginning with the continuity equation,

$$\nabla \vec{j} = 0, \tag{2.19}$$

the right side of equation 2.14 can be written as

$$\begin{aligned} \vec{j} + \partial_t \vec{D} &= \vec{j} + \epsilon \partial_t \vec{E} \\ &= \vec{j}_S + \vec{j}_C + \vec{j}_D. \end{aligned} \tag{2.20}$$

Here, $\vec{j}_S$ denotes the source term of the current density distribution. The term $\vec{j}_C$ specifies the convective currents with Ohm's law (see section 2.5):

$$\vec{j}_C = \underline{\underline{\sigma}} \vec{E}, \tag{2.21}$$

where $\underline{\underline{\sigma}}$ is the complex conductivity tensor (see eq. 2.9) that is related to the complex anisotropic resistivities (i.e., anisotropic *impeditivities*) $\rho_{ij}, (i,j) \in \{x,y,z\}$, whereby

$$\rho_{ij} = |\rho_{ij}| \, \mathrm{e}^{i\phi_{ij}} \, . \tag{2.22}$$

The complex-valued anisotropic resistivities are related to the complex conductivities via

$$\underline{\underline{\rho}} = \underline{\underline{\sigma}}^{-1}. \tag{2.23}$$

The term $\vec{j}_D = \epsilon \partial_t \vec{E}$ denotes the displacement currents.

The complex anisotropic resistivities contain a phase shift between the current flow, $\vec{j}_C$, and the excitatory electric field $\vec{E}$.

In the limit case of very low frequencies (and thus large periodic time), the displacement currents $\vec{j}_D$ are vanishing since $\lim_{f \to 0} \partial_t \vec{E}(t) = 0$. Therefore, the electric field in the limit case of low frequencies is a potential field, imposing a vanishing curl $\nabla \vec{E}$.

Let $\vec{E} \propto \mathrm{e}^{i\omega t}$ be a periodic electrical field with a frequency ω, then the ratio of $\vec{j}_C$ and $\vec{j}_D$ can be examined. With the additional constraint of small phase shifts between transmitting and receiving signal, this results in

$$\begin{aligned} \frac{|\vec{j}_C|}{|\vec{j}_D|} &= \frac{|\vec{E}|}{\rho \epsilon |\partial_t \vec{E}|} \\ &= \frac{1}{\rho \epsilon \omega}. \end{aligned} \tag{2.24}$$

Typical threshold values in frequency-domain IP are $\rho = 100 \Omega\,\mathrm{m}$, $\epsilon = 80 \cdot \epsilon_0$ and $\omega = 2\pi \cdot 1000\mathrm{Hz}$. Inserting this into equation 2.24 produces

$$\frac{|\vec{j}_C|}{|\vec{j}_D|} = 2 \cdot 10^3 \gg 1. \tag{2.25}$$

Therefore, displacement currents can be neglected in typical frequency-domain IP.

The continuity equation 2.19 becomes

$$\begin{aligned} \nabla \vec{j} = \nabla(\vec{j}_S + \vec{j}_C) &= 0 \\ \Leftrightarrow \nabla \vec{j}_C &= -\nabla \vec{j}_S. \end{aligned} \tag{2.26}$$

Now, let the source currents be inserted through a point electrode at (x_0, y_0, z_0). In this case and with Ohm's law (equation 2.21), it follows that

$$\begin{aligned} \nabla\vec{j_S} &= I\delta(x-x_0)\delta(y-y_0)\delta(z-z_0) \\ \nabla\vec{j_C} &= -\nabla(\underline{\underline{\sigma}}\nabla\phi). \end{aligned} \tag{2.27}$$

Merging this with eq. 2.26 results in the Poisson equation, which is an elliptical second order partial differential equation:

$$\nabla(\underline{\underline{\sigma}}\nabla\phi) = I\delta(x-x_0)\delta(y-y_0)\delta(z-z_0). \tag{2.28}$$

This equation is identical for DC geoelectrics and frequency-domain IP. Generally, solutions for arbitrary anisotropic conductivity distributions can only be computed numerically. However, a number of solutions exist for special simple cases.

2.6.1 Homogeneous Space

In this case, the point electrode is considered to be within a space of uniform and isotropic complex conductivity σ_0. The Poisson equation 2.28 can then be simplified:

$$\sigma \cdot \nabla\nabla\phi = I\delta(x-x_0)\delta(y-y_0)\delta(z-z_0).$$

In this case the electrical potential only varies in the radial component (see figure 2.11)

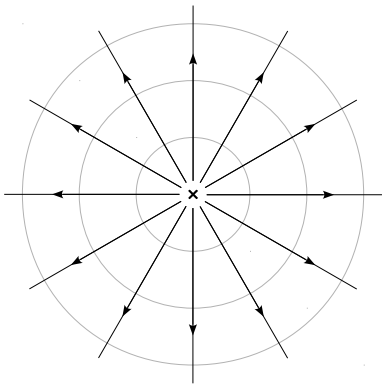

Figure 2.11: Electrical field lines (black with arrows) of a point current source (x) in a homogeneous space. The gray lines depict a constant potential surface.

if the coordinate origin is the current injection point. In polar coordinates:

$$\sigma\nabla\nabla\phi = \sigma\cdot(\frac{\partial^2\phi}{\partial r^2} + \frac{2}{r}\frac{\partial\phi}{\partial r}) = I\delta(x-x_0)\delta(y-y_0)\delta(z-z_0). \tag{2.29}$$

Integrating the homogeneous equation equals

$$\sigma\frac{\partial\phi}{\partial r} = \frac{C_1}{r^2} \tag{2.30}$$

with the solution

$$\phi = \frac{1}{\sigma}(-\frac{C_1}{r} + C_2). \tag{2.31}$$

Due to the boundary condition $\phi(r\to\infty) = 0$, the term $C_2 = 0$ and hence,

$$\phi = \frac{1}{\sigma}\frac{C_1}{r}. \tag{2.32}$$

The constant C_1 depends on the total current I that is injected through the point electrode. Consider the current density $\vec{j_C}$ through the surface of a sphere A:

$$\begin{aligned} I &= \int \vec{j_C} d\vec{A} = \int \vec{j_C} \cdot \vec{e}_r \cdot r^2 \sin(\theta) d\varphi \, d\theta \\ I &= 4\pi r^2 |\vec{j_C}| \\ I &= 4\pi r^2 (|\sigma \nabla \cdot \phi|) \\ I &= 4\pi r^2 (\sigma \frac{\partial \phi}{\partial r}) \\ I &= 4\pi C_1 \\ C_1 &= \frac{I}{4\pi} \end{aligned} \tag{2.33}$$

Inserting this into equation 2.32 results in

$$\phi = \frac{1}{\rho} \frac{I}{4\pi r}. \tag{2.34}$$

This implies that the electrical potential ϕ is inverse proportional to the distance to the source point.

2.6.2 Homogeneous Half-Space with Isotropic Conductivity

Let a point current electrode reside at the surface of a body that extends infinitely to the left, the right, the front, the back and to the depth (see figure 2.12. The Poisson equation

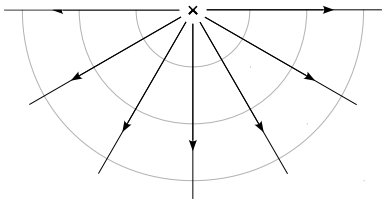

Figure 2.12: Electrical field lines (black with arrows) of a point current source (x) in a homogeneous half-space. The gray lines depict a constant potential surface.

$$\begin{aligned} \nabla(\sigma \nabla \phi) &= I\delta(x - x_0)\delta(y - y_0)\delta(z - z_0) \\ \Leftrightarrow (\nabla\sigma)(\nabla\phi) - \sigma(\nabla\nabla\phi) &= I\delta(x - x_0)\delta(y - y_0)\delta(z - z_0) \end{aligned} \tag{2.35}$$

may then be evaluated with two conductivities, σ_1 and σ_2. Outside of the boundary, $\nabla \cdot \sigma = 0$ and therefore

$$\sigma \nabla \nabla \phi \equiv \Delta \phi = I\delta(x - x_0)\delta(y - y_0)\delta(z - z_0) \tag{2.36}$$

with the well-known solution

$$\phi = \frac{C_1}{\sigma r}. \tag{2.37}$$

At the boundary itself, the current in z direction has to be constant on both sides, $j_{1,z} = j_{2,z}$. With

$$j_{1,z} = -\sigma_1 \cdot E_{1,z} \tag{2.38}$$

$$j_{2,z} = -\sigma_2 \cdot E_{2,z} \tag{2.39}$$

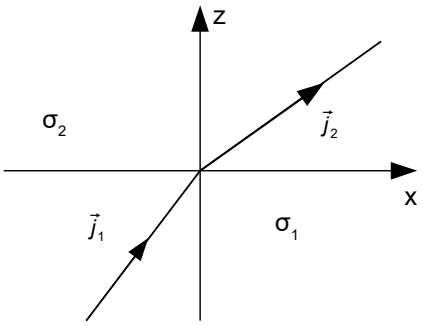

Figure 2.13: Current lines at a conductivity boundary between σ_1 and σ_2.

it follows that

$$E_{2,z} = \frac{\sigma_1}{\sigma_2} \cdot E_{1,z}. \tag{2.40}$$

If $\sigma_2 = 0$ and $\sigma_1 > 0$, $E_{2,z}$ cannot diverge. This is satisfied by

$$E_{1,z} = 0. \tag{2.41}$$

With the electric field perpendicular to the boundary being zero, it follows that all current that is injected flows symmetrically through half-sphere surfaces:

$$\begin{aligned}
I = &\int \vec{j} d\vec{A} = \int \vec{j} \cdot \vec{e}_r \cdot r^2 \sin(\theta) d\varphi \, d\theta && (2.42)\\
I = &\quad 2\pi r^2 |\vec{j}| && (2.43)\\
I = &\quad 2\pi r^2 |\sigma_1 \nabla \cdot \phi| && (2.44)\\
I = &\quad 2\pi r^2 \sigma_1 \tfrac{\partial \phi}{\partial r} && (2.45)\\
I = &\quad 2\pi C_1 && (2.46)\\
&\quad C_1 = \tfrac{I}{2\pi}. && (2.47)
\end{aligned}$$

Finally, ϕ becomes

$$\phi = \frac{1}{\sigma_1} \frac{I}{2\pi r} \tag{2.48}$$

in the case of a homogeneous half-space.

2.6.3 Homogeneous Half-Space with Anisotropic Conductivity (Horizontal-Vertical)

According to Telford *et al.* (1990), the analytical potential distribution in a homogeneous anisotropic half-space with the conductivity σ_h in horizontal and σ_v in vertical direction can be expressed as

$$\begin{aligned}
\phi &= \frac{I}{2\pi \sqrt{\sigma_h \cdot \sigma_v} r} \\
&= \frac{I}{2\pi \overline{\sigma} r}.
\end{aligned} \tag{2.49}$$

In this case, an averaged conductivity is built with the square root of horizontal and vertical conductivity, $\overline{\sigma} = \sqrt{\sigma_h \cdot \sigma_v}$. Mainly, it follows that the potential distribution at the surface of an anisotropic subsurface cannot be distinguished from the signal over an equivalent isotropic subsurface.

2.7 Mixing Laws for Thin Layers *

This section addresses the calculation of equivalent complex anisotropic conductivity for layered isotropic media, represented as conductivity tensor $\underline{\underline{\sigma}}$. The layering direction is assumed to be aligned with the x-y-z coordinate system, corresponding to either horizontally or vertically layered structures. With this assumption, the complex conductivity tensor is

$$\underline{\underline{\sigma}} = \begin{pmatrix} \sigma_{xx} & \sigma_{xy} & \sigma_{xz} \\ \sigma_{yx} & \sigma_{yy} & \sigma_{yz} \\ \sigma_{zx} & \sigma_{zy} & \sigma_{zz} \end{pmatrix} \tag{2.50}$$

with vanishing off-diagonal elements. The next assumption is that the material consists only in two different electrical layer types each with an isotropic complex conductivity, i.e., σ_1 and σ_2. This is only a minor limitation since the theory may easily be extended to support more than two conductivities. For simplicity, the equations are discussed for the case where all layers have the same thickness. The general case with different thicknesses holds no significant additional information and is delineated in the appendix in Kenkel *et al.* (2012). The complex anisotropic conductivity can be computed considering a serial and respective a parallel circuit (Fig. 2.14). A direction perpendicular to

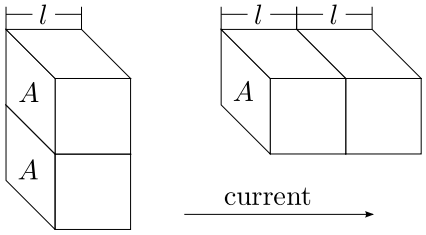

Figure 2.14: Sketch of the model used to calculate the anisotropic conductivities. The conductivity in the horizontal direction is calculated either assuming the two blocks are in series or in parallel.

the layer orientation (e.g., the vertical direction in a horizontally layered structure) can be conceptualized with two blocks with complex conductivities σ_1 and σ_2, length l and cross-sectional area A resulting in a series connection with length $2l$ and cross-sectional area A. Similarly, a direction parallel to the layer orientation (e.g., one of the horizontal directions in a horizontally layered structure, the left side of Fig. 2.14) can be considered as a parallel connection of the blocks with σ_1 and σ_2 resulting in a block with length l and a cross-sectional area $2A$.

Let the effective complex conductivity in one direction be σ, e.g., σ_x, with

$$\sigma = |\sigma| \, \mathrm{e}^{-i\varphi},$$

where i is the imaginary unit with $i^2 = -1$, σ is the conductivity magnitude and φ denotes the negative phase of the complex conductivity (i.e., the phase of the complex resistivity). A convention in this work is to abbreviate the complex conductivity in the form

$$\begin{aligned} \sigma &= |0.1\text{S/m}| \, \mathrm{e}^{i5\text{mrad}} \\ &\stackrel{\text{def}}{=} \{0.1 \text{ S/m}, 5 \text{ mrad}\}. \end{aligned} \tag{2.51}$$

*The sections 2.7, 2.7.1 and 2.7.2 are adapted from Kenkel, J., Hördt, A., & Kemna, A. 2012. 2D modelling of induced polarization data with anisotropic complex conductivities. *Near Surface Geophysics*, **10**(6), 533–544.

The complex conductivity σ is related to the complex resistivity ρ of a block with length l, cross-sectional area A and impedance Z according to

$$\rho = \frac{1}{\sigma} = Z\frac{A}{l}.$$

A series connection of two complex resistivities, ρ_1 and ρ_2, representing the direction perpendicular to the layers, leads to the complex resistivity

$$\rho_\perp = \tfrac{1}{2}\left(\|\rho_1\|\,\mathrm{e}^{i\varphi_1} + \|\rho_2\|\,\mathrm{e}^{i\varphi_2}\right). \tag{2.52}$$

Complex resistivity phase values of soils and rocks are usually small compared to 1 (e.g. (Pelton *et al.*, 1978b)), so that the approximations $\cos\varphi \approx 1$ and $\sin\varphi \approx \varphi$ can be applied, leading to

$$\rho_\perp \approx \tfrac{1}{2}\left(\rho_1\rho_2 + i\rho_1\varphi_1 + i\rho_2\varphi_2\right) = \rho_\perp\,\mathrm{e}^{i\varphi_\perp} \tag{2.53}$$

with

$$\begin{aligned}\rho_\perp &= \frac{\rho_1 + \rho_2}{2}\\ \varphi_\perp &= \frac{\rho_1\varphi_1 + \rho_2\varphi_2}{\rho_1 + \rho_2}\end{aligned} \tag{2.54}$$

Here, $\rho_\perp$ is the magnitude of the effective complex resistivity and $\varphi_\perp$ is its phase, which is the average value of φ_1 and φ_2 weighted by the magnitudes ρ_1 and ρ_2.

The corresponding complex resistivity parallel to the layers can be calculated via a parallel circuit of the complex resistivities ρ_1 and ρ_2.

$$\rho_\parallel = 2\left(\frac{1}{\rho_1\,\mathrm{e}^{i\varphi_1}} + \frac{1}{\rho_2\,\mathrm{e}^{i\varphi_2}}\right)^{-1}. \tag{2.55}$$

After some algebra, (one obtains)

$$\rho_\parallel \approx 2\left(\frac{1}{\rho_1} + \frac{1}{\rho_2}\right)^{-1}\,\mathrm{e}^{\,i\left(\frac{1}{\frac{1}{\rho_1}+\frac{1}{\rho_2}}\left(\frac{\varphi_1}{\rho_1}+\frac{\varphi_2}{\rho_2}\right)\right)} \tag{2.56}$$

with

$$\begin{aligned}\rho_\parallel &= 2\left(\frac{1}{\rho_1} + \frac{1}{\rho_2}\right)^{-1}\\ \varphi_\parallel &= \left(\frac{1}{\frac{1}{\rho_1}+\frac{1}{\rho_2}}\left(\frac{\varphi_1}{\rho_1} + \frac{\varphi_2}{\rho_2}\right)\right).\end{aligned} \tag{2.57}$$

Here, $\rho_\parallel$ is the magnitude of the effective complex resistivity parallel to the layers and $\varphi_\parallel$ is its phase, again being the weighted average of the individual phase values, but this time weighted by the inverse magnitude values. For both the parallel and perpendicular directions, corresponding to parallel and serial connections, the magnitude mixing works like in the DC case where the effective magnitude only depends on the two magnitudes of layers 1 and 2. In contrast, the effective phase values depend on both the magnitude and phase of media 1 and 2 and are computed as a magnitude weighted phase average. Since the consideration is independent of the rotation of the anisotropic media with respect to the surface, the conclusion holds also for arbitrary directions, i.e., full-complex conductivity tensors, provided they are equivalent to layering.

To understand the nature of these mixing laws, two special cases are discussed below: homogeneous magnitudes and homogeneous phases.

2.7.1 Homogeneous Phase Angles

In case of equal phase angles for both layers, $\varphi = \varphi_1 = \varphi_2$, equations 2.53 and 2.56 can be simplified:

$$\rho_\perp = \frac{\rho_1 + \rho_2}{2} \, \mathrm{e}^{i\varphi} \tag{2.58}$$

and

$$\rho_\parallel = \frac{2}{\rho_1^{-1} + \rho_2^{-2}} \, \mathrm{e}^{i\varphi} \tag{2.59}$$

where ρ_1 and ρ_2 are the magnitudes of layers 1 and 2. This implies that in case of equal phase angles in all layers, the magnitude-averaging is independent of the phase angle.

2.7.2 Homogeneous Magnitudes

Another case is given by homogeneous magnitudes and different phase angles. In this case, equations 2.53 and 2.56 can be simplified as follows:

$$\rho_\perp = \rho \, \mathrm{e}^{i\frac{\varphi_1+\varphi_2}{2}} \tag{2.60}$$

and

$$\rho_\parallel = \rho \, \mathrm{e}^{i\frac{\varphi_1+\varphi_2}{2}} \, . \tag{2.61}$$

This result (equations 2.60 and 2.61) is remarkable, since it implies that phase angles are calculated in the same way for both the parallel and perpendicular directions. This means that independent of the individual phase angles φ_1 and φ_2, the anisotropic phase is indistinguishable from isotropic phases with

$$\frac{\varphi_1 + \varphi_2}{2}. \tag{2.62}$$

Consequently, if one assumes anisotropy to be caused by sequences of thin layers, an anisotropic phase can only occur if the resistivity magnitude shows anisotropy. The mixing laws change slightly if we give up the assumption of small phase values:

$$\rho_\perp = \rho \cos\left(\frac{\varphi_1 + \varphi_2}{2}\right) \mathrm{e}^{i\frac{\varphi_1+\varphi_2}{2}} \tag{2.63}$$

$$\rho_\parallel = \frac{\rho}{\cos\left(\frac{\varphi_1+\varphi_2}{2}\right)} \, \mathrm{e}^{i\frac{\varphi_1+\varphi_2}{2}} \tag{2.64}$$

Again, the phase angles are averaged identically for the parallel and perpendicular directions and thus no anisotropy can be resolved. It is important to note that at large phase angles, the magnitude is no longer independent of the phase angle. However, in geophysical applications, phase shifts of $-100\,\mathrm{mrad}$ are already considered large. If one assumes for example $\varphi_1 = -100\,\mathrm{mrad}$ and $\varphi_2 = -20\,\mathrm{mrad}$, we obtain a magnitude decrease of 0.2%, i.e., this effect is very small.

3

Modeling

3.1 Anisotropy in Principal Directions

For simplicity, the conductivity tensor is restricted to its diagonal elements in the modeling algorithm:

$$\underline{\underline{\sigma}} = \begin{pmatrix} \sigma_x & 0 & 0 \\ 0 & \sigma_y & 0 \\ 0 & 0 & \sigma_z \end{pmatrix}. \tag{3.1}$$

The full tensor conductivity is then available through a rotation of the corresponding coordinate system. With this, the Poisson equation (eq. 2.28),

$$\nabla(\underline{\underline{\sigma}}\nabla\phi) = I\delta(x - x_0)\delta(y - y_0)\delta(z - z_0), \tag{3.2}$$

may be written explicitly as

$$\begin{aligned} &\partial_x(\sigma_x\partial_x\phi) + \partial_y(\sigma_y\partial_y\phi) + \partial_z(\sigma_z\partial_z\phi) + I\delta(x - x_s)\delta(y - y_s)\delta(z - z_s) = 0 \\ \Leftrightarrow\ &(\partial_x\sigma_x)(\partial_x\phi) + \sigma_x\partial_x^2\phi + (\partial_y\sigma_y)(\partial_y\phi) + \sigma_y\partial_y^2\phi + (\partial_z\sigma_z)(\partial_z\phi) + \sigma_z\partial_z^2\phi \\ &\qquad + I\delta(x - x_s)\delta(y - y_s)\delta(z - z_s) = 0. \end{aligned} \tag{3.3}$$

3.2 2.5-D Space

One common branch of IP measurements utilizes line-style setups with (assumed) point electrodes. Until this point in this thesis, the Poisson equation is three-dimensional with a three-dimensional potential distribution and a three-dimensional conductivity distribution. However, in many scenarios, only 2 dimensions are of interest, either because of the assumed conductivity distribution or because of the applied measurement setup. Typical claims include the geological assumed structures (faults, layers, etc.), which are continuous at least in one dimension. In this case, the number of "free" dimensions is reduced at least by 1, resulting in a (max.) two-dimensional parameter space. A side effect of this is the possibility to eliminate one dimension from the modeling algorithm, which greatly reduces its computational needs. The assumption of a constant conductivity in y

direction can be exploited with a Fourier transform to a "wave-number" space:

$$\begin{aligned} F(k) &= \int_{-\infty}^{\infty} f(y) e^{iky} dy \\ &= \int_{-\infty}^{\infty} f(y) \cos(ky) dy + i \int_{-\infty}^{\infty} f(y) \sin(ky) dy. \end{aligned}$$

Assuming a symmetrical function in y direction due to a point current source electrode at $y = 0$, the sine function vanishes, resulting in

$$F(k) = \int_{-\infty}^{\infty} f(y) \cos(ky) dy. \tag{3.4}$$

The transformation of eq. 3.3 into the Fourier space leads to (detailed derivations in Appendix A)

$$\begin{aligned} &\partial_x \sigma_x \partial_x \widetilde{\phi}(k) + \sigma_x \partial_x^2 \widetilde{\phi}(k) - \sigma_y k^2 \widetilde{\phi}(k) + \partial_z \sigma_z \partial_z \widetilde{\phi}(k) + \sigma_z \partial_x^2 \widetilde{\phi}(k) \\ &\qquad + \frac{I}{2} \delta(x - x_s) \delta(z - z_s) = 0 \\ \Leftrightarrow\ &\partial_x (\sigma_x \partial_x \widetilde{\phi}(k)) - \sigma_y k^2 \widetilde{\phi}(k) + \partial_z (\sigma_z \partial_z \widetilde{\phi}(k)) + \frac{I}{2} \delta(x - x_s) \delta(z - z_s) = 0. \end{aligned} \tag{3.5}$$

The resulting equation is a Helmholtz-type equation. Here, the value $\widetilde{\phi}$ is the electrical potential in the Fourier space. It may be transformed to the real space with the Fourier backward transformation according to eq. 3.4.

3.3 Finite Element Method

The Poisson equation (eq. 2.28) as well as the corresponding Helmholtz equation (eq. 3.5) cannot be solved analytically for arbitrary conductivity distributions. The finite element method solves partial differential equations on complex geometries. It is based on the calculus of variations (e.g., Courant & Hilbert (1924); Courant *et al.* (1943)). This particular finite element approach follows Schwarz (1991b,a) and extends it to the modeling of anisotropic conductivities. The notation is closely related to Kemna (2000); Kenkel (2011), albeit with a special focus on anisotropic complex conductivities.

The target equation is eq. 3.5,

$$\partial_x (\sigma_x \partial_x \widetilde{\phi}(k)) - \sigma_y k^2 \widetilde{\phi}(k) + \partial_z (\sigma_z \partial_z \widetilde{\phi}(k)) + \frac{I}{2} \delta(x - x_s) \delta(z - z_s) = 0 \tag{3.6}$$

with a condition on the function domain's boundary,

$$\sigma_x \partial_x \widetilde{\phi} + \sigma_y \partial_y \widetilde{\phi} + \sigma_z \partial_z \widetilde{\phi} + \beta \cdot \widetilde{\phi} = 0. \tag{3.7}$$

This boundary condition allows to account for the type of boundary. According to fig. 3.1, no current flow can be observed at a boundary to a non-conductive medium (e.g., air), while a distinct current may flow through a conducting boundary depending on the strength of the injected current and its relative position to the boundary. The parameter β obviously controls the allowed current flow, and setting it to zero leads to a no-flow boundary condition (i.e., *Neumann* boundary condition). A current flow through a boundary can be expressed via $\beta \neq 0$ (*mixed* boundary condition).

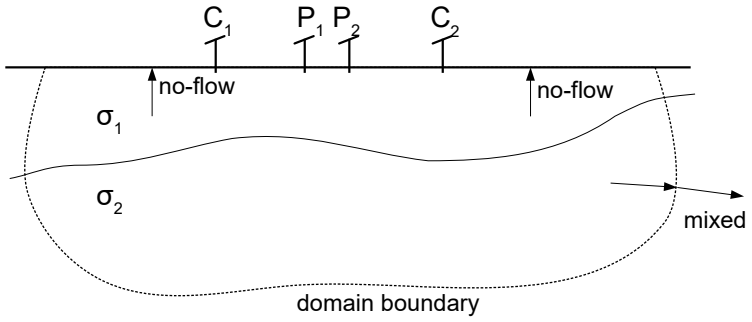

Figure 3.1: Sketch of a measurement setup with current and voltage electrodes. The dashed line denotes the model domain. At the top boundary, no current can flow into the air (*Neumann* boundary). At depth, current is flowing through the boundary into a conductive material (*mixed* boundary).

According to Schwarz (1991b) and based on the calculus of variations Courant & Hilbert (1924), the solution to the above boundary value problem is equivalent to minimizing the functional

$$F = \iint_G (\frac{1}{2}(\sigma_x(\partial_x\widetilde{\phi})^2 + \sigma_z(\partial_z\widetilde{\phi})^2) + \frac{1}{2}\sigma_y\widetilde{\phi}^2 - \frac{I}{2}\delta(x-x_s)\delta(z-z_s)\widetilde{\phi})dxdz + \oint_C \frac{1}{2}\beta\widetilde{\phi}^2 ds \tag{3.8}$$

with respect to $\widetilde{\phi}$ on the domain G with the boundary ∂G. In that case,

$$\partial F = 0. \tag{3.9}$$

In finite elements, the domain G is divided into n_e sub-domains $G^{(j)}$ with corresponding conductivities $\underline{\underline{\sigma}}_j$. Moreover, the domain boundary ∂G is divided into n_r sub-sections $(\partial G)^{(j)}$ with the corresponding parameter β_j:

$$G = \bigcup_{j=1}^{n_e} G^{(j)} \text{ and } \partial G = \bigcup_{j=1}^{n_r} (\partial G)^{(j)}. \tag{3.10}$$

The integral over the domain G can then be written as the sum of the integrals over the sub-domains $G^{(j)}$:

$$F = \sum_{j=1}^{n_e}(\frac{1}{2}\iint_{G^{(j)}} \sigma_{x,j}(\partial_x\widetilde{\phi}) + \sigma_{z,j}(\partial_z\widetilde{\phi})dxdz + \frac{1}{2}\sigma_{y,j}k^2\iint_{G^{(j)}}\widetilde{\phi}^2 dxdz - \frac{I}{2}\iint_{G^{(j)}}\delta(x-x_s)\delta(z-z_s)\widetilde{\phi}dxdz + \sum_{j=1}^{n_r}\frac{1}{2}\beta_j\int_{(\partial G)^{(j)}}\widetilde{\phi}^2 ds. \tag{3.11}$$

The sub-domains $G^{(j)}$ and the boundary sections $(\partial G)^{(j)}$ are implicitly characterized by their n_j nodes i. Every node i in G is assigned with a potential $\widetilde{\phi}_i$. The total potential function $\widetilde{\phi}$ can then be approximated. For that purpose, a linear function trend of $\widetilde{\phi}$ is assumed on each sub-domain. At the nodes, continuity allows to connect the linear function approaches between different sub-domains. Generally, the considered domain may be divided into triangles, quadrilaterals or higher order polygons. Yet, in this thesis only triangles and quadrilaterals are considered.

3.3.1 Element Types

In this section, the symbolic integrals are carried out for the "area elements" on the sub-domains $G^{(j)}$ and for the "boundary elements" on the boundary sections $(\partial G)^{(j)}$. Detailed derivations are depicted in appendix B.

The n_r integrals on the boundary ∂G,

$$\int_{\partial G^{(j)}} \widetilde{\phi}^2 ds \tag{3.12}$$

can be expressed with along the coordinate s along $\partial G^{(j)}$ with the linear ansatz

$$\widetilde{\phi}(s) \approx c_1^{(j)} + c_2^{(j)} s. \tag{3.13}$$

In matrix notation, this can be written as (see appendix B)

$$\int_{\partial G^{(j)}} \widetilde{\phi}^2 ds = \underline{\widetilde{\boldsymbol{\phi}}}^{(j)^T} \boldsymbol{S}_3'^{(j)} \underline{\widetilde{\boldsymbol{\phi}}}^{(j)} \tag{3.14}$$

with

$$\boldsymbol{S}_3'^{(j)} = \frac{L^{(j)}}{6} \begin{pmatrix} 2 & 1 \\ 1 & 2 \end{pmatrix} \text{ and } \underline{\widetilde{\boldsymbol{\phi}}^{(j)}} = (\widetilde{\phi}_{i_1(j)}, \widetilde{\phi}_{i_2(j)}). \tag{3.15}$$

$L^{(j)}$ is the length of the jth boundary element. The potentials $\widetilde{\phi}_{i_{1,2}(j)}$ are located on both ends of the boundary element. The n_e triangular sub-domain/area element integrals

$$\begin{aligned} \frac{1}{2} \iint_{G^{(j)}} (\sigma_{x,j} (\partial_x \widetilde{\phi}) + \sigma_{z,j} (\partial_z \widetilde{\phi}) + \frac{1}{2} \sigma_{y,j} k^2 \widetilde{\phi}^2 \\ - \frac{I}{2} \delta(x - x_s) \delta(z - z_s) \widetilde{\phi}) dx \, dz \end{aligned} \tag{3.16}$$

can be approximated with a linear ansatz function

$$\widetilde{\phi}(x, z) = c_1^{(j)} + c_2^{(j)} x + c_3^{(j)} z. \tag{3.17}$$

The result can be written in matrix notation as (see Appendix B)

$$\begin{aligned} &\frac{1}{2} \iint_{G^{(j)}} (\sigma_{x,j} (\partial_x \widetilde{\phi}) + \sigma_{z,j} (\partial_z \widetilde{\phi}) + \frac{1}{2} \sigma_{y,j} k^2 \widetilde{\phi}^2 \\ &\qquad - \frac{I}{2} \delta(x - x_s) \delta(z - z_s) \widetilde{\phi}) dx \, dz \\ &= \frac{1}{2} \underline{\widetilde{\boldsymbol{\phi}}}^{(j)^T} \boldsymbol{S}_1'^{(j)} \underline{\widetilde{\boldsymbol{\phi}}}^{(j)} + \frac{1}{2} \underline{\widetilde{\boldsymbol{\phi}}}^{(j)^T} \boldsymbol{S}_2'^{(j)} \underline{\widetilde{\boldsymbol{\phi}}}^{(j)} \end{aligned} \tag{3.18}$$

with the accumulated matrices

$$\begin{aligned} \boldsymbol{S}_1'^{(j)} =& (\sigma_x a^{(x)} + \sigma_z a^{(z)}) \boldsymbol{S}_1 + (\sigma_x b^{(x)} + \sigma_z b^{(z)}) \boldsymbol{S}_2 \\ &+ (\sigma_x c^{(x)} + \sigma_z c^{(z)}) \boldsymbol{S}_3 \\ \boldsymbol{S}_2'^{(j)} =& \sigma_y k^2 J \boldsymbol{S}_4. \end{aligned} \tag{3.19}$$

This result differs from the previously used element integrals with *isotropic* conductivities. In these terms, the conductivity could always be factored out so that the matrices $\boldsymbol{S}_{1,2,3}$ together with their scaling factors a, b, c could be regarded cumulative, i.e., the sum

$$\sigma \left(a \boldsymbol{S}_1 + b \boldsymbol{S}_2 + c \boldsymbol{S}_3 \right). \tag{3.20}$$

This property finally has to be reflected within the finite element modeling algorithm where the compilation of the final linear system of equations (i.e., the *stiffness matrix*) has to be done later in the program. Preliminary, three matrices of the size of the stiffness matrix have to be buffered. Finally, they can be summed up with the corresponding anisotropic conductivities as factors.

The functional in eq. 3.11 can now explicitly written with the element matrices $\boldsymbol{S}_i^{(j)}$:

$$\begin{aligned} F = &\sum_{j=1}^{n_e}(\frac{1}{2}\iint_{G^{(j)}}\sigma_{x,j}(\partial_x\widetilde{\phi}) + \sigma_{z,j}(\partial_z\widetilde{\phi})dxdz + \frac{1}{2}\sigma_{y,j}k^2\iint_{G^{(j)}}\widetilde{\phi}^2dxdz \\ &-\frac{I}{2}\iint_{G^{(j)}}\delta(x-x_s)\delta(z-z_s)\widetilde{\phi}dxdz + \sum_{j=1}^{n_r}\frac{1}{2}\beta_j\int_{\partial G^{(j)}}\widetilde{\phi}^2ds \\ &= \sum_{j=1}^{n_e}\frac{1}{2}\underline{\widetilde{\boldsymbol{\phi}}}^{(j)^T}\boldsymbol{S}_1'^{(j)}\underline{\widetilde{\boldsymbol{\phi}}}^{(j)} + \frac{1}{2}\underline{\widetilde{\boldsymbol{\phi}}}^{(j)^T}\boldsymbol{S}_2'^{(j)}\underline{\widetilde{\boldsymbol{\phi}}}^{(j)} \\ &+ \sum_{j=1}^{n_r}\underline{\widetilde{\boldsymbol{\phi}}}^{(j)^T}\boldsymbol{S}_3'^{(j)}\underline{\widetilde{\boldsymbol{\phi}}}^{(j)}. \end{aligned} \tag{3.21}$$

This sum can be written as a linear system of equations (see the transformation at the end of Appendix B.1)

$$\boldsymbol{S}\underline{\widetilde{\boldsymbol{\phi}}} = \underline{\boldsymbol{b}}. \tag{3.22}$$

In this system, $\boldsymbol{S}$ is referred to as the *stiffness matrix* due to the origins of the finite element method as a modeling tool for elasticity and structural analysis in mechanics. This system of equations can be solved by common solvers such as the Python `numpy.linalg.solve` algorithm. Additional information on the finite element method can be found in Schwarz (1991b); Kemna (2000).

3.3.2 Boundary Conditions

The mixed boundary conditions

$$\sigma\frac{\partial\phi}{\partial n} + \beta\phi = 0 \tag{3.23}$$

are used to simulate asymptotic function behavior of the 3-D potential, $\phi \propto \frac{1}{r}$ on non-infinitely distanced boundary sections. In order to do so, a homogeneous-space solution is assumed at the boundary. For compliance with the continuity equation $\mathrm{div}\vec{j} = 0$, the conductivity of the direct neighbor cell is used. Accordingly for 2.5-D, the required potential $\widetilde{\phi}$ in this case would be the analytical homogeneous-space solution of the Helmholtz equation with a yet to be set value for the conductivity tensor, $\underline{\underline{\sigma}}$. In an isotropic medium with conductivity σ_{iso} and the source at the point of origin, the solution is (Kemna, 2000)

$$\widetilde{\phi}(\vec{r}) = \frac{I}{2\pi\sigma_{iso}}K_0(k|\vec{r}|) \tag{3.24}$$

with the current strength I and the modified Bessel function of order 0, K_0. In the case of anisotropic subsurfaces in a 2.5-D space, the boundary condition can be expressed as (see Appendix C)

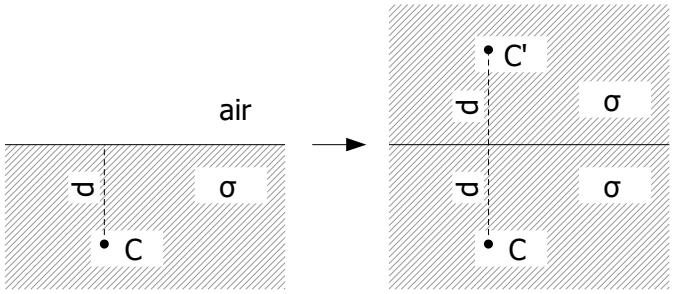

Figure 3.2: Sketch of an application of the image source method at a boundary with air over a homogeneous subsurface with conductivity σ (left). A current electrode C is buried in depth d. Obviously, no current can flow through this boundary. This constraint is achieved through regarding the full space with conductivity σ and inserting a second electrode C' at height d over the boundary. Modified after Jackson (2006).

$$\beta = \sqrt{\sigma_y} k g \tag{3.25}$$

$$g = \frac{K_1(\sqrt{\sigma_y} k r') \partial_n r'}{K_0(\sqrt{\sigma_y} k r')} \tag{3.26}$$

$$r' = \sqrt{\frac{x^2}{\sigma_x} + \frac{z^2}{\sigma_z}} \tag{3.27}$$

with the wave-number k, the modified Bessel functions of order 0 and 1, K_0 and K_1 and the coordinates x and z denoting the distance from the corresponding source.

In order to account for multiple sources, as utilized in typical measurement setups (dipole-dipole, Schlumberger, Wenner, gradient, etc.), summation may be applied in the form

$$\beta = \sqrt{\sigma_y} k g \tag{3.28}$$

$$g = \frac{K_1(\sqrt{\sigma_y} k r'_1) \partial_n r'_1 + K_1(\sqrt{\sigma_y} k r'_2) \partial_n r'_2 + ...}{K_0(\sqrt{\sigma_y} k r'_1) + K_0(\sqrt{\sigma_y} k r'_2)} \tag{3.29}$$

$$r'_i = \sqrt{\frac{x_i^2}{\sigma_x} + \frac{z_i^2}{\sigma_z}}. \tag{3.30}$$

Furthermore, this rule may be used to consider subsurface current sources with the method of image charges which tries to eliminate current flow of a subsurface (buried, borehole) electrode through a straight boundary. According to Jackson (2006), the problem of deriving the potential distribution of a buried current electrode can be treated with an equivalent system of two electrodes as depicted in Fig. 3.2. The electrical potential solution then simply is the superposition of the potentials of the buried and the image electrodes.

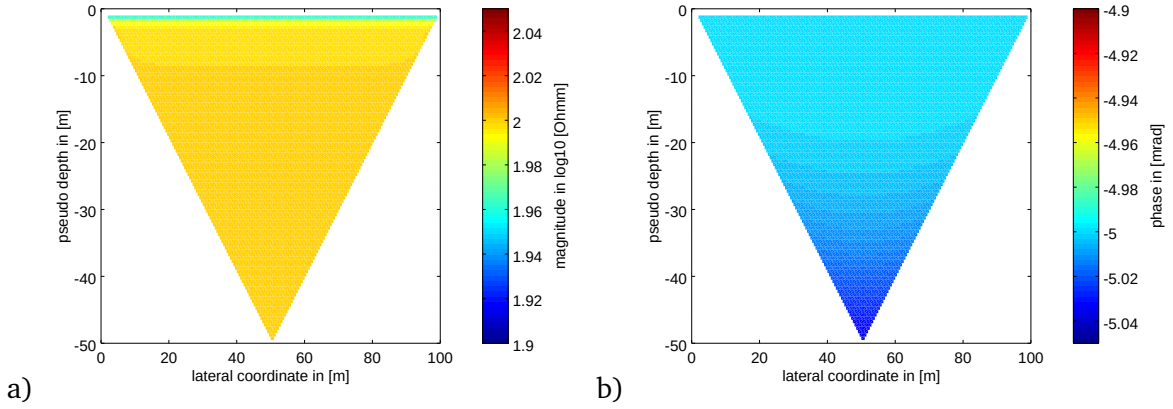

Figure 3.3: Synthetic modeled data of a forward-directed dipole-dipole set with 100 electrodes over a homogeneous half-space with $\sigma = \{0.01$ S/m, 5 mrad$\}$ plotted in pseudo-section form (see section 2.2). Figure a) depicts the magnitude in log_{10} [Ωm]; Figure b) displays the phase angle in [mrad].

3.4 Verification

The presented algorithm was implemented into the existing code `CRMod` (Kemna, 2000). The original implementation features the forward modeling in a 2.5-D space with arbitrary complex conductivity distributions. In the original form, it supports no-flow (i.e., *Neumann*) and mixed boundary conditions.

In the verification process, the anisotropic finite element solution is compared to analytical solutions for isotropic, anisotropic and layered half-spaces as well as to specific numerical data from isotropic subsurfaces. In the latter case, fine layers with isotropic conductivity are compared to an equivalent homogeneous model with anisotropic conductivity.

Simulations were carried out with a dipole-dipole configuration with an electrode distance of 1 m. The grid used for the following examples consists of 99 electrodes. At the surface, a Neumann boundary condition is used, while the bottom and the sides utilize a mixed boundary condition. The rectangular grid is chosen with 0.5 m line separation both horizontally and vertically.

3.4.1 Half-Space with Homogeneous Isotropic Conductivity

Obviously, the simplest model is a homogeneous half-space with isotropic conductivity. In this case, the conductivity is set to (see eq. 2.51) $\sigma = \{0.01$ S/m, 5 mrad$\}$. Figure 3.3 displays the synthetic modeled data recorded over this half-space with a dipole-dipole configuration. The ideal values of the shown apparent conductivity would be the homogeneous σ, so that $\sigma = \sigma_{\text{apparent}}$. Figure 3.4 exhibits the ratio of the modeled apparent conductivity (magnitude and phase) with respect to the ideal value. The deviation of the conductivity magnitude is largest close to the surface, where the impact of finite element sizes becomes visible. Here, the largest deviation is less than 9%. With larger pseudo depths, the deviation continues to be generally less than 1%.

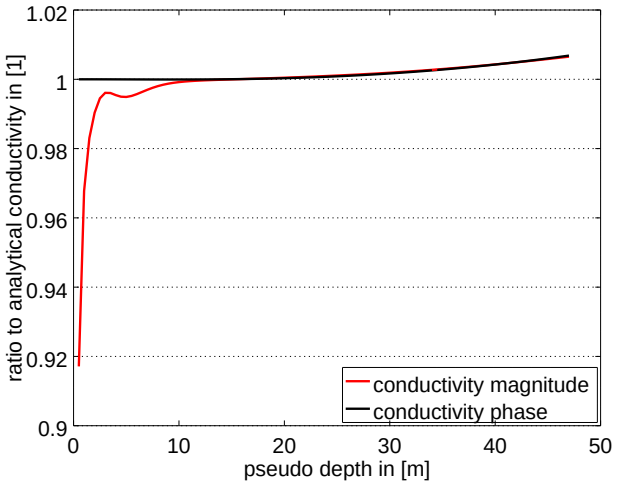

Figure 3.4: Ratio of modeled and analytical (ideal) apparent conductivity magnitude (red) and phase (black) over a homogeneous *isotropic* half-space.

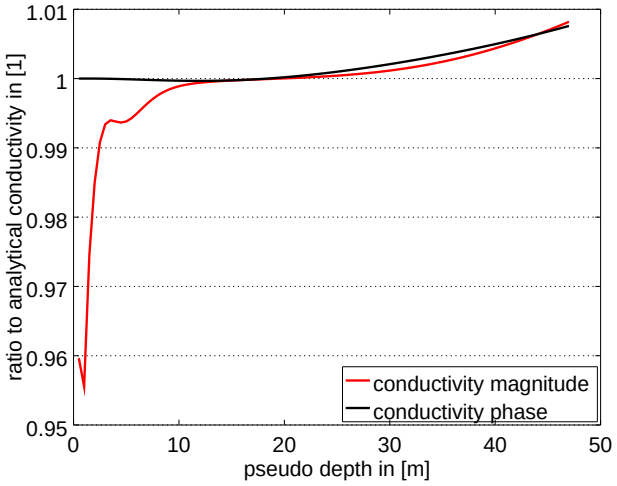

Figure 3.5: Ratio of modeled and analytical (ideal) apparent conductivity magnitude (red) and phase (black) over a homogeneous *anisotropic* half-space.

3.4.2 Half-Space with Homogeneous Anisotropic Conductivity

According to Parasnis (1986); Knödel (2005), a half-space with anisotropic conductivities in horizontal and vertical direction, σ_h and σ_v, can be represented analytically as an apparent isotropic half-space with the apparent conductivity

$$\sigma = \sqrt{\sigma_h \sigma_v} \tag{3.31}$$

An example model with $\sigma_h = 0.01 \frac{\mathrm{S}}{\mathrm{m}}$ and $\sigma_v = 0.04 \frac{\mathrm{S}}{\mathrm{m}}$ produces the apparent conductivity ratio in Figure 3.5. According to eq. 3.31, this leads to the apparent conductivity $\sigma_a = 0.02 \frac{\mathrm{S}}{\mathrm{m}}$. As before, this yields to generally low deviations for the phase angle (less than 1%) and decreasing apparent conductivity errors, starting with 5% but quickly decreasing to less than 1%.

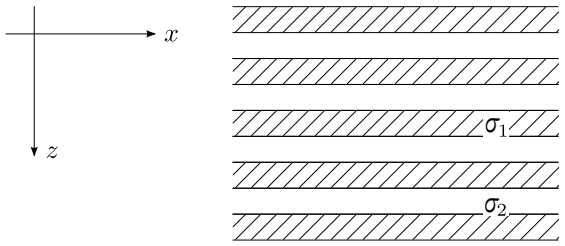

Figure 3.6: Detailed view into a horizontally layered half-space with complex conductivities σ_1 and σ_2.

3.5 Alternative Verification: Half-Space with Homogeneous Anisotropic Conductivity Simulated by Thin Layers *

Accuracy tests were performed through a comparison of half-spaces consisting of finely layered isotropic versus homogeneous anisotropic half-spaces. Starting with a horizontal finely layered isotropic half-space (see figure 3.6), the corresponding anisotropic model may be determined with the mixing laws (see section 2.7):

$$|\sigma_\parallel| = \frac{1}{2}\left(|\sigma_1|\exp\left(-i\varphi_1\right) + |\sigma_2|\exp\left(-i\varphi_2\right)\right) \tag{3.32}$$

$$\Rightarrow|\sigma_\parallel| \approx \frac{1}{2}(|\sigma_1| + |\sigma_2|)\exp\left(i\frac{-1}{|\sigma_1| + |\sigma_2|}\right)(|\sigma_1|\varphi_1 + |\sigma_2|\varphi_2) \tag{3.33}$$

and

$$\sigma_\perp = 2\left(\frac{1}{|\sigma_1|\exp(-i\varphi_1)} + \frac{1}{|\sigma_1|\exp(-i\varphi_1)}\right)^{-1} \tag{3.34}$$

$$\Rightarrow\sigma_\perp \approx 2\left(\frac{1}{|\sigma_1|} + \frac{1}{|\sigma_2|}\right)^{-1}\exp\left(-i\frac{1}{\frac{1}{|\sigma_1|} + \frac{1}{|\sigma_2|}}\left(\frac{\varphi_1}{|\sigma_1|} + \frac{\varphi_2}{|\sigma_2|}\right)\right) \tag{3.35}$$

Here, $\sigma_\parallel$ and $\sigma_\perp$ are the magnitudes of the effective complex conductivity parallel and perpendicular to the assumed layers. $\varphi_\parallel$ and $\varphi_\perp$ are the corresponding phase angles. For both the parallel and perpendicular directions, corresponding to parallel and serial connections, the magnitude mixing works like in the DC case where the effective magnitude only depends on the two magnitudes of layers 1 and 2. Contrary to this, the effective phase values depend on both the magnitude and phase of media 1 and 2 and are computed as a magnitude weighted phase average. Since the consideration is independent of the rotation of the anisotropic media with respect to the surface, the conclusion holds also for arbitrary directions, i.e., full-complex conductivity tensors, provided they are equivalent to layering. In this case, the grid consists of 94000 cells. The element width between the two electrodes is 0.5 m (two elements between two electrodes) and the element height inside the half-space is 0.25 m.

*The sections 3.5, 3.6 and 3.7 are adapted from Kenkel, J., Hördt, A., & Kemna, A. 2012. 2D modelling of induced polarization data with anisotropic complex conductivities. *Near Surface Geophysics*, **10**(6), 533–544.

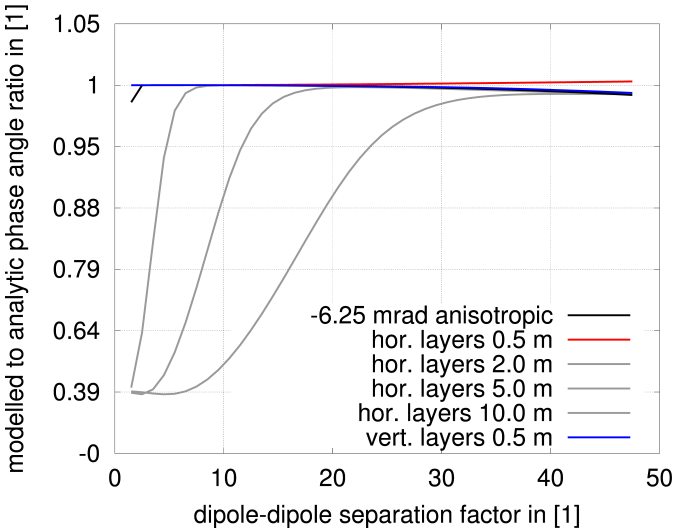

Figure 3.7: Anisotropic half-space (black line), horizontally layered half-space with 0.5 m layer thickness (red line) and vertically layered (blue line) data with also 0.5 m layer thickness. The modeled data are shown as a ratio with respect to the analytical solution -6.25 mrad. The gray lines show the effects of thicker layers (2.0 m, 5.0 m and 10.0 m).

3.5.1 Homogeneous Phase Angles

In case of equal phase angles for both layers, $\varphi = \varphi_1 = \varphi_2$, equations 3.33 and 3.35 can be simplified:

$$\sigma_{\parallel} = \frac{\|\sigma_1\| + \|\sigma_2\|}{2} \, \mathrm{e}^{i\varphi} \tag{3.36}$$

$$\sigma_{\perp} = \frac{2}{\frac{1}{\|\sigma_1\|} + \frac{1}{\|\sigma_2\|}} \, \mathrm{e}^{i\varphi} \tag{3.37}$$

The result implies that in case of equal phase angles in all layers, magnitude averaging is independent of the phase angle.

3.5.2 Homogeneous Magnitudes

The second case is represented by homogeneous magnitudes and different phase angles. In that case, equations 3.33 and 3.35 can be simplified to

$$\sigma_{\perp} = \|\sigma\| \, \mathrm{e}^{\frac{\varphi_1+\varphi_2}{2}} \tag{3.38}$$

$$\sigma_{\parallel} = \|\sigma\| \, \mathrm{e}^{\frac{\varphi_1+\varphi_2}{2}} \tag{3.39}$$

The result highlights that phase angles are calculated in the same way for both the parallel and perpendicular directions. This means that independent of the individual phase angles φ_2 and φ_2, the anisotropic phase is indistinguishable from isotropic phases with

$$\varphi_1 = \varphi_2 = \frac{\varphi_1 + \varphi_2}{2}. \tag{3.40}$$

Consequently, if one assumes anisotropy to be caused by sequences of thin layers, an anisotropic phase can only occur if the resistivity magnitude shows anisotropy. The mixing laws slightly change when the assumption of small phase values is given up:

$$\sigma_{\parallel} = \sigma \cos\left(\frac{\varphi_1 + \varphi_2}{2}\right) \exp^{i\frac{\varphi_1+\varphi_2}{2}} \tag{3.41}$$

$$\sigma_{\perp} = \frac{\sigma}{\cos\left(\frac{\varphi_1+\varphi_2}{2}\right)} \mathrm{e}^{i\frac{\varphi_1+\varphi_2}{2}} \tag{3.42}$$

Again the phase angles are averaged identically for the parallel and perpendicular directions and thus no anisotropy can be resolved. It is important to note that at large phase angles, the magnitude is no longer independent of the phase angle. However, in geophysical applications, phase shifts of -100 mrad are already considered large. If, for example, $\varphi_1 = -100$ mrad and $\varphi_2 = -20$ mrad, one obtains a magnitude decrease of 0.2% — this effect is very small.

According to equations 3.38 and 3.39 a layered half-space with horizontal layers as illustrated in Fig. 3.6 with homogeneous magnitudes $\|\sigma\|$ and varying phases of the complex resistivities

$$\sigma_1 = \|\sigma\| \, \mathrm{e}^{i(-2.5 \text{ mrad})} \tag{3.43}$$

$$\sigma_1 = \|\sigma\| \, \mathrm{e}^{i(-10 \text{ mrad}))} \tag{3.44}$$

$$\tag{3.45}$$

results in anisotropic phase values of

$$\sigma_{\parallel} = \|\sigma\| \, \mathrm{e}^{i(-6.25 \text{ mrad})} \tag{3.46}$$

$$\sigma_{\perp} = \|\sigma\| \, \mathrm{e}^{i(-6.25 \text{ mrad}))} \tag{3.47}$$

$$\tag{3.48}$$

Since the anisotropic phase angles are the same for both the parallel and perpendicular directions, this case is actually isotropic. The analytical apparent phase angle therefore is -6.25 mrad.

In fig. 3.7 the ratio of the modeled isotropic layer half-space data with respect to the analytical solution is shown with respect to the dipole-dipole separation factor with a red line. The deviation is less than 2%. The deviation at the top is due to the size of the single layers with respect to the electrode spacing and therefore the dipole-dipole separation, which is linked to the electrode configuration. This can be understood by means of two extreme situations:

- The layers are much thicker than the depth range covered by the largest electrode spacing, e.g., the layers are of the size $\gg 10$ m, while the maximum dipole-dipole separation is of some 10 m. In this case, the whole current system is only influenced by the first layers and the apparent complex impedance will only depend on these first layers, e.g., a two-layer case.

- The layers are much thinner than the electrode separation, e.g., the layers are the size 1 cm and while the dipole-dipole separation is again of some 10 m. Now, the current system is influenced by many layers in a way that the current system

becomes smooth and the apparent complex impedance would comply with the complex anisotropic impedances as introduced in equations (6) and (9). In fig. 3.7, three gray lines show the model results with larger layer thicknesses, varying from 2.0 m to 10.0 m. With thicker layers, the strong deviation reaches larger dipole-dipole separations. Isotropic vertical layers show a similar behavior. In this case, the isotropic layers with the same resistivities as in the horizontally layered case are modeled with vertical orientation. The layer thickness is again 0.5 m. The blue line in fig. 3.7 displays the ratio between the modeled data and the analytical value, which again shows a good agreement to the isotropic half-space. The black line shows the ratio of the modeled anisotropic homogeneous half-space with respect to the analytical solution.

The result shows a small deviation from the analytical solution. It is generally less than 1%. The results indicate the validity of the mixing laws. Ideally, the results of the horizontally and vertically layered structures and the anisotropic mixed case do not differ from the analytical solution. This agreement is achieved with reasonable accuracy, in particular at large dipole-dipole separations. It is clear nevertheless, that with relatively thick layers compared to the electrode distance the effect of single layers is visible at small separations.

3.6 Homogeneous Half-Space with Anisotropic Phase Angles

The above mixing laws may be applied to models with embedded sections of fine layers where no analytical solution exists. The comparison can only be done with respect to the anisotropic modeled phase angles. For this purpose, a model where both resistivity and phase shift are different for the two media is used. As explained above the anisotropic magnitudes are necessary to obtain anisotropic phases.

$$\sigma_1 = \frac{1}{50}\,\mathrm{S\,m^{-1}}\,\mathrm{e}^{-i(2\ \mathrm{mrad})} \tag{3.49}$$

$$\sigma_1 = \frac{1}{200}\,\mathrm{S\,m^{-1}}\,\mathrm{e}^{-i(30\ \mathrm{mrad})}\,. \tag{3.50}$$

In terms of complex anisotropic resistivities, this is

$$\begin{aligned} \|\sigma\|_z &= (\frac{1}{125}\,\mathrm{S\,m^{-1}}) & \|\sigma\|_{x,y} &= \frac{1}{80}\,\mathrm{S\,m^{-1}} \\ \varphi_z &= -24.4\ \mathrm{mrad} & \varphi_{x,y} &= -7.6\ \mathrm{mrad}. \end{aligned} \tag{3.51}$$

The results are displayed in Fig. 3.8 in terms of the phase angle ratio as in the previous section. They show a strong but quickly decreasing deviation with increasing depth. The strong deviation at small dipole-dipole separations results from the non-infinite thin layers, i.e., the larger the dipole-dipole separation the more the apparent magnitude and phase are spatially averaged. Therefore, at small dipole-dipole separations the impact of the first layer is large. In this case, the first layer is set to have a phase angle of $-2\ \mathrm{mrad}$. Together with our mixing laws, these results indicate a successful implementation of anisotropy into our code.

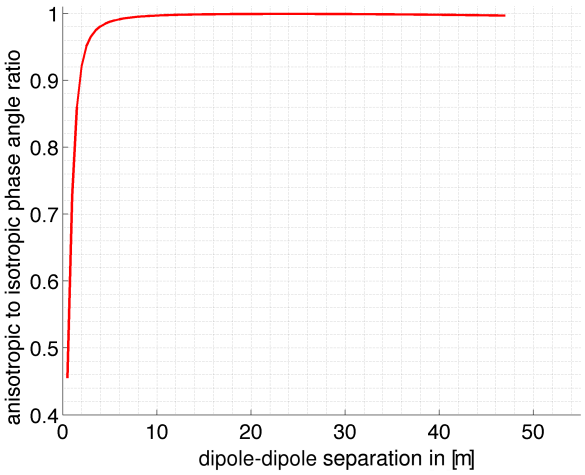

Figure 3.8: Ratio of the phase angles calculated for an anisotropic half-space with $\sigma_{x,y} = \frac{1}{80}\,\mathrm{S\,m^{-1}}$, $\varphi_{x,y} = -7.6\,\mathrm{mrad}$, $\sigma_z = \frac{1}{125}\,\mathrm{S\,m^{-1}}$ and $\varphi_z = -24.4\,\mathrm{mrad}$ with respect to the layered half-space with $\sigma_1 = \frac{1}{50}\,\mathrm{S\,m^{-1}}$, $\varphi_1 = -2\,\mathrm{mrad}$ and $\sigma_2 = \frac{1}{200}\,\mathrm{S\,m^{-1}}$, $\varphi_2 = -30\,\mathrm{mrad}$.

3.7 Models with Anisotropic Blocks

In addition to the previous verifications, two block models with only a small block of either isotropic layers or homogeneous anisotropic conductivity embedded in a homogeneous half-space are examined. Equations 3.38 and 3.39 are used to calculate equivalent complex resistivities for isotropic layered (see Fig. 3.9) and anisotropic (see Fig. 3.10) blocks. The layered block with isotropic phase angles $-2\,\mathrm{mrad}$ and $-30\,\mathrm{mrad}$ and magnitudes $\frac{1}{50}\,\mathrm{S\,m^{-1}}$ and $\frac{1}{200}\,\mathrm{S\,m^{-1}}$ (arbitrarily chosen values) corresponds to an anisotropic block with a phase angle of $-7.6\,\mathrm{mrad}$ and a magnitude of $\frac{1}{80}\,\mathrm{S\,m^{-1}}$ in both the x and y directions and a phase angle of $-24.4\,\mathrm{mrad}$ and a magnitude of $\frac{1}{120}\,\mathrm{S\,m^{-1}}$ in the z direction. Figure 3.11 shows the modeled phase angles with respect to the dipole-dipole separations. It indicates a good agreement of the layered model versus the anisotropic block model. At both the top and bottom of the block, the largest differences between the isotropic and anisotropic models are observed. This is again due to the finite layer thickness in the isotropic case.

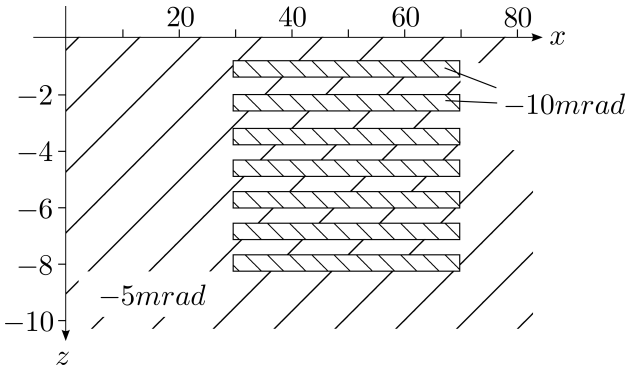

Figure 3.9: Block consisting of isotropic layers with phase angles $-10\,\mathrm{mrad}$ and $-5\,\mathrm{mrad}$ inside the sketched block and homogeneous $-5\,\mathrm{mrad}$ outside. The magnitude is constant and anisotropic (see text).

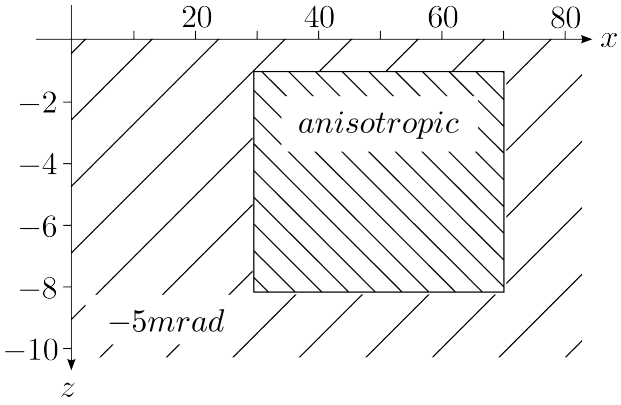

Figure 3.10: Anisotropic block with a homogeneous phase angle of -7.5 mrad in all three principal axes to represent the isotropic layered block in fig. 3.9. Again, the background is -10 mrad. The magnitude is constant and anisotropic (see text).

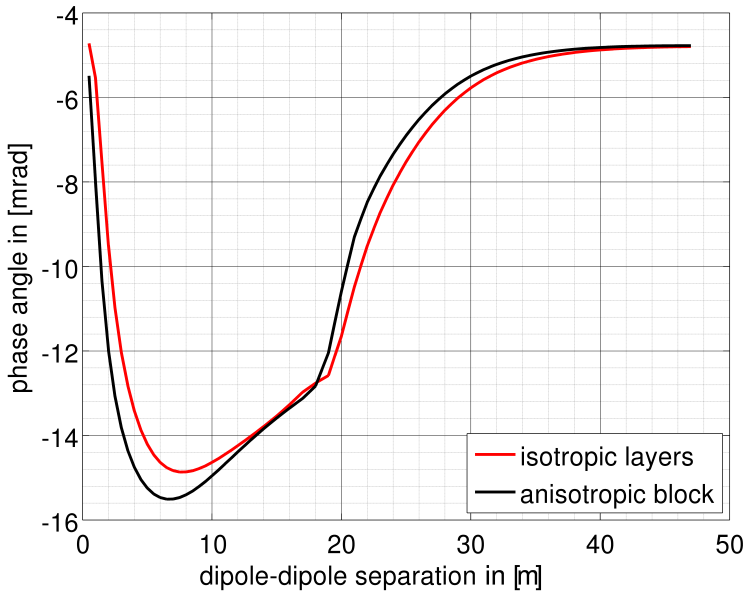

Figure 3.11: Apparent phase angle of modeled data with isotropic phase layers (red line) and an anisotropic block with corresponding anisotropic phase angles (black line) with respect to the dipole-dipole separation.

4

Sensitivity *

In the next sections, isotropic and anisotropic sensitivity distributions are presented and interpreted with a focus on implications on the inversion algorithm. It is highlighted that the understanding of sensitivity patterns of typical measurement configurations can be crucial to a successful application of a corresponding anisotropic inversion scheme.

The outline of the following sensitivity-related sections is as follows: first, the anisotropic complex-valued sensitivity is derived for the application to the code of Kemna (2000). Along with this, the extension of the principle of reciprocity to anisotropy is delineated. Then, the implementation is validated by means of the analytical sensitivities of Greenhalgh *et al.* (2009) for the case of a trivial homogeneous half-space. As an additional validation, a relationship between the isotropic sensitivity and the sum of the anisotropic sensitivities is evaluated. As a main part, the anisotropic sensitivities of common configurations over and in homogeneous half-spaces with and without embedded anomalies are presented and discussed. To extend the discussed patterns, the sensitivity with respect to the anisotropy ratio is computed and interpreted.

4.1 Anisotropic Sensitivity Computation

Sensitivity may be defined as the partial derivative of the measured impedance Z with respect to the complex conductivity tensor $\underline{\underline{\sigma}}$ at arbitrary points in the subsurface. Assuming anisotropy, for reasons of simplicity, only in the three principal axes that coincide with the (x, y, z) Cartesian coordinates, the complex conductivity tensor is

$$\underline{\underline{\sigma}} = \begin{pmatrix} \sigma_x & 0 & 0 \\ 0 & \sigma_y & 0 \\ 0 & 0 & \sigma_z \end{pmatrix} \tag{4.1}$$

and the corresponding anisotropic sensitivities are

$$\frac{\partial Z}{\partial \sigma_x(x,y,z)}, \frac{\partial Z}{\partial \sigma_y(x,y,z)}, \frac{\partial Z}{\partial \sigma_z(x,y,z)}. \tag{4.2}$$

*The sections 4.1, 4.2, 4.3 and 4.4 are adapted from Kenkel, J., & Kemna, A. 2017. Sensitivity of 2-d complex resistivity measurements to subsurface anisotropy. *Geophysical Journal International*, **208**(2), 1043–1057.

In the case of a parametrization into grid cells j with anisotropic conductivities $\sigma_k^{(j)}, k \in (x, y, z)$, the anisotropic sensitivities can be written as

$$\frac{\partial Z}{\partial \sigma_x^{(j)}}, \frac{\partial Z}{\partial \sigma_y^{(j)}}, \frac{\partial Z}{\partial \sigma_z^{(j)}}. \tag{4.3}$$

The following sensitivity derivation is fitted to the 2.5-D finite element modeling code of Kemna (2000), which was extended to anisotropic modeling in the previous sections. In this section, sensitivities are implemented with the assumption of 2-D parameter distribution with variations only allowed in the (x, z) plane while the y axis remains constant. As mentioned in the previous section, point electrical sources are modeled.

Note: Despite the 2-D assumption, the conductivity can still be anisotropic in all three dimensions (x, y, z).

In the considered case of a result from the FE modeling, the electric potential vector $\boldsymbol{\phi}$ containing the complex electrical potential values at all nodes of the 2-D mesh, is used for further analysis. As depicted in section 3.2, the electric potential vector, $\boldsymbol{\phi}$, is obtained by solving the Helmholtz equation, which results from Fourier transformation of the Poisson equation with given boundary conditions into the wave-number domain with respect to the strike direction y, for the transformed complex potential vector $\widetilde{\boldsymbol{\phi}}$. Accordingly, the inverse Fourier transform needs to be applied.

The main computational task of the forward modeling is the solution of the linear system of equations for $\widetilde{\boldsymbol{\phi}}$ in the wave-number domain. Similar to the modeling, the sensitivity computation is performed in the wave-number domain.

The linear system of equations being solved in the wave-number domain for a current point source at node l can be written as

$$\mathbf{S}\widetilde{\boldsymbol{\phi}}^{(l)} = \mathbf{b}^{(l)}, \tag{4.4}$$

with the complex FE matrix $\mathbf{S}$, the transformed complex potential $\widetilde{\boldsymbol{\phi}}^{(l)}$ and the current source vector $\mathbf{b}^{(l)}$, which contains the current strength $I^{(l)}$ in the l-th component and is zero elsewhere (see section 3.2. Differentiating eq. 4.4 with respect to the complex conductivity in the Cartesian direction $k \in \{x, y, z\}$ of the j-th element, $\sigma_k^{(j)}$, yields (see e.g., Rodi (1976); Oristaglio & Worthington (1980); Sasaki (1989) for the isotropic, real-valued DC case)

$$\mathbf{S}\frac{\partial \widetilde{\boldsymbol{\phi}}^{(l)}}{\partial \sigma_k^{(j)}} = -\frac{\partial \mathbf{S}}{\partial \sigma_k^{(j)}}\widetilde{\boldsymbol{\phi}}^{(l)} \tag{4.5}$$

The complex sensitivity $\frac{\partial \widetilde{\boldsymbol{\phi}}^{(l)}}{\partial \sigma_k^{(j)}}$ fulfills the Cauchy-Riemann conditions (Kemna, 2000), i.e.,

$$\left(\frac{\partial \widetilde{\boldsymbol{\phi}}^{(l)}}{\partial \sigma_k^{(j)}}\right)' = \frac{\partial \widetilde{\boldsymbol{\phi}}'^{(l)}}{\partial \sigma'^{(j)}_k} = \frac{\partial \widetilde{\boldsymbol{\phi}}''^{(l)}}{\partial \sigma''^{(j)}_k}, \left(\frac{\partial \widetilde{\boldsymbol{\phi}}^{(l)}}{\partial \sigma_k^{(j)}}\right)'' = \frac{\partial \widetilde{\boldsymbol{\phi}}''^{(l)}}{\partial \sigma'^{(j)}_k} = -\frac{\partial \widetilde{\boldsymbol{\phi}}'^{(l)}}{\partial \sigma''^{(j)}_k} \tag{4.6}$$

where $'$ and $''$ respectively denote real and imaginary parts.

The following notation follows the notation of Kemna (2000) for comparability. The structure of the FE matrix $\mathbf{S}$ (see Kenkel *et al.* (2012)) causes its derivative with respect to the directional conductivities $\sigma_k^{(j)}$ to vanish for all but the j-th element. Accordingly, the right-hand side of eq. 4.5 can be treated as a (fictitious) source vector, $\mathbf{c}^{(j)}$, which

has non-vanishing entries only at the M nodes κ_m, $m \in \{1, \ldots, M\}$) that correspond to the j-th element. Consequently, eq. 4.5 can be written as

$$\mathbf{S}\frac{\partial\widetilde{\boldsymbol{\phi}}^{(l)}}{\partial\sigma_k^{(j)}} = \mathbf{c}^{(j)}. \tag{4.7}$$

From the analogy of eqs. 4.4 and 4.7 it can be argued that the solution of eq. 4.7 is given by the superposition of the potential values due to the individual fictitious source terms at nodes κ_m, i.e., for the p-th component (node p) of the sensitivity vector it can be written

$$\frac{\partial\widetilde{\phi}_p^{(l)}}{\partial\sigma_k^{(j)}} = \sum_{m=1}^{M}\widetilde{\phi}_p^{(\kappa_m)}. \tag{4.8}$$

Based on the principle of reciprocity (see Appendix C.1), current source and potential measurement points can be interchanged without changing the impedance, i.e.,

$$\frac{\widetilde{\phi}_p^{(\kappa_m)}}{c_{\kappa_m}^{(j)}} = \frac{\widetilde{\phi}_{\kappa_m}^{(p)}}{b_p} \tag{4.9}$$

for each node κ_m where the fictitious source vector $\mathbf{c}^{(j)}$ has non-zero entries (i.e., the nodes of the j-th element). In eq. 4.9, $\widetilde{\phi}_{\kappa_m}^{(p)}$ is the potential at node κ_m due to a point source with current strength $b_p = I^{(p)}$ at node p. Inserting eq. 4.9 into eq. 4.8, and replacing $\mathbf{c}^{(j)}$ according to eqs. 4.5 and 4.7 again, leads to

$$\begin{aligned}\frac{\partial\widetilde{\phi}_p^{(l)}}{\partial\sigma_k^{(j)}} &= -\frac{1}{I^{(p)}}\sum_{m=1}^{M}\widetilde{\phi}_{\kappa_m}^{(p)}\left[\frac{\partial\mathbf{S}}{\partial\sigma_k^{(j)}}\widetilde{\boldsymbol{\phi}}^{(l)}\right]_{\kappa_m} \\ &= -\frac{1}{I^{(p)}}\sum_{m=1}^{M}\sum_{n=1}^{M}\left[\frac{\partial\mathbf{S}}{\partial\sigma_k^{(j)}}\right]_{\kappa_m\kappa_n}\widetilde{\phi}_{\kappa_m}^{(p)}\widetilde{\phi}_{\kappa_n}^{(l)}.\end{aligned} \tag{4.10}$$

Although the FE matrix $\mathbf{S}$ in the anisotropic case has a different form than in the isotropic case, all its entries remain linear in the conductivity (see section 3.3 and Kenkel *et al.* (2012), and therefore, analogous to the isotropic case (see Kemna (2000)), the term $\left[\frac{\partial\mathbf{S}}{\partial\sigma_k^{(j)}}\right]_{\kappa_m\kappa_n}$ does not depend on conductivity; in fact it is real-valued and only depends on the geometry of the j-th element and the chosen FE approach within the element.

When the transformed sensitivities are computed according to eq. 4.10 for all point sources (i.e., electrode positions) used in a configuration (e.g., a tomographic survey), the sensitivity of a specific impedance, $\frac{\partial Z}{\partial\sigma_k^{(j)}}$, is obtained by means of inverse Fourier transform and corresponding superposition fully analogous to the isotropic case (see Kemna (2000)).

4.2 Validation

4.2.1 Analytical Anisotropic Sensitivities

A validation of the above algorithm can be performed through comparison with an analytical solution over a homogeneous subsurface. Greenhalgh *et al.* (2009) presented

a perturbation approach to derive expressions for anisotropic sensitivities with respect to real-valued conductivities. However, the derived expressions likewise hold for the complex (IP) case. Accordingly, the sensitivities with respect to the complex conductivities in the different Cartesian directions of a small volumetric element can be calculated from the corresponding directional derivatives of the potential fields due to the current source at node l and a fictitious (ad-joint) source at the measurement point at node p (with current strength $I^{(p)}$), $\phi_j^{(l)}$ and $\phi_j^{(p)}$, respectively:

$$\frac{\partial \phi_p^{(l)}}{\partial \sigma_k^{(j)}} = \frac{-w_j}{I^{(p)}} \left(\frac{\partial \phi_j^{(l)}}{\partial k} \frac{\partial \phi_j^{(p)}}{\partial k} \right), k \in \{x, y, z\} \tag{4.11}$$

where w_j is the volume of the j-th element, and $\phi_j^{(l)}$ and $\phi_j^{(p)}$ are evaluated at the center of the j-th element, $\mathbf{r}_j$. In the case of a homogeneous, isotropic half-space with complex conductivity σ, the potentials $\phi_j^{(l)}$ and $\phi_j^{(p)}$ are given by

$$\phi_j^{(l)} = \frac{I^{(l)}}{2\pi\sigma} \frac{1}{|\mathbf{r}_j - \mathbf{r}_l|}, \phi_j^{(p)} = \frac{I^{(p)}}{2\pi\sigma} \frac{1}{|\mathbf{r}_j - \mathbf{r}_p|} \tag{4.12}$$

with $\mathbf{r}_l$ and $\mathbf{r}_p$ being the positions of nodes l and p, respectively, and eq. 4.11 results in

$$\frac{\partial \phi_p^{(l)}}{\partial \sigma_k^{(j)}} = -w_j \frac{I^{(l)}}{(2\pi\sigma)^2} \left(\frac{(\mathbf{r}_j - \mathbf{r}_l)_k}{|\mathbf{r}_j - \mathbf{r}_l|^3} \frac{(\mathbf{r}_j - \mathbf{r}_p)_k}{|\mathbf{r}_j - \mathbf{r}_p|^3} \right), \tag{4.13}$$

where $(\ldots)_k$ means the k-th component of the vector in parentheses.

To compare the sensitivity with respect to a volumetric element ("3-D" sensitivity) from eq. 4.13 with the sensitivity with respect to an areal element with infinite extension in the strike direction y ("2.5-D" sensitivity), eq. 4.13 is evaluated for volumetric elements at the same (x, z) but different y positions, and the results are subsequently integrated along the y axis.

The validation is carried out for pole-pole, pole-dipole, dipole-dipole and Wenner configurations at the surface.

The relative deviation between the results of the two computational approaches is below 2% in the considered discretized cross-section, except in the direct vicinity of the electrodes where larger deviations occurred due to the singularity for the electric potential, which is only poorly approximated by the FE solution.

The results in Fig. 4.1 indicate a good agreement between analytical and numerical approach; the regarded examples are pole-pole, pole-dipole, dipole-dipole, Wenner and Schlumberger configurations at the surface of a homogeneous half-space. In most areas except in the vicinity of the electrodes, the relative deviation is capped at 1%, although values may rise to $> 2\%$ close to the electrodes.

4.2.2 Sum of Anisotropic Sensitivities

Another validation is carried out based on the relationship between the sum of the different anisotropic sensitivities and their isotropic counterparts (see eq. 3.20 in section 3.3.1) in the case of isotropy. The anisotropic conductivities in the different spatial directions, σ_k, $k \in \{x, y, z\}$, can be considered as three independent parameters, and therefore

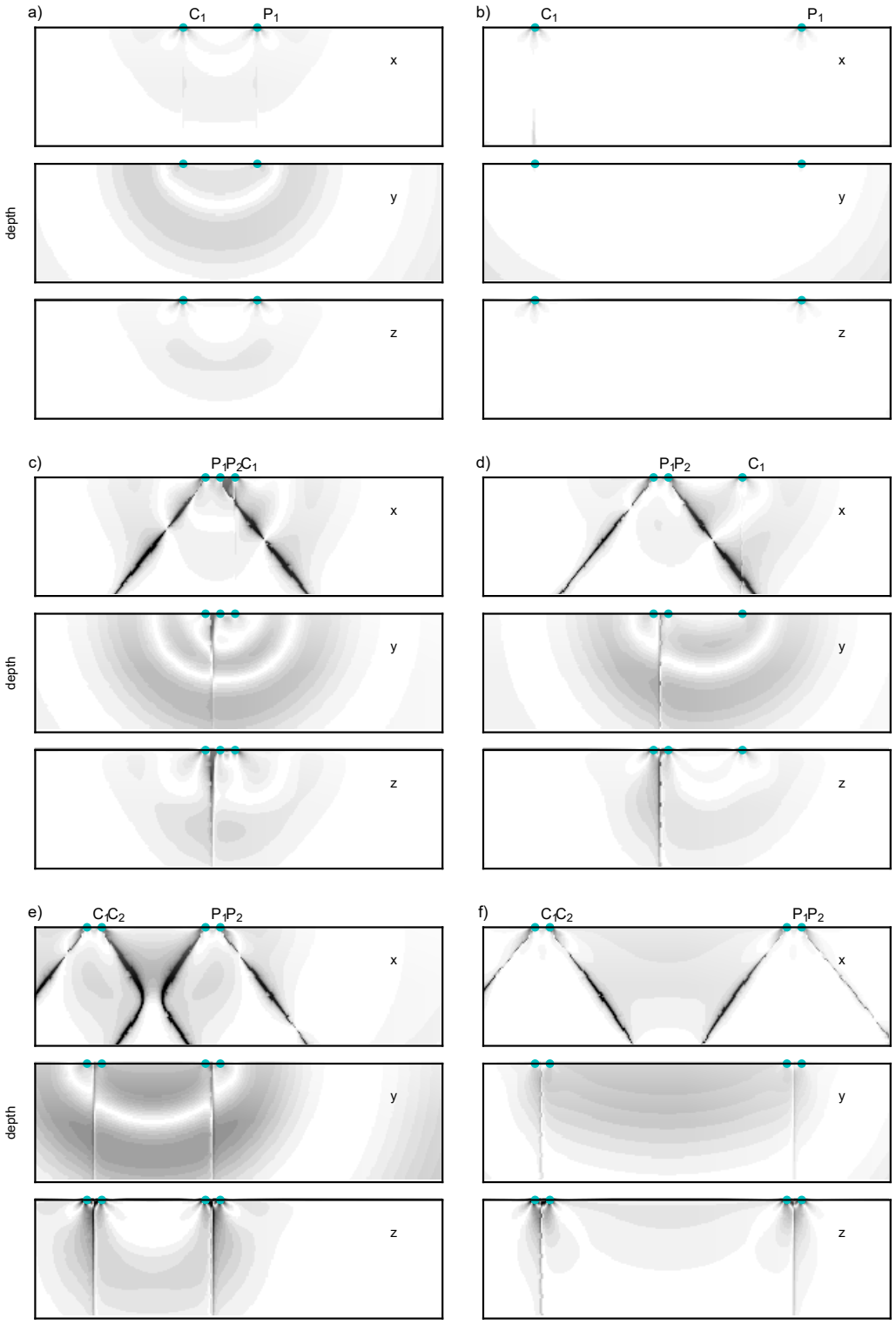

to be continued on the next page...

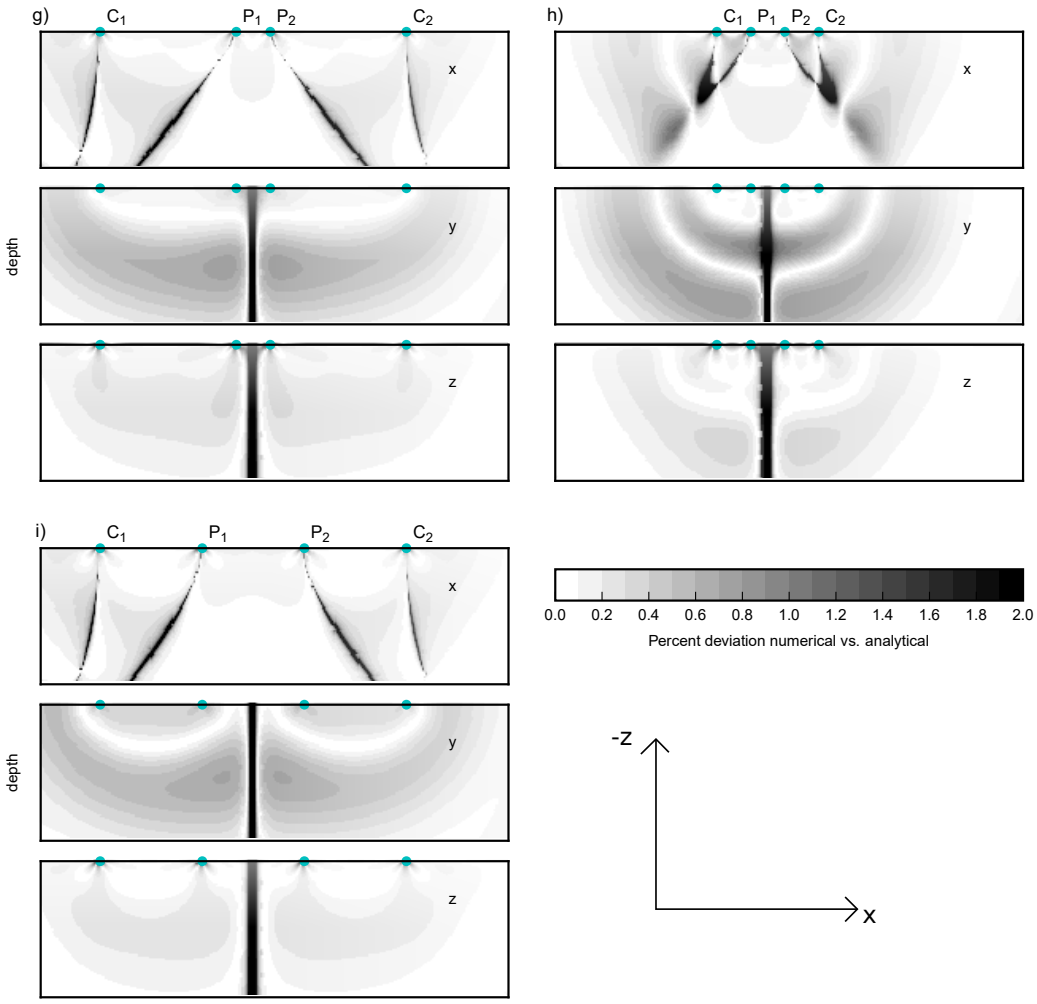

Figure 4.1: x-z sections: relative deviation in percent between numerical and analytical anisotropic normalized real-valued sensitivities with respect to (x,y,z)-direction over a homogeneous half space for various configurations (similar to Friedel (2000)): a) and b) pole pole, c) and d) pole dipole, e) to i) dipole dipole. Turquoise dots represent the electrode positions of current (C) and potential (P) electrodes.

the total derivative of the potential ϕ with respect to the isotropic conductivity, σ, may be written as

$$\frac{d\phi}{d\sigma} = \sum_k \frac{\partial \phi}{\partial \sigma_k} \frac{\partial \sigma_k}{\partial \sigma}, k = \{x, y, z\}. \tag{4.14}$$

In the case of isotropy, all conductivities σ_k are equal, leading to $\frac{\partial \sigma_k}{\partial \sigma} = 1$, and finally

$$\frac{d\phi}{d\sigma} = \sum_k \frac{\partial \phi}{\partial \sigma_k}, k = \{x, y, z\}. \tag{4.15}$$

The comparison was performed over a homogeneous, isotropic half-space, where the sensitivities were computed both with the isotropic implementation (Kemna, 2000) and the newly implemented anisotropic sensitivity computation scheme. The results exhibit a very good agreement with deviations only within the numerical precision.

4.3 Sensitivity Patterns

The figures 4.2 and 4.3 display exemplary patterns of the complex conductivity for each conductivity direction and as real and imaginary parts, i.e., $\frac{\partial Z^{'}}{\partial \sigma^{'}}$ and $\frac{\partial Z^{''}}{\partial \sigma^{''}}$. The presented configurations are (di)pole-(di)pole and Wenner for surface measurements and two different cross-hole dipole-dipoles in two boreholes. The depicted data are normalized per setup to the sum of the three anisotropic sensitivities, i.e., in this case the isotropic sensitivity. The individual anisotropic sensitivity patterns show characteristics similar to the isotropic case like a decrease of sensitivity with increasing distance to the electrodes. However, the anisotropic sensitivity patterns are often unequal for the different conductivity directions. This becomes apparent especially for the borehole configurations with very different textures for all conductivity directions. Less prominent, the surface measurements emphasize the texture differences between the x sensitivity and the two y and z sensitivities, while the latter two patterns are very similar. For these surface setups, the x sensitivity generally shows the largest absolute values, suggesting that the x conductivity can be recovered best. The real and imaginary components of the anisotropic sensitivities exhibit identical patterns, but differ in terms of sign and amplitude.

The analytical expressions for the anisotropic sensitivities from eq. 4.11 (Greenhalgh *et al.*, 2009) allow to easily comprehend the obtained sensitivity patterns. The right-hand side of eq. 4.11 contains the product of the directional derivatives of the potential fields due to the current source at the true injection poles and a fictitious current source at the potential measurement poles. The directional derivatives of the potential are directly related to the current density components through Ohm's law, and thus the anisotropic sensitivity $\frac{\partial Z}{\partial \sigma_k}$ is determined by the product of the corresponding components k of the current densities resulting from the true and fictitious source configurations. For instance for the pole-pole configuration in fig. 4.2, the multiplied directional derivatives $\frac{\partial \phi_j^{(l)}}{\partial k} \frac{\partial \phi_j^{(p)}}{\partial k}$ are negative only in x direction and between the two electrodes; everywhere else the term is positive. The patterns of the pole-dipole, dipole-dipole and Wenner configurations in Fig. 4.2 can be understood from the general pole-pole sensitivity pattern by means of corresponding superposition.

Inserting an anomalous anisotropic block into the previously considered homogeneous half-space results in the sensitivity patterns shown in fig. 4.4 for the dipole-dipole

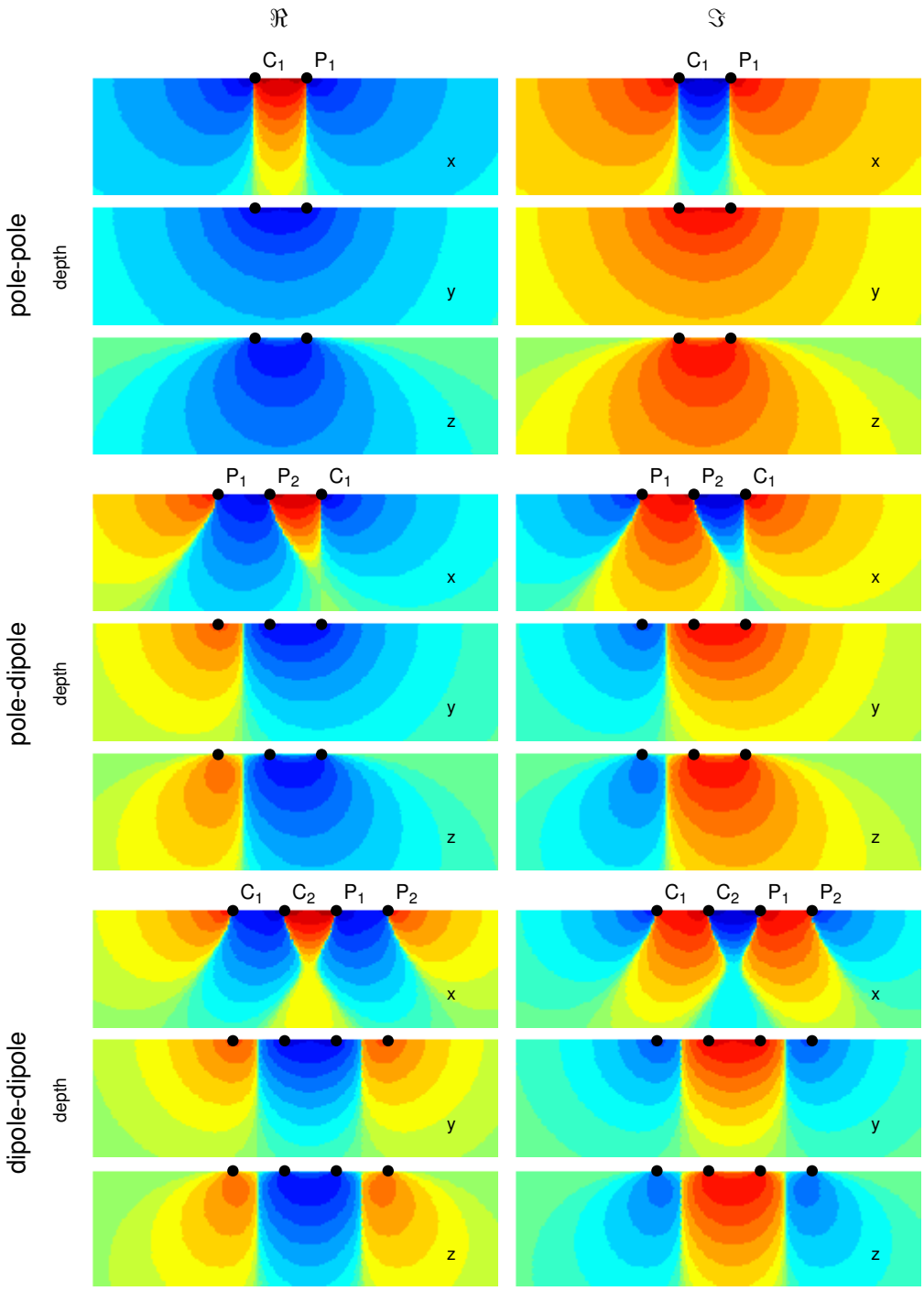

Figure 4.2: *to be continued on the next page...*

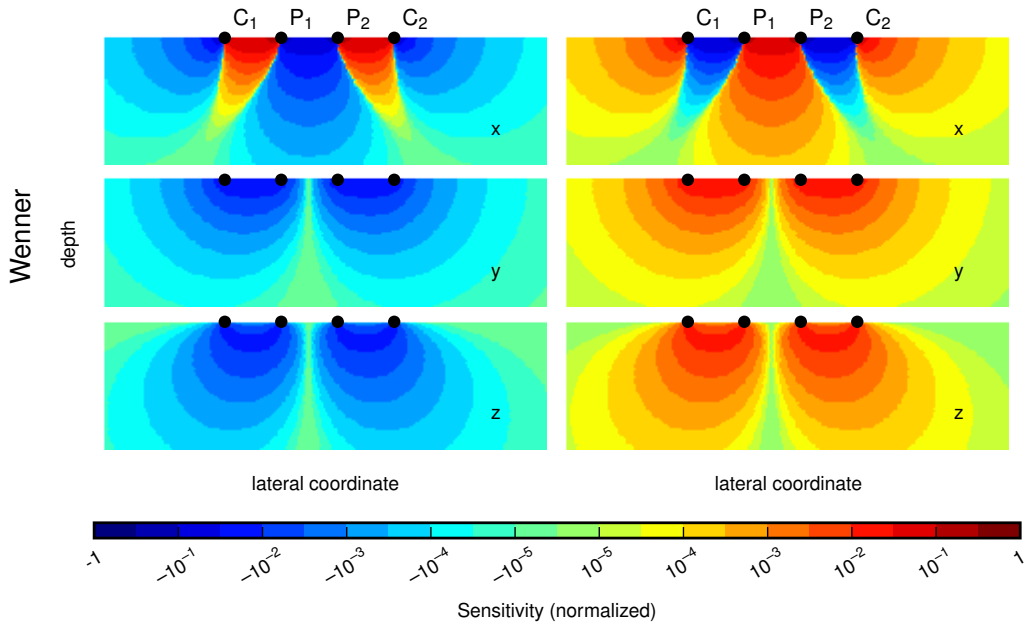

Figure 4.2: Cross-sectional distributions of real ($\Re$, left column) and imaginary ($\Im$, right column) components of the anisotropic sensitivities $\frac{\partial Z}{\partial \sigma_x}, \frac{\partial Z}{\partial \sigma_y}$ $\frac{\partial Z}{\partial \sigma_z}$ (respectively indicated by x, y, z) for pole-pole, pole-dipole, dipole-dipole and Wenner measurement configurations (from top to bottom) over a homogeneous, isotropic half-space. In each plot the respective sensitivities are normalised to the maximum absolute value of the sum of all three (x, y, z) sensitivities (i.e., the "isotropic" sensitivity according to eq. 4.15), separately for real and imaginary parts. Black dots indicate position of current (C) and potential (P) electrodes.

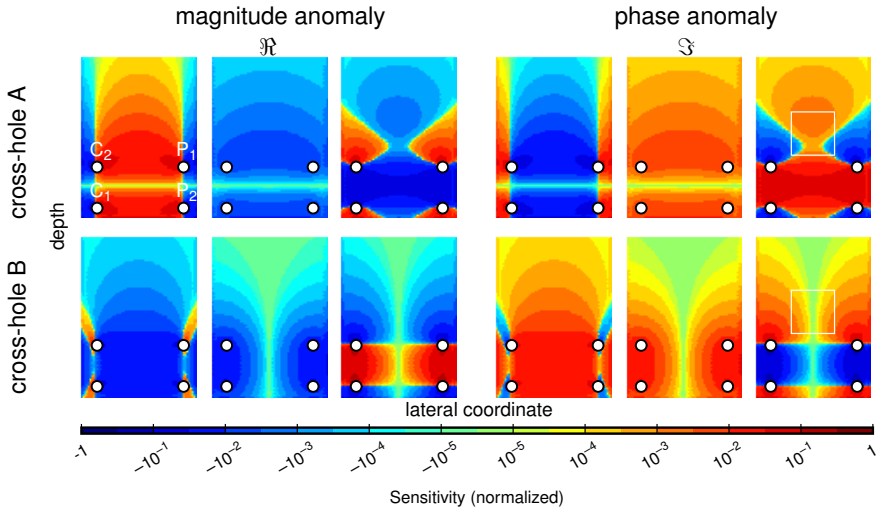

Figure 4.3: Cross-section view (see fig. 4.2) for two borehole setups. The top row displays the anisotropic sensitivities of a cross-hole setup with the two current and the two potential electrodes each in one borehole (termed ”cross-hole A”), and the bottom row with one current and one potential electrode in each borehole (termed ”cross-hole B”), respectively. In contrast to fig. 4.2, x, y and z conductivity are plotted side by side.

configuration. Here, either the magnitude or the phase angle of the anomalous block is changed, and this either for x, z or for all directions. The results reveal that the sensitivity patterns and thus the focus of the measurement are distorted depending on location and extension of the anomaly. However, the case of an anisotropic anomaly in terms of y direction does not exhibit a significant change of the sensitivity pattern compared to the homogeneous half-space case in fig. 4.2.

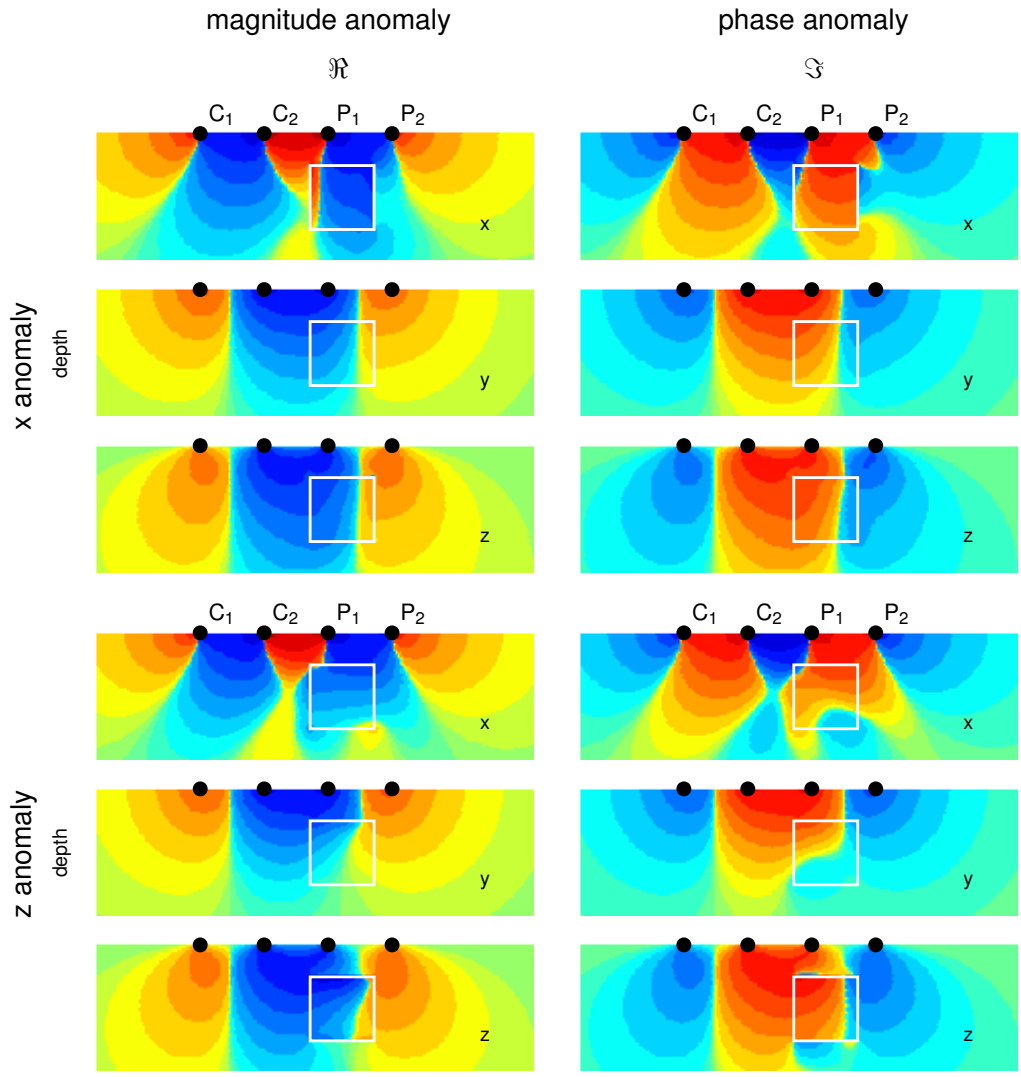

Figure 4.4: *to be continued on the next page...*

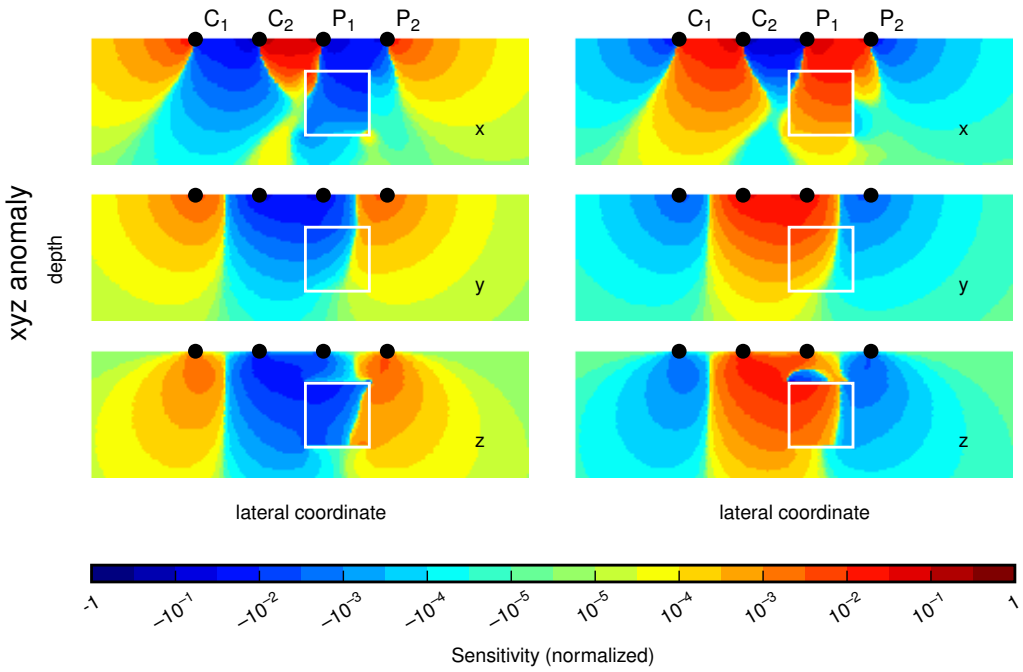

Figure 4.4: Cross-sectional, normalized distributions of the real and imaginary components of the anisotropic sensitivities (see fig. 4.2) for a dipole-dipole configuration over a homogeneous, isotropic half-space (with $100\,\Omega\mathrm{m}$ resistivity magnitude and $-10\,\mathrm{mrad}$ resistivity phase) with an embedded anomaly (white rectangle). The top, middle and bottom three panels display, respectively, (left) the real components ($\Re$) of $\frac{\partial Z}{\partial \sigma_x}$, $\frac{\partial Z}{\partial \sigma_y}$, $\frac{\partial Z}{\partial \sigma_z}$ for an anomaly with $1000\,\Omega\mathrm{m}$ resistivity magnitude in x, z and all (x, y, z) directions, and (right) the imaginary components ($\Im$) of $\frac{\partial Z}{\partial \sigma_x}$, $\frac{\partial Z}{\partial \sigma_y}$, $\frac{\partial Z}{\partial \sigma_z}$ for an anomaly with $-50\,\mathrm{mrad}$ resistivity phase in x, z and all (x, y, z) directions. Black dots indicate position of current (C) and potential (P) electrodes.

4.4 Sensitivity with respect to Anisotropy Ratio

The anisotropic complex sensitivities considered in the previous section describe the change of an impedance measurement due to a local change of the subsurface complex conductivity in a specific spatial direction. Although their patterns are mostly non-identical, it cannot be concluded that anisotropic parameters can necessarily be resolved. In order to assess this problem, the sensitivity with respect to anisotropy was computed. More specifically, anisotropy may be, for instance, described as a ratio of the complex conductivities in horizontal (x and y) and vertical (z) direction.

Let the anisotropy factor, $\lambda_{kl}, (k,l) \in \{x,y,z\}$, be defined as the (complex-valued) ratio of the complex conductivities in two different spatial directions, i.e., $\lambda_{kl} = \frac{\sigma_k}{\sigma_l}$. Then, the modified sensitivity is defined as $\frac{\partial Z}{\partial \lambda_{kl}}$. When applied to the two horizontal directions, x and y, the (complex-valued) sensitivity with respect to the anisotropy ratio can be obtained by means of application of the chain rule (see Appendix C.2)

$$\frac{\partial Z}{\partial \lambda_{xy}} = \sigma_y \frac{\partial Z}{\partial \sigma_x} - \frac{\sigma_x}{\lambda_{xy}^2} \frac{\partial Z}{\partial \sigma_y}. \tag{4.16}$$

Here, $\frac{\partial Z}{\partial \lambda_{xy}}$ depends solely on the x and y sensitivities. The sensitivities $\frac{\partial Z}{\partial \lambda_{xz}}$ and $\frac{\partial Z}{\partial \lambda_{yz}}$ can be computed analogously.

Figure 4.5 displays the resulting patterns of the sensitivities with respect to the three different anisotropy ratios with real and imaginary parts for a dipole-dipole configuration over a homogeneous, isotropic half-space. The results reveal distinct patterns for all of the anisotropy ratios, which indicates that, in principle, corresponding anisotropy should be resolvable from surface measurements. However, the magnitude of sensitivity varies largely: the real part of the sensitivity with respect to the horizontal anisotropy ratio λ_{xy} shows much larger absolute values than the real part in the other two cases. On the other hand, the largest absolute values of the imaginary part of the sensitivities are more similar for the different anisotropy ratios, differing by less than a factor of 20.

In order to assess the above mentioned sensitivities with respect to horizontal-vertical anisotropy, again the chain rule may be applied. With the horizontal and vertical conductivity, $\sigma_h = \sigma_x = \sigma_y$ and $\sigma_v = \sigma_z$, it can be stated that

$$\frac{\partial Z}{\partial \lambda_{hv}} = \sigma_v \frac{\partial Z}{\partial \sigma_h} - \frac{\sigma_h}{\lambda_{hv}^2} \frac{\partial Z}{\partial \sigma_v} \tag{4.17}$$

with $\frac{\partial Z}{\partial \sigma_h} = \frac{\partial Z}{\partial \sigma_x} + \frac{\partial Z}{\partial \sigma_y}$ and $\frac{\partial Z}{\partial \sigma_v} = \frac{\partial Z}{\partial \sigma_z}$.

A plot of this sensitivity for a dipole-dipole configuration over a homogeneous, isotropic half-space is shown in fig. 4.6. The distinctive sensitivity pattern, which also results for other measurement configurations, shows that it should be possible, in principle, to detect this type of anisotropy even with standard surface measurements.

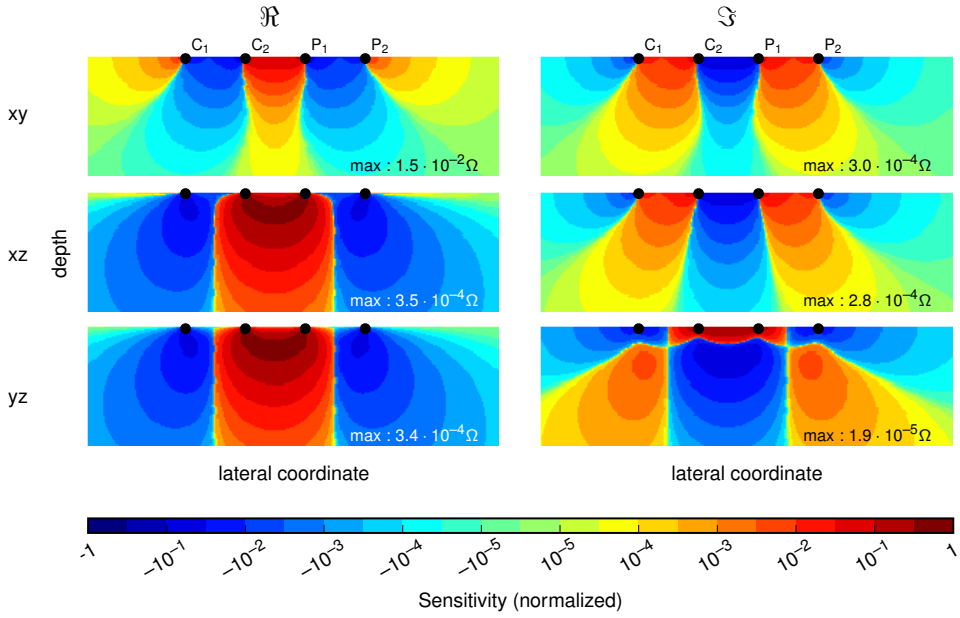

Figure 4.5: Cross-sectional distributions of real ($\Re$, left column) and imaginary ($\Im$, right column) components of the anisotropic sensitivities $\frac{\partial Z}{\partial \lambda_{xy}}$, $\frac{\partial Z}{\partial \lambda_{xz}}$, $\frac{\partial Z}{\partial \lambda_{yz}}$ (indicated by xy,xz,yz, respectively) with respect to the different anisotropy ratios $\lambda_{kl} = \sigma_k/\sigma_l$ for a dipole-dipole configuration over a homogeneous, isotropic half-space. In each plot the respective sensitivities are normalized to the (individual) maximum absolute value, which is stated in the bottom right corner. Black dots indicate position of current (C) and potential (P) electrodes.

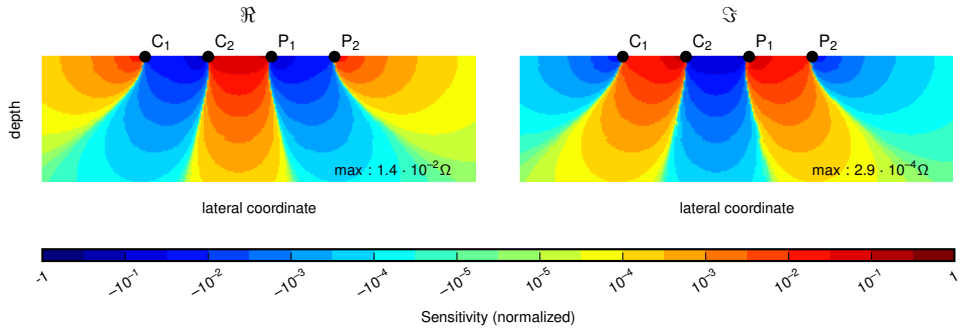

Figure 4.6: Cross-sectional distributions of real ($\Re$, left column) and imaginary ($\Im$, right column) components of the anisotropic sensitivity $\frac{\partial Z}{\partial \lambda_{hv}}$ with respect to the anisotropy ratio $\lambda_{hv} = \sigma_h/\sigma_v$ for a dipole-dipole configuration over a homogeneous, isotropic half-space. In each plot the respective sensitivities are normalized to the (individual) maximum absolute value, which is stated in the bottom right corner. Black dots indicate position of current (C) and potential (P) electrodes.

5

Inversion Algorithm

5.1 Work flow of Iterative Inversion

The inversion algorithm processes measured data into subsurface anisotropic complex conductivity sections. Figure 5.1 depicts the inversion algorithm scheme utilized in this work. The inversion starts by reading N measured data $\vec{d}$ with $d_i = \ln Z_i, i \in (1, N)$ that contain voltages V_i, phase shifts φ_i, injected currents I_i as well as the electrode locations/setups. A necessary starting model m with M model parameters $m_j = \ln\sigma_j, j \in (1, M)$ may be based on the data, e.g., through averaging all measured apparent conductivities, or contain chosen values, e.g. to incorporate predetermined model information. The forward model $f(m)$ contains the synthetic voltages corresponding to the given electrode positions, the injected current and a given model m, i.e. the starting model in the zeroth iteration. In the next step, the misfit between measured and synthetic data is computed, for instance with a L^2-norm. Accordingly, the misfit is compared to a predefined target misfit. If the agreement is greater than a given value, the algorithm advances to the computation of synthetic data sensitivities with respect to the model m, $\partial f(m)/\partial m$, at a model state m. Next, the model update function computes the iterative improvement dm based on the current model, the misfit and its predefined a priori constraints, such as "smooth model" (*Occam's razor*, see Constable (1987)), a model with isotropy, a model with faults, or a model with the least possible number of steep gradients (*Minimum Gradient Support*, see Portniaguine & Zhdanov (1999)). Then, the updated model is handed to the forward operator, yielding a new iteration cycle. Finally, if the misfit reaches its target value, the algorithm successfully finishes.

In this iterative approach, model updates have to be computed for each iteration step. The presented approach is based on Kemna (2000) and is usually referred to as *Tikhonov approach* (see Tikhonov & Arsenin (1977)). Here, the inherently ill-posed geoelectrics problem even in cases where the number of measured data is larger than the number of free subsurface parameters (i.e., grid cells) is solved with a damping parameter, representing chosen assumptions such as a general model smoothness or a more specific layering of the subsurface to possibly yield a unique model.

Generally, the Tikhonov approach tries to minimize a cost function. In this case (and closely following the notation of Kemna (2000)), this may be expressed through

$$\partial_m \Psi(m) = 0 \tag{5.1}$$

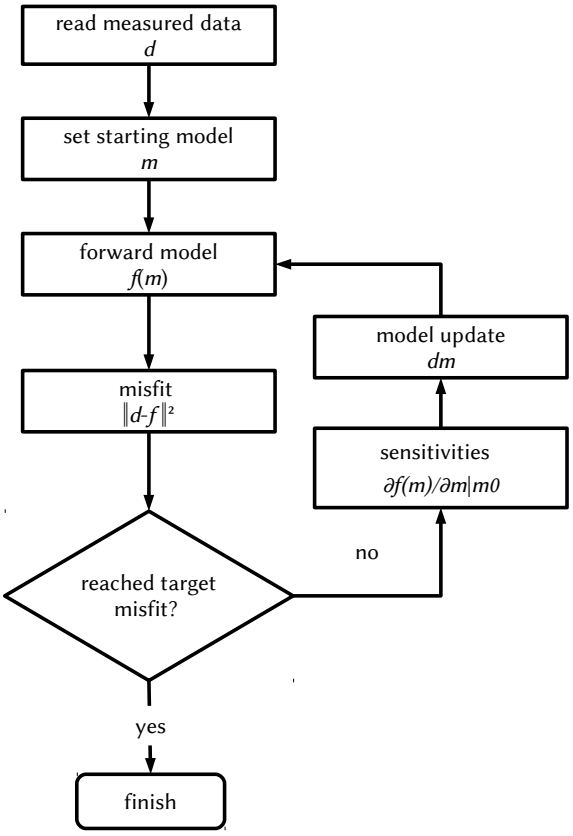

Figure 5.1: Flow diagram scheme of the inversion. Boxes represent computations, the square on one edge indicates a decision and the rounded boxes refer to states of the algorithm.

where

$$\Psi(m) = \Psi_d(m) + \lambda\Psi_m(m). \tag{5.2}$$

Here,

$$\Psi_d(m) = \sum_{i=1}^{N} \frac{|d_i - f_i(m)|^2}{|\epsilon_i|^2} \tag{5.3}$$

is the chi-squared functional that is used as a measure for the misfit between predicted and measured data, $f_i(m)$ and d_i, in relation with the assumed data error, ϵ_i. The last parameter in eq. 5.2, Ψ_m, contains the model cost function.

5.2 Model Cost Function

Typical model cost functions are:

- Smoothness-constraint model: This model is represented generally with

$$\Psi_m = \int \|\nabla m\|^2 dxdz. \tag{5.4}$$

  This constraint originates in the principle of *Occam's Razor*, stating that "among competing hypotheses, the one with the fewest assumptions should be selected" (Constable, 1987). Applied to IP tomography, the smoothness-constraint model

may be useful where no additional information about the subsurface is available. Moreover, it offers consistent conditions, e.g., for data comparison, and is suited for a general inversion approach.

In the case of a subsurface grid, its general definition can be narrowed to the difference in model cell values normalized by their distances, i.e.,

$$\Psi_m = \sum_{i=1}^{N} \left(\sum_{j=1}^{Nb_i} \left(\frac{m_i - m_j}{d_{ij}} \right)^2 \right), \tag{5.5}$$

with i iterating over all grid cells N and j iterating over all its neighboring cells Nb_i, considering their center distances d_{ij}. According to Kemna (2000), this may be rewritten as

$$\Psi_m = \|W_m m\|^2, \tag{5.6}$$

with the model vector m, constituted of the conductivity values in all cells.

- Smoothness-constraint model with respect to pre-defined background model. This model is based upon the above smoothness-constraint model, but further introducing a background m_0 in the form of

$$\Psi_m = \int (\nabla(m - m_0))^2. \tag{5.7}$$

This constraint is useful in cases, where a priori information is available, e.g. the location of a fault structure or a conductivity contrast. Within this inversion approach, this constraint can be expressed with

$$\Psi_m = \sum_{i=1}^{N} \left(\sum_{j=1}^{Nb_i} (\frac{m_i - m_{i0} - m_j + m_{j0}}{d_{ij}})^2 \right). \tag{5.8}$$

- Minimum gradient support (MGS). This constraint may be expressed as

$$\Psi_m = \int \frac{\|\nabla(m)\|^2}{\|\nabla(m)\|^2 + \beta^2}. \tag{5.9}$$

In the limiting case of $\beta \to 0$, small model gradients ∇m result in strong contributions to the model penalty function Ψ_m. Concluding, this approach allows only for the most necessary model boundaries and results in a model with few sections of constant conductivity. In the case of a large β, the MGS equals the smoothness-constraint model.

5.3 Excursus: Isotropic Update Function

This section cites the section "Inverse Problem/Numerical Solution" from Kemna (2000) and serves the purpose of adjusting the used symbols and terms to the present thesis. One may assemble the complex data errors $\epsilon_i, i \in (1, \dots, N)$ with the number of data points, N, in a diagonal data error matrix,

$$W_d = \text{diag}\left(1/\epsilon_1, 1/\epsilon_2, \dots\right). \tag{5.10}$$

According to Kemna (2000), assuming that data errors are uncorrelated, the data misfit function may be written as the L^2 norm

$$\Psi_d = \|W_d\,(d - f(m))\,\|^2 = \||W_d|\Re(d - f(m))\|^2 + \||W_d|\Im(d - f(m))\|^2. \tag{5.11}$$

This is the data objective function. With the model parameter objective function, Ψ_m (eq. 5.6), a global objective function may be written as

$$\Psi(m) = \Psi_d + \lambda_m \Psi_m \tag{5.12}$$

$$= \|W_d\,(d - f(m))\,\|^2 + \lambda_m \|W_m m\|^2. \tag{5.13}$$

Because of the L^2 norm for complex numbers, this may be written as

$$\Psi(m) = (d - f(m))^H W_d^H W_d (d - f(m)) + \lambda_m m^H W_m^T W_m m \tag{5.14}$$

with the complex conjugate transpose H and the regularization parameter λ_m. The Gauss-Newton algorithm is a way to find the minimum of eq. 5.14. It utilizes the first derivative with respect to the model vector m and sets it to zero. Kemna (2000) implements this as "normal equations" (Kemna & Binley, 1996) to determine the model parameter iterate Δm, specifically,

$$B\Delta m = b \tag{5.15}$$

with

$$B = A^H W_d^H W_d A + \lambda_m W_m^T W_m \tag{5.16}$$

and

$$b = A^H W_d^H W_d\,(d - f(m)) - \lambda_m W_m^T W_m m. \tag{5.17}$$

Here, A is the sensitivity matrix with $A_{ij} = \frac{\partial Z_i}{\partial \sigma_j}$. The solution to eq. 5.15, Δm, is the model vector iterate, containing the iterative best guess. In the presented inversion scheme, these iterations are repeated until a specific criterion (target data misfit, number of iterations, ...) is achieved. See Kemna (2000) for details on the implementation.

5.4 Anisotropic Update Algorithm

The principle of the isotropic update function of the previous section may be applied to anisotropy. In order to do so, the corresponding expressions for the model cost function need to be altered depending on the desired target of the inversion. The following three update algorithms are discussed in this work:

Individual x,y and z conductivity update The inversion algorithm allows for individual x,y and z conductivities. In order to constrain the anisotropy, a penalty function is applied.

Horizontal-vertical conductivity update Only horizontal ($\sigma_h = \sigma_x = \sigma_y$) and vertical ($\sigma_z$) conductivities are allowed. The anisotropy is again constrained with a penalty function.

Horizontal conductivity and anisotropy ratio update The inversion parameters are the horizontal conductivity ($\sigma_h = \sigma_x = \sigma_y$) and the horizontal-vertical anisotropy ratio ($\lambda_{hv} = \sigma_h/\sigma_z$).

5.4.1 Individual x,y and z conductivity update

In this case, anisotropy is expressed through the complex conductivities in the three principal axes, $\sigma_i, i \in (x, y, z)$. Hence, the corresponding sensitivities may be used to iteratively compute a subsurface model. In fact, the isotropic update function eq. 5.15 can independently be applied to each of the three conductivity directions. In matrix form, this may be expressed by concatenating the model parameter vectors $\vec{m}_i, i \in \{x, y, z\}$:

$$\vec{m}_a = (m_{x,1}, \dots m_{x,N}, m_{y,1}, \dots m_{y,N}, m_{z,1}, \dots m_{z,N})^H \tag{5.18}$$

Here, the model parameters are $m_{x,i} = \log \sigma_{x,i}, \dots$. Consequently, the normal equations (eq. 5.15) may be extended to

$$B_a \Delta \vec{m}_a = b_a \tag{5.19}$$

with

$$B = A_a^H W_d^H W_d A_a + \lambda_m W_{m,a}^T W_{m,a} \tag{5.20}$$

and

$$b = A_a^H W_d^H W_d \left(d - f(m)\right) - \lambda_m W_{m,a}^T W_{m,a} m_a \tag{5.21}$$

with the anisotropic sensitivities

$$A_a = \left(A_a^x, A_a^y, A_a^z\right) \tag{5.22}$$

$$= \left(\begin{array}{ccc|c|ccc} \frac{\partial Z_1}{\partial \sigma_x^{(1)}} & \cdots & \frac{\partial Z_1}{\partial \sigma_x^{(N)}} & \dots & \frac{\partial Z_1}{\partial \sigma_z^{(1)}} & \cdots & \frac{\partial Z_1}{\partial \sigma_z^{(N)}} \\ \vdots & & & & \vdots & & \\ \frac{\partial Z_M}{\partial \sigma_x^{(1)}} & \cdots & \frac{\partial Z_M}{\partial \sigma_x^{(N)}} & \dots & \frac{\partial Z_M}{\partial \sigma_z^{(1)}} & \cdots & \frac{\partial Z_M}{\partial \sigma_z^{(N)}} \end{array}\right) \tag{5.23}$$

with the extended model weighting matrix

$$W_{m,a} = \begin{pmatrix} [W_m] & 0 & 0 \\ 0 & [W_m] & 0 \\ 0 & 0 & [W_m] \end{pmatrix}. \tag{5.24}$$

However, to approach ambiguity in the data (apart from the smoothness constraint in section 5.3), anisotropy can be penalized. Here, the isotropy-favoring anisotropy penalty function according to Pain *et al.* (2003) is used. With their scheme, isotropy can be favored by minimizing

$$\Psi_a = \int (m_x(r), m_y(r), m_z(r)) \begin{pmatrix} 2 & -1 & -1 \\ -1 & 2 & -1 \\ -1 & -1 & 2 \end{pmatrix} (m_x(r), m_y(r), m_z(r))^T. \tag{5.25}$$

The above equation has its smallest value 0 if the model parameters are equal in all three directions, i.e., $m_x = m_y = m_z$. In the regarded case, no consideration is given to differently sized model cells*. When applied to a discrete number of model cells, this may be written as

$$\Psi_a = \vec{m}_a W_a \vec{m}_a^H \tag{5.26}$$

*In the case of differently sized model cells, their size should be used as a weighting parameter here.

with

$$W_a(i,j) = \begin{cases} 2, \text{if } i = j \\ -1, \text{if } j = (kN+i) \bmod (3N), k \in \{2,3\} \end{cases} \tag{5.27}$$

Explicitly, eq. 5.26 may be displayed as

$$\Psi_a = \vec{m}_a \left(\begin{array}{cccc|cccc|cccc} 2 & 0 & \dots & & -1 & 0 & \dots & & -1 & 0 & \dots & \\ 0 & 2 & 0 & \dots & 0 & -1 & 0 & \dots & 0 & -1 & 0 & \dots \\ & & \ddots & & & & \ddots & & & & \ddots & \\ & \dots & 0 & 2 & & \dots & 0 & -1 & & \dots & 0 & -1 \\ \hline -1 & 0 & \dots & & 2 & 0 & \dots & & -1 & 0 & \dots & \\ 0 & -1 & 0 & \dots & 0 & 2 & 0 & \dots & 0 & -1 & 0 & \dots \\ & & \ddots & & & & \ddots & & & & \ddots & \\ & \dots & 0 & -1 & & \dots & 0 & 2 & & \dots & 0 & -1 \\ \hline -1 & 0 & \dots & & -1 & 0 & \dots & & 2 & 0 & \dots & \\ 0 & -1 & 0 & \dots & 0 & -1 & 0 & \dots & 0 & 2 & 0 & \dots \\ & & \ddots & & & & \ddots & & & & \ddots & \\ & \dots & 0 & -1 & & \dots & 0 & -1 & & \dots & 0 & 2 \end{array}\right) \vec{m}_a^H. \tag{5.28}$$

In this case, three individual conductivities are used per model cell. The anisotropy penalty may be applied to the objective function,

$$\Psi(m) = \Psi_d + \lambda_m \Psi_m + \lambda_a \Psi_a, \tag{5.29}$$

where λ_a denotes a weighting factor for anisotropy. Similar to Kemna (2000), one may apply the Gauss-Newton algorithm to iteratively find the minimum of $\Psi(m)$ in eq. 5.29. The first three terms of the corresponding Taylor series are

$$\Psi \mid_m (\Delta m) = \Psi(m) + \frac{\partial \Psi(m)}{\partial m} \Delta m + {}^1\!/_2 \Delta m^H \frac{\partial}{\partial m^H} \frac{\partial \Psi(m)}{\partial m} \Delta m. \tag{5.30}$$

The minimum may be found by demanding

$$\begin{aligned} \frac{\partial \Psi \mid_m (m)}{\partial \Delta m} &= 0 \\ &= \frac{\partial \Psi(m)}{\partial m} + \left(\frac{\partial}{\partial m} \frac{\partial \Psi(m)}{\partial m^H} \right) \Delta m \\ \Leftrightarrow \left(\frac{\partial}{\partial m} \frac{\partial \Psi(m)}{\partial m^H} \right) \Delta m &= - \frac{\partial \Psi(m)}{\partial m}. \end{aligned} \tag{5.31}$$

Inserting eq. 5.29 yields

$$\frac{\partial \Psi(m)}{\partial m} = -2A^H W_d^H W_d \left(d - f(m)\right) + 2\lambda_m W_{m,a}^T W_{m,a} m + 2\lambda_a W_a m \tag{5.32}$$

$$\frac{\partial}{\partial m} \frac{\partial \Psi(m)}{\partial m^H} = 2A^H W_d^H W_d A + 2\lambda_m W_{m,a}^T W_{m,a} + 2\lambda_a W_a. \tag{5.33}$$

Finally, the model update vector Δm may be computed from

$$\begin{aligned} &\left(A^H W_d^H W_d A + \lambda_m W_{m,a}^T W_{m,a} + \lambda_a W_a \right) \Delta m \\ &= -A^H W_d^H W_d \left(d - f(m)\right) + \lambda_m W_{m,a}^T W_{m,a} m + 2\lambda_a W_a m. \end{aligned} \tag{5.34}$$

Consequently, the model update vector is applied in each model iteration (see the previous section, 5.3).

The above update algorithm allows for three model values per cell, i.e., three complex conductivities per cell. The inversion results therefore consist of these three individual complex conductivities. However, the update algorithm may be applied to two complex conductivities per cell, e.g.,

- horizontal and vertical complex conductivities
- horizontal conductivity σ_h and anisotropy ratio σ_h/σ_v.

5.4.2 Horizontal-Vertical Conductivity Update

The inversion of independent horizontal and vertical complex conductivity, σ_h and σ_v, can be achieved through re-structuring of the update algorithm. Obviously, the model vector $\vec{m}_a$ (eq. 5.18) only consists of

$$\vec{m}_a = (m_{h,1}, \dots m_{h,N}, m_{v,1}, \dots m_{v,N})^T \tag{5.35}$$

with $m_{h,i} = \log \sigma_{h,i}$ and $m_{v,i} = \log \sigma_{v,i}$. Consequently, the normal equations eq. 5.21 can be adjusted accordingly. Since $\sigma_h = \sigma_x = \sigma_y$, the sensitivity with respect to the horizontal conductivity, $\frac{\partial Z_i}{\partial \sigma_h}$ may be expressed as

$$\begin{aligned} \frac{\partial Z_i}{\partial \sigma_h} &= \frac{\partial Z_i}{\partial \sigma_x}\frac{\partial \sigma_x}{\partial \sigma_h} + \dots \\ &= \frac{\partial Z_i}{\partial \sigma_x} + \frac{\partial Z_i}{\partial \sigma_y}. \end{aligned} \tag{5.36}$$

In the regarded case, the vertical sensitivity is the z sensitivity. The model weighting matrix may be written as

$$W_{m,a} = \begin{pmatrix} [W_m] & 0 \\ 0 & [W_m] \end{pmatrix}. \tag{5.37}$$

The anisotropy penalty (eq. 5.25) may be adjusted accordingly, i.e.,

$$\Psi_a = \int (m_h(r), m_v(r)) \begin{pmatrix} 2 & -1 \\ -1 & 2 \end{pmatrix} (m_h(r), m_v(r))^H. \tag{5.38}$$

5.4.3 Horizontal Conductivity and Anisotropy Ratio Update

The inversion can also be carried out for the target parameter's horizontal conductivity σ_h and horizontal-vertical anisotropy ratio λ_{hv}. Similar to the previous section, the model vector $\vec{m}_a$ (eq. 5.18) now contains

$$\vec{m}_a = (m_{h,1}, \dots m_{h,N}, m_{\lambda_{hv},1}, \dots m_{\lambda_{hv},N})^T \tag{5.39}$$

with $m_{h,i} = \log \sigma_{h,i}$ and $m_{\lambda_{hv},i} = \log \frac{\sigma_{h,i}}{\sigma_{v,i}}$. According to the above paragraph 5.4.2, the sensitivity with respect to the horizontal conductivity is

$$\frac{\partial Z_i}{\partial \sigma_h} = \frac{\partial Z_i}{\partial \sigma_x} + \frac{\partial Z_i}{\partial \sigma_y}. \tag{5.40}$$

The sensitivity with respect to the horizontal-vertical anisotropy ratio can be expressed through

$$\frac{\partial Z_i}{\partial \lambda_{hv}} = \frac{\partial Z_i}{\partial \sigma_x}\frac{\sigma_x}{\lambda_{hv}} + \dots \tag{5.41}$$

$$= \sigma_z \left(\frac{\partial Z_i}{\partial \sigma_x} + \frac{\partial Z_i}{\partial \sigma_y} \right) - \frac{\sigma_z^2}{\sigma_x}\frac{\partial Z_i}{\partial \sigma_z}. \tag{5.42}$$

Similar to the previous section, the model weighting matrix is

$$W_{m,a} = \begin{pmatrix} [W_m] & 0 \\ 0 & [W_m] \end{pmatrix}. \tag{5.43}$$

The anisotropy penalty of Pain *et al.* (2003) is not applicable in this case. However, anisotropy is already constrained through the model weighting matrix that is applied on the anisotropy ratio. Consequently, this model does not bound anisotropy, but requires its ratio to be homogeneous on the inverted section.

A possible application of this inversion algorithm may be in the case of a strong background anisotropy, e.g., through sedimentary layering in which another structure with different conductivity and/or anisotropy ratio is embedded.

6

Synthetic Study

6.1 Measurement Response to Anisotropic Anomalous Body for Different Measurement Configurations *

6.1.1 Surface Measurements

This section displays measurement response curves obtained in simulated surface profiling surveys. The profiling takes place with different measurement setups over a homogeneous isotropic subsurface with an embedded anisotropic anomaly (see Fig. 6.1. Here, anisotropy is incorporated using either a x, y or z conductivity or an isotropic conductivity for the anomaly.

The synthetic response curves are shown in Fig. 6.2. The four arrays show different overall amplitudes of the responses, with the pole-dipole and Wenner arrays producing the strongest response, in terms of both magnitude and phase, and the dipole-dipole array showing the weakest responses in terms of magnitude. For all measurement configurations, the strongest response, again in terms of both magnitude and phase, is obtained for the isotropic anomalous body. However, for an anomaly in terms of solely the vertical conductivity σ_z, the response is almost similarly strong compared with the response of the isotropic anomaly, while the response to an anomaly in terms of solely σ_x or σ_y, respectively, is considerably weaker. An exception here represents the dipole-dipole array, where the magnitude responses with respect to σ_x and σ_z reach similar amplitudes.

The response curves relate to the corresponding setup's sensitivity characteristics in multiple ways:

- Strength of the response: in a depth similar to the anomaly, the shape of the sensitivities is comparable
- Characteristics of the response: For instance, the pole-pole setup shows an increasing impedance when approaching the anomaly (0 m - 2.5 m in the plot in fig. 6.2). However, when placed directly above it, the impedance drops below the initial value at places far away from the anomaly. This behavior can be observed also from the anisotropic sensitivity pattern in fig. 4.2 when reading the sensitivity values from a line at a depth corresponding to the anomaly depth used in this section.

*The sections 6.1 and 6.2 are adapted from Kenkel, J., & Kemna, A. 2017. Sensitivity of 2-d complex resistivity measurements to subsurface anisotropy. *Geophysical Journal International*, **208**(2), 1043–1057.

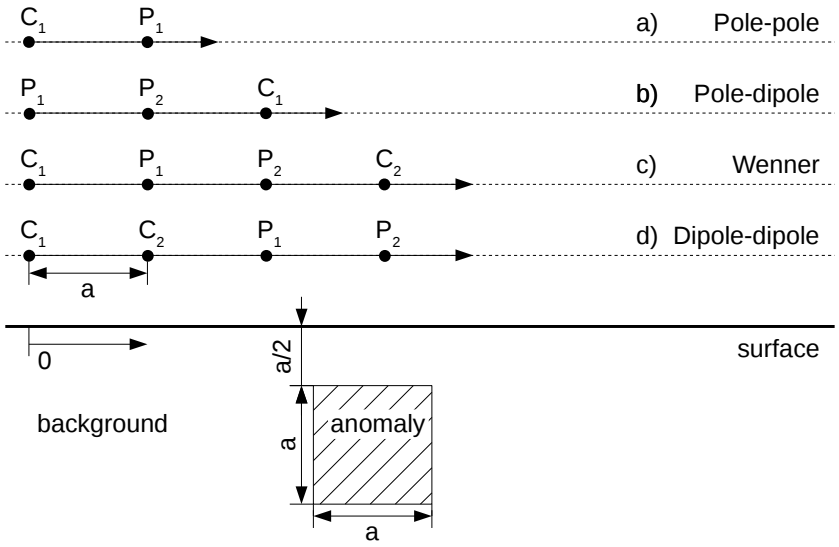

Figure 6.1: Model setup for the computation of the measurement response curves shown in Figure 6.2 for surface profiling surveys using typical measurement configurations (C and P denote current and potential electrodes) over a homogeneous, isotropic half-space with an embedded anisotropic anomaly (hatched area). The measurement configurations are moved laterally at the surface crossing the subsurface anomaly. The anomaly consists of a block with cross-sectional area $a \times a$ and infinite extension in the perpendicular (strike) direction at depth of $a/2$.

Importantly, the shape of the response curves differ. For all arrays, the qualitative behavior of the σ_y and σ_z responses is similar, and clearly different from the σ_x response. This again is in agreement with the sensitivity patterns in fig. 4.2 and fig. 4.4. For the asymmetric pole-dipole array, the asymmetry is found in all the four response curves.

6.1.2 Borehole Measurements

To investigate the measurement response curves also for cross-borehole measurements, the responses of σ_x, σ_y, σ_z (anisotropic anomalies) and σ (isotropic anomaly) for the model setup shown in fig. 6.3 were computed considering two typical measurement configurations with in-hole and cross-borehole current injection, respectively, which are moved along the boreholes, crossing an anomalous body. The results shown in fig. 6.4 again reveal important similarities in the different responses.

For the configuration with cross-hole current injection ('cross-hole B' in fig. 6.4), all types of anomalies (σ_x, σ_y, σ_z and σ) produce a response with a single peak. Notably, for the σ_z case the peak is 'negative' (i.e., exhibiting decreased impedance magnitude and increased impedance phase values). However, if the contrast of the anomaly is not known, all types of anomalies are practically indistinguishable and therefore local anisotropy cannot be resolved with this cross-borehole measurement electrode configuration.

For the cross-borehole configuration with in-hole current injection ('cross-hole A' in fig. 6.4) the different response curves again differ in terms of shape. Qualitatively similar responses are only found for the σ_x and σ_y anomalies (although with different

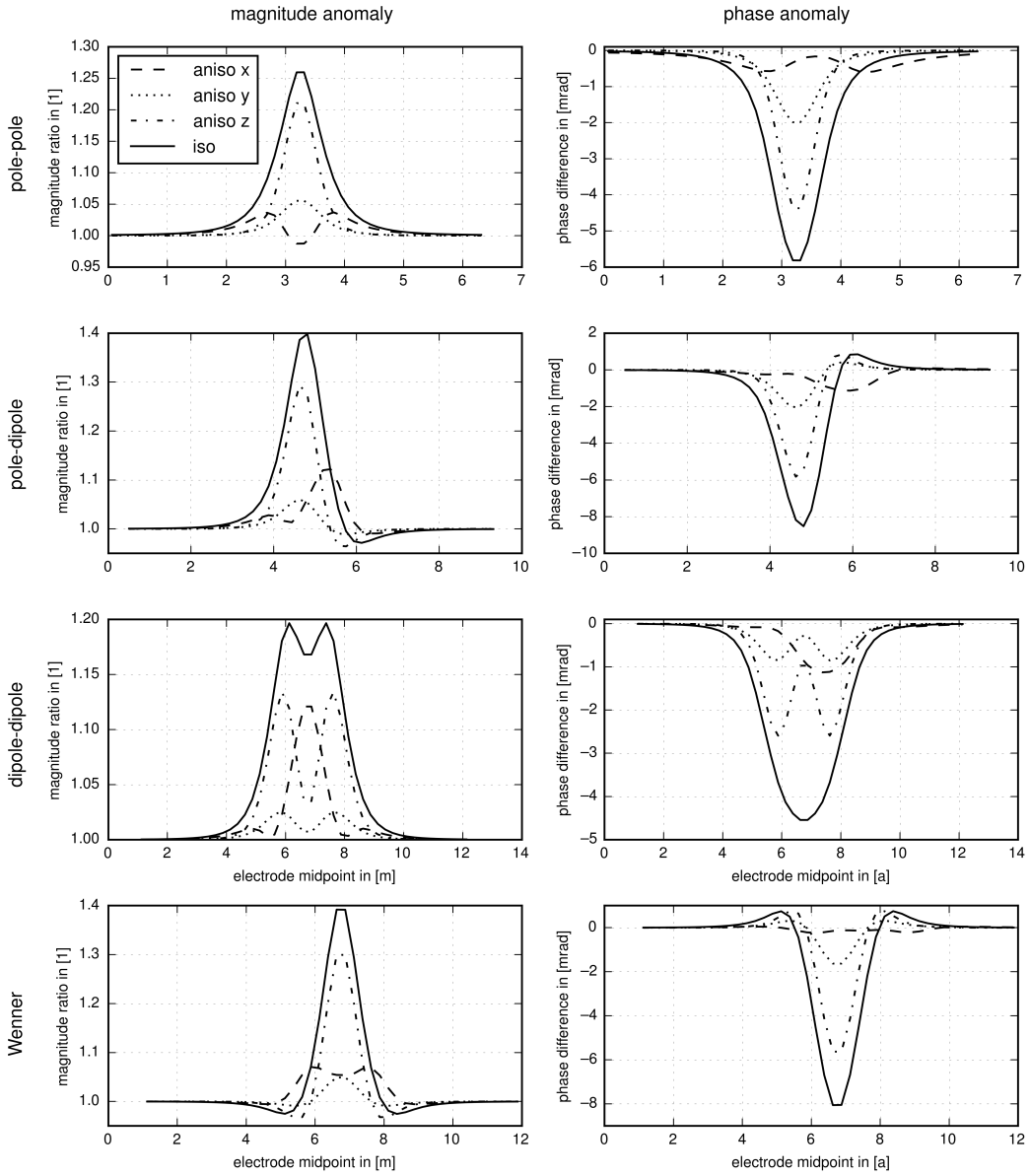

Figure 6.2: Measurement response curves for surface profiling surveys using typical measurement configurations (from top to bottom: pole-pole, pole-dipole, dipole-dipole, Wenner) over a homogeneous, isotropic half-space ($100\,\Omega\mathrm{m}$, $-10\,\mathrm{mrad}$) with an embedded anisotropic anomaly as shown in Figure 4.4. The measurement configurations are moved laterally at the surface, indicated by the midpoint of the four electrodes, crossing the subsurface anomaly. The left column shows the impedance magnitude response relative to the response without embedded anomaly (plotted as magnitude ratio) for an anomaly with different resistivity magnitude ($100\,\Omega\mathrm{m}$) in x, y, z (different anisotropic cases) and all (x, y, z; isotropic case) directions (indicated by 'aniso x', 'aniso y', 'aniso z', 'iso', respectively). The right column shows the impedance phase response relative to the response without embedded anomaly (plotted as phase difference) for an anomaly with different resistivity phase ($-50\,\mathrm{mrad}$) in x, y, z (different anisotropic cases) and all (x, y, z; isotropic case) directions (indicated by aniso x, aniso y, aniso z, iso, respectively).

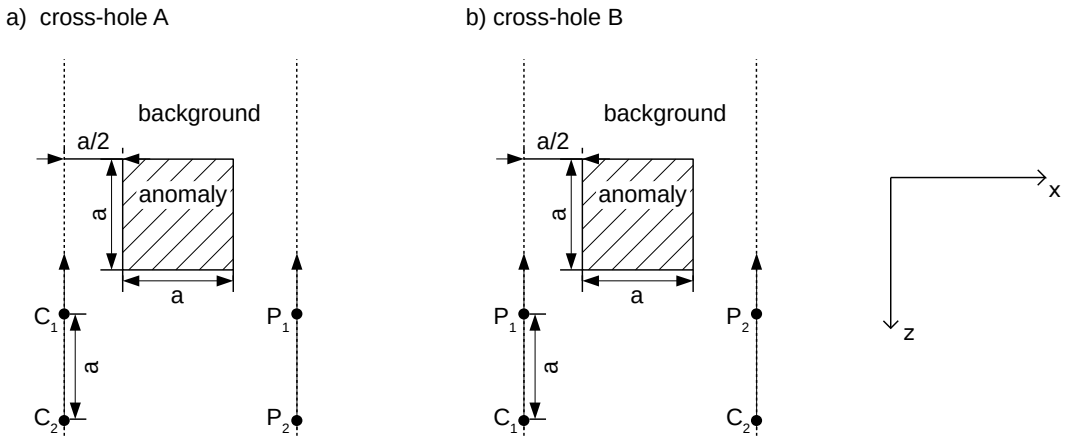

Figure 6.3: Model setup for the computation of the measurement response curves shown in fig. 6.4 for cross-borehole surveys using typical measurement configurations (C and P denote current respective potential electrodes) with in-hole (left: cross-hole A) and cross-hole (right: cross-hole B) current injections in a homogeneous, isotropic space with an embedded anisotropic anomaly (hatched area). The measurement configurations are moved vertically crossing the anomaly. The anomaly consists of a block with cross-sectional area $a \times a$ and infinite extension in the perpendicular (strike) direction, with a lateral distance of $a/2$ from each borehole.

'polarity' of the peaks) while the responses with respect to σ_z and σ each exhibit a unique behavior. This implies that this configuration is in fact capable of detecting anisotropy and, moreover, that local anomalies in σ_z can be distinguished from anomalies in σ_x or σ_y.

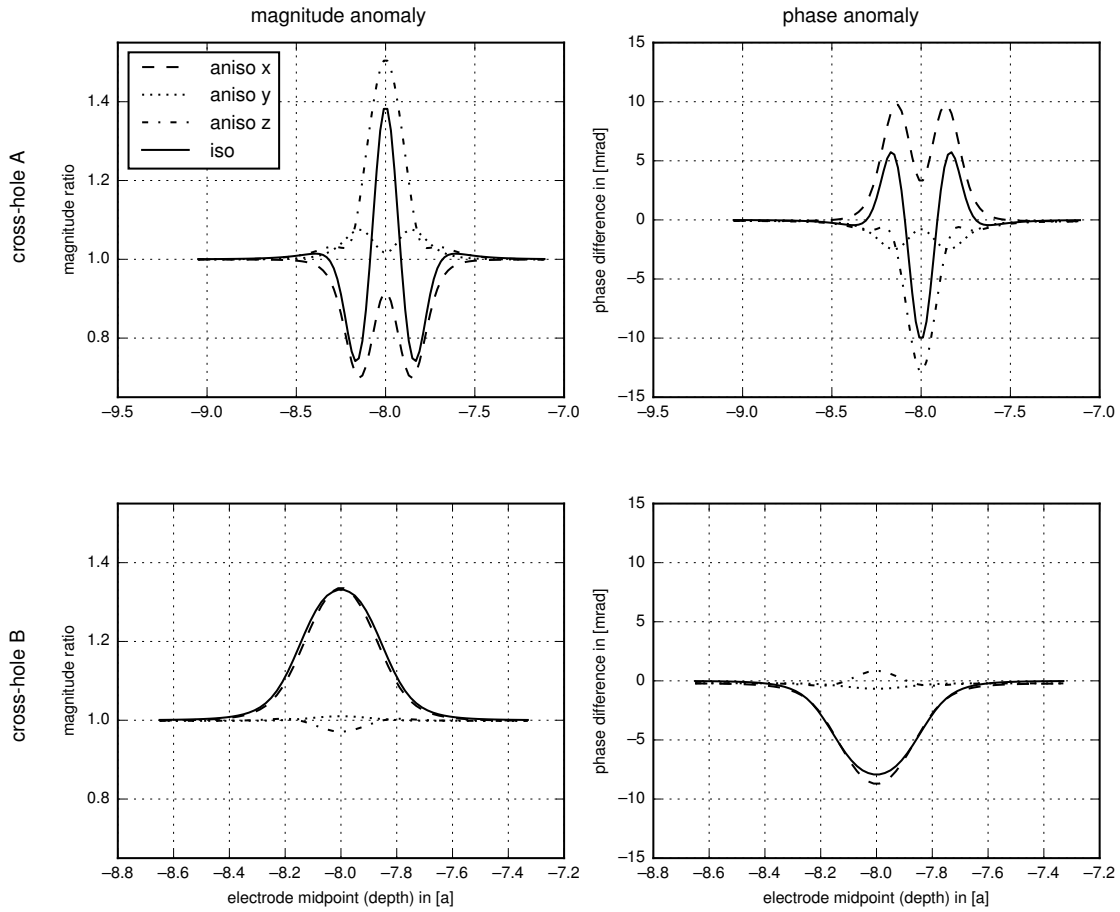

Figure 6.4: Measurement response curves for cross-borehole surveys using typical measurement configurations (top: cross-hole A, bottom: cross-hole B) in a homogeneous, isotropic half-space ($100\,\Omega\mathrm{m}$, $-10\,\mathrm{mrad}$) with an embedded anisotropic anomaly as shown in fig. 6.3. The measurement configurations are moved vertically along the boreholes, indicated by the vertical midpoint of the electrodes, crossing the anomaly. The left column shows the impedance magnitude response relative to the response without embedded anomaly (plotted as magnitude ratio) for an anomaly with different resistivity magnitude ($1000\,\Omega\mathrm{m}$) in x, y, z (different anisotropic cases) and all (x, y, z; isotropic case) directions (indicated by 'aniso x', 'aniso y', 'aniso z' and respectively 'iso'). The right column shows the impedance phase response in relation to to the response without embedded anomaly (plotted as phase difference) for an anomaly with different resistivity phase ($-50\,\mathrm{mrad}$) in x, y, z (different anisotropic cases) and all (x, y, z; isotropic case) directions (indicated by 'aniso x', 'aniso y', 'aniso z', 'iso').

6.2 Sensitivity implications for survey design and anisotropic complex conductivity inversion

In order to assess the impact of an anisotropic subsurface anomaly on IP measurements, response curves are obtained by moving certain setups along this anomaly; the presented examples cover different measurement configurations: pole-pole, pole-dipole, dipole-dipole and Wenner configurations at the surface, and dipole-dipole cross-borehole configurations with in-hole and cross-hole current injection. In the previous section, the simple scenario of an anisotropic block in an isotropic background was analyzed, from which important conclusions may be drawn regarding the general design of 2-D DC/IP surveys (i.e., with electrodes along a surface line or in boreholes in the x, z-plane) aiming at the recognition and eventually the tomographic inversion of 2-D anisotropic complex conductivity.

6.2.1 Recovering Individual Anisotropic Conductivities

If measurements are limited to the surface, anomalies in σ_x, i.e., the complex conductivity in the direction of the electrode layout, are detectable through the clearly distinct response features while responses due to σ_y or σ_z anomalies are similar in most cases in terms of their response patterns. Despite this, the anisotropy ratios $\frac{\sigma_x}{\sigma_y}$ or $\frac{\sigma_h}{\sigma_v}$ can be explored with the collinear surface arrays mentioned before. To unambiguously collect information on σ_z, measurement configurations with the current dipole oriented in the z direction would be needed, implying the use of borehole electrodes. However, cross-borehole configurations with 'zero-offset' cross-hole current injection are not beneficial in this matter. Even if combined surface and borehole 2-D electrode layouts are employed, the direct sensing of σ_y, i.e., the complex conductivity in the strike direction, is virtually impossible. The latter would require the extension of the electrode array in strike direction, i.e., the use of 3-D data measurement layouts. These fundamental limitations could also be taken into account in the parametrization of the anisotropic complex conductivity inverse problem, for instance by assuming $\sigma_y = \sigma_x$ or $\sigma_y = \sigma_z$ (depending on additional geological *a priori* information) in the inversion, or by the incorporation of corresponding penalties in the underlying objective function.

6.2.2 Anisotropy Ambiguity at Different Scales

Another important aspect in an anisotropic inversion is the relation between the size of (anisotropic) parameter cells and the spatial resolution, given the fact that anisotropy per se is a scale-dependent phenomenon. As illustrated in figures 6.5 and 6.6 for the model considered in the above sections (cf. figures 6.1 and 6.2), an anisotropic model at a certain scale can be equivalently described by a smaller-scale heterogeneous model that consists solely of isotropic parameters. In the example below, the anisotropic block is replaced by alternating isotropic layers whose resistivity magnitude values are chosen in a way that exactly the anisotropic resistivity values of the block are obtained by the application of simple mixing models* at the scale of the block (see e.g., Kenkel *et al.*, 2012). As the layer thickness becomes small in relation to the electrode separation

*Only for magnitudes. As pointed out in (Kenkel *et al.*, 2012), anisotropic phase angles cannot be explained equivalently through isotropic layering.

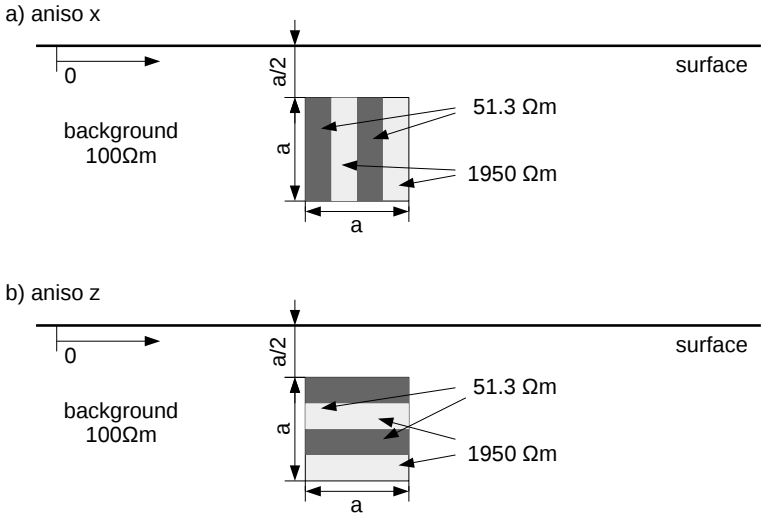

Figure 6.5: Model setup for the computation of the measurement response curves shown in figure 6.6 for a dipole-dipole surface survey as depicted in figure 6.1 over a homogeneous, isotropic half-space ($100\,\Omega\mathrm{m}$, $-10\,\mathrm{mrad}$) with an embedded anomaly consisting of alternating isotropic layers. The resistivity magnitude values of the alternating layers ($51.3\,\Omega\mathrm{m}$ and $1950\,\Omega\mathrm{m}$) are chosen in such a way that a resistivity of $100\,\Omega\mathrm{m}$ (i.e., equal to background) and $1000\,\Omega\mathrm{m}$ results in the direction parallel and perpendicular to the respective layering (see e.g., Kenkel *et al.*, 2012); resistivity phase values of the alternating layers are equal to the background phase value ($-10\,\mathrm{mrad}$). With decreasing layer thickness the alternating layers effectively form an anisotropic anomaly equivalent to the model shown in figure 6.1. (a) Layering perpendicular to x direction ('aniso x'), (b) layering perpendicular to z direction ('aniso z').

of the measurement array, which determines the scale of significant spatial sensitivity variations, the response of the isotropic layers becomes identical to the response of the anisotropic block (Figure 6.6). From an inversion point of view this means that an anisotropic parametrization effectively accounts for any (unresolvable) heterogeneity below the measurement's scale.

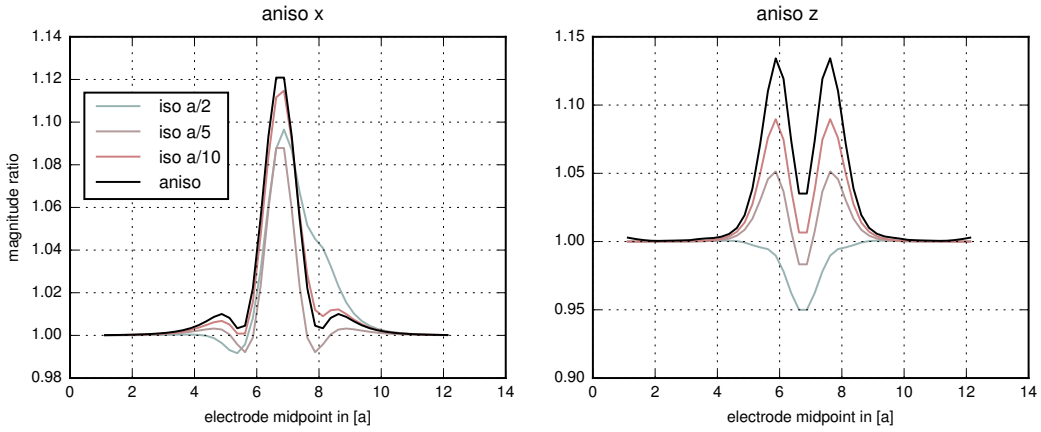

Figure 6.6: Measurement response curves for a dipole-dipole surface survey over the model shown in figure 6.5 with layering in the anomalous region perpendicular to the x direction (left: 'aniso x') and perpendicular to the z direction (right: 'aniso z') for different thicknesses of the alternating layers (blue: $a/2$, purple: $a/5$, red: $a/10$). The black curve shows the corresponding response from figure 6.2 for the equivalent case with anomalous resistivity magnitude in x direction ('aniso x') and z direction ('aniso z'), for comparison. As the layer thickness decreases, the response of the alternating isotropic layers approaches the response of the anisotropic block in both cases.

6.3 Isotropic Inversion of Anisotropic Synthetic Data

As a motivation for anisotropic inversion, an isotropic inversion of data from an anisotropic model is presented. The original model contains a dike structure and electrodes at the surface and in two boreholes, virtually surrounding the anomaly structure (see the bottom fig. 6.11 for the original magnitude and phase angle model).

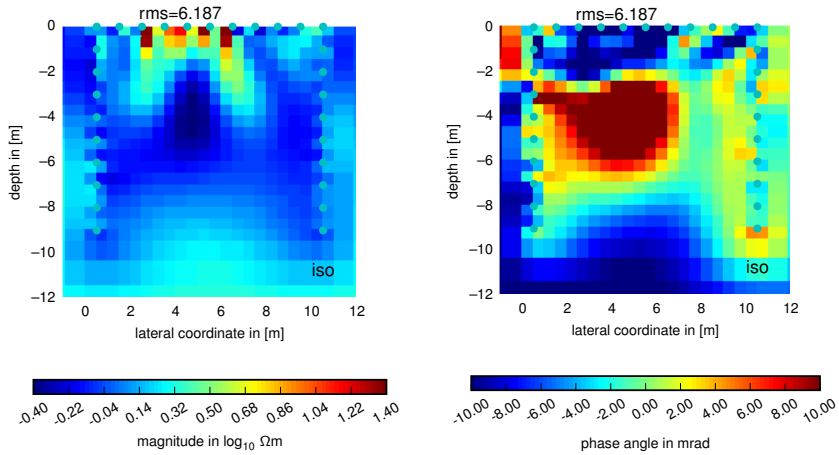

Figure 6.7: Magnitude (left) and phase angle (right) recovered/inverted resistivity sections of the data from the anisotropic model in fig. 6.11. Turquoise dots represent electrodes

The recovered magnitude section in fig. 6.7 does not correctly locate the anomaly

position or strength and exhibits strong artifacts close to the electrodes at the surface and in the left borehole. The recovered phase angle section in fig. 6.7 recovers the anomaly position but fails to estimate its original phase angle. Moreover, strong artifacts are visible throughout the section. The final data-model misfit RMS is very high, suggesting that the model is not capable of interpreting the data. In this case, the isotropic inversion of data from an anisotropic model cannot be considered successful.

6.4 Anisotropic Inversion of Synthetic Data

In this section, inversion examples are presented. Special consideration is given to the anisotropy lambda factor λ_a with regard to an optimal inversion result. Here, the focus lies on synthetic inversions which can be tuned very easily and which provide an excellent data quality. Moreover, ground-truth is easily available in this context, since the synthetic data is computed over a chosen subsurface model.

6.4.1 Isotropic Models

As a test for the anisotropic inversion algorithm, data from an isotropic model is inverted. The model is depicted in fig. 6.8

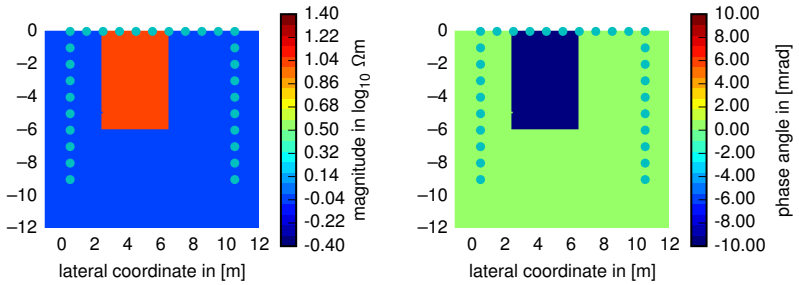

Figure 6.8: Magnitude (left) and phase angle (right) sections of the original model's resistivity of a surface setup with 29 electrodes with $1\ \mathrm{m}$ spacing in two boreholes and at the surface. The model contains a vertical dike with a resistivity contrast only in the horizontal (x,y) directions. The resistivity magnitudes are set to isotropic $10^0\ \Omega m$ for the background and $10^1\ \Omega m$ for the dike structure. The phase angle is set to $0\ \mathrm{mrad}$ at the background and anisotropic $-10\ \mathrm{mrad}$ inside the dike. The synthetic data consists of all applicable dipole-dipole, cross-borehole and surface-to-borehole measurements.

The inverted sections in fig. 6.9 (magnitude) and fig. 6.10 are computed for various anisotropy penalty values, λ_a, ranging over three decades. With the highest anisotropy penalty, both magnitude and phase angle sections exhibit virtually isotropic results (see table 6.1) inside and outside of the model block. When lambda is decreased, the inversion results generally contain more anisotropy. However, even with the smallest λ_a, most of the original model's isotropy is correctly recovered. Extracted values for magnitude and phase angle at crucial points in the recovered model can be found in table 6.1.

location in m		magnitudes in $\log_{10}\Omega m$			phase angles in mrad			info
x	z	$\|\rho_x\|$	$\|\rho_y\|$	$\|\rho_z\|$	$\angle\rho_x$	$\angle\rho_y$	$\angle\rho_z$	
-	-	1	1	1	-10	-10	-10	model inside dike
4.25	-1.75	0.99	0.73	0.81	-12.2	-5.5	-8.1	max. inside dike
5.75	-5.75	0.28	0.21	-0.21	-1.4	1.5	-0.6	min. inside dike
-	-	0	0	0	0	0	0	model outside dike
5.75	-9.25	-0.09	0.11	0.03	-0.9	2.4	1.6	outside dike

Table 6.1: Inverted resistivities (magnitude: $\|\rho_i\|$, phase angle $\angle\rho_i$) with the least anisotropy penalty $\lambda_a = 10^{-7}$ of the data recorded over the model in fig. 6.8 at selected points.

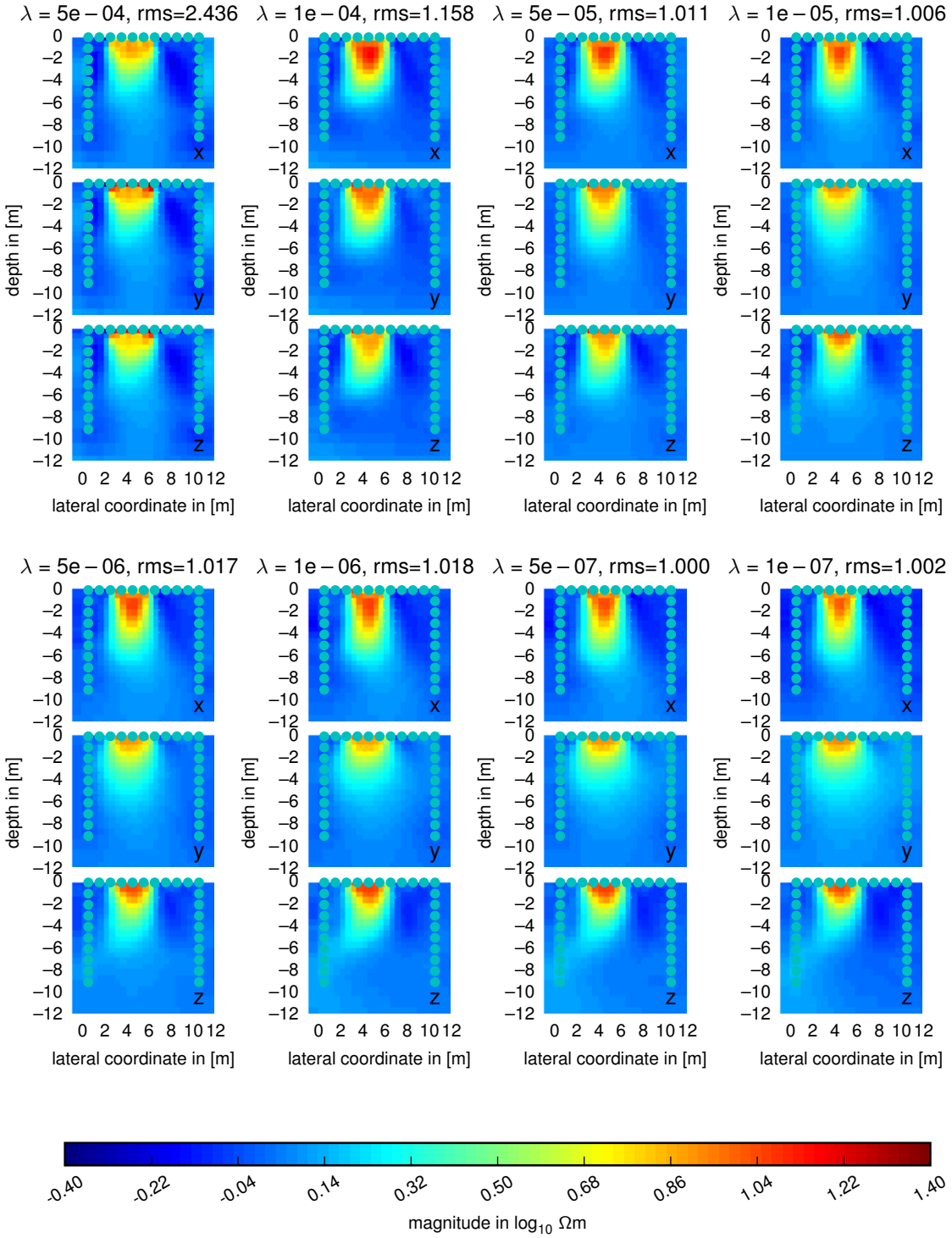

Figure 6.9: Inversion results of the dike model in fig. 6.8 computed with multiple anisotropy lambda values λ_a: $5{\cdot}10^{-4}$ (top left), 10^{-4}, ..., $5{\cdot}10^{-7}$, 10^{-7} (bottom right). For comparison, the depicted sections represent the third iteration step of each inversion and include the corresponding data misfit RMS. In plots for each anisotropy lambda value, the x, y and z resistivity magnitude sections are shown. All inversions use the data from the original model with added Gaussian noise in the range of 1% of the measured data plus 10^{-6} Ω, which is also their target fit (RMS$= 1$). The color range is matched with the original model in fig. 6.8.

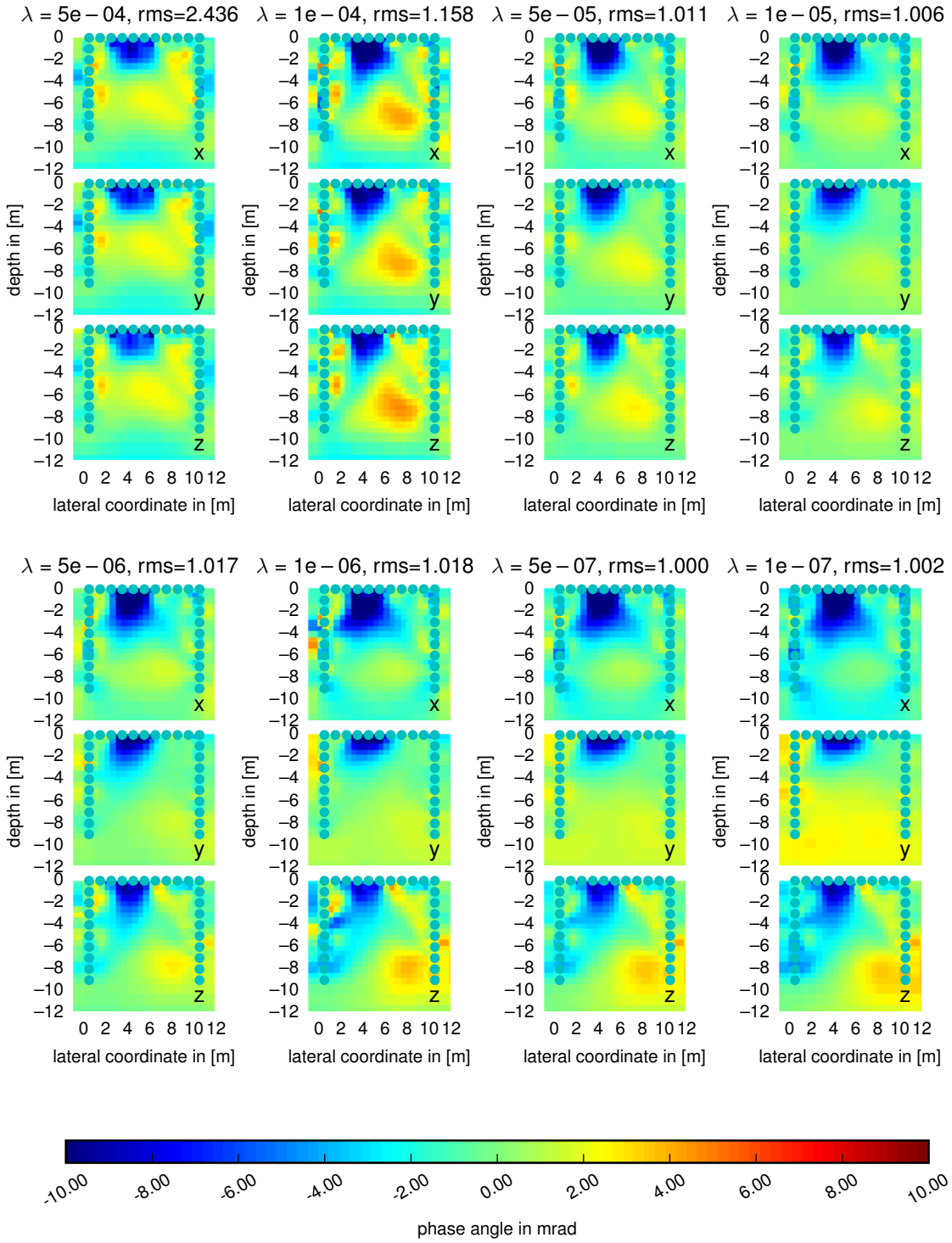

Figure 6.10: Phase angle of the inverted sections of the dike model in fig. 6.8. The assumed phase angle error is 1 mrad. For details, see fig. 6.9.

6.4.2 Anisotropic Models

6.4.2.1 Subsurface Dike Model

One key aspect of inverting data that was recorded over anisotropic subsurfaces is setting the anisotropy penalty properly. Regarding this, the expected behavior would be a more isotropic inversion result when a large anisotropy lambda factor λ_a is chosen.

In this section, a model with a vertical dike is observed. The model is shown in fig. 6.11. The dike is specified to have anisotropic resistivities and is placed into an isotropic and homogeneous background. The resistivities inside the dike are chosen to be more resistive in the horizontal directions. This situation corresponds with a vertical layering, which can be interpreted as a system of vertical tubes.

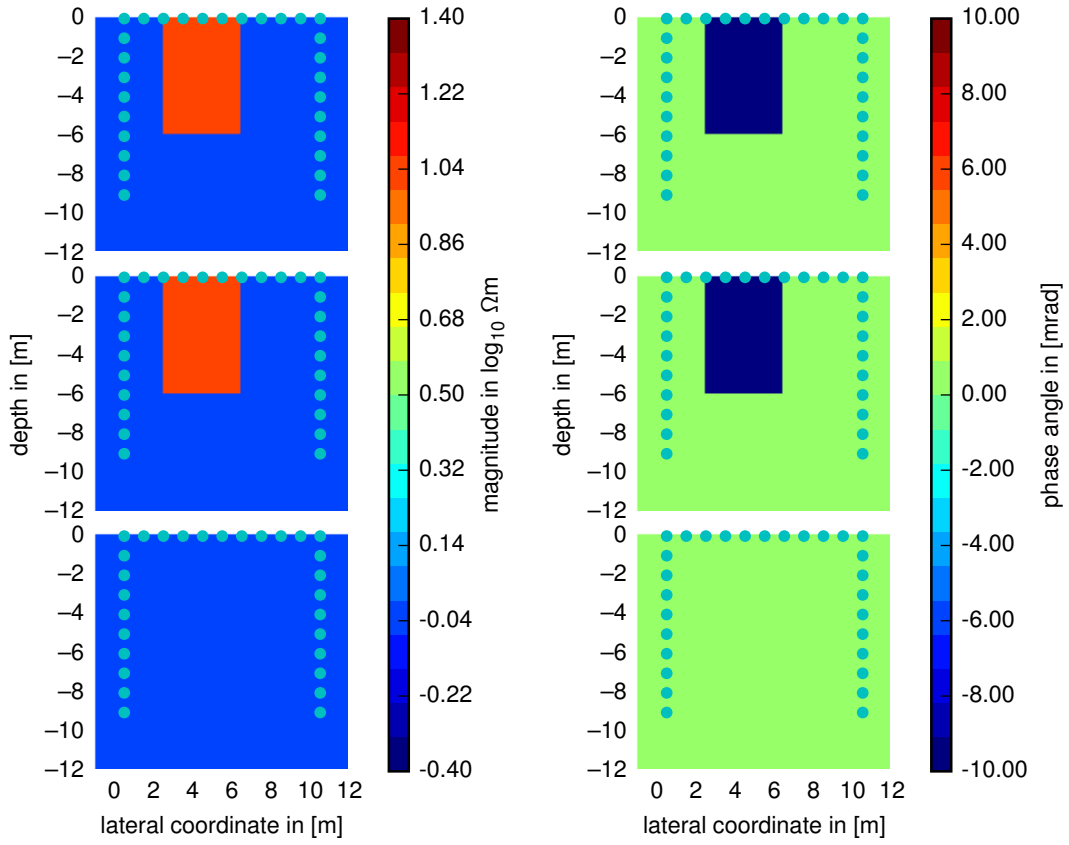

Figure 6.11: Magnitude (left) and phase angle (right) sections of the original model of a surface setup with 29 electrodes with 1 m spacing in two boreholes and at the surface. X, y and z resistivities are shown in the top, middle and bottom panel, respectively. The model contains a vertical dike with a resistivity contrast only in the horizontal (x,y) directions. The resistivity magnitudes are set to isotropic $10^0\ \Omega m$ for the background and to $(10^1, 10^1, 10^0)\ \Omega m$ for the dike structure. The phase angle is set to isotropic 0 mrad at the background and anisotropic $(-10, -10, 0)$ mrad inside the dike. The synthetic data consists of all applicable dipole-dipole, cross-borehole and surface-to-borehole measurements.

The inverted sections are shown in fig. 6.12 and fig. 6.13. Starting with the magnitude sections, the dike location is resolved with all anisotropy penalties λ_a. However, the

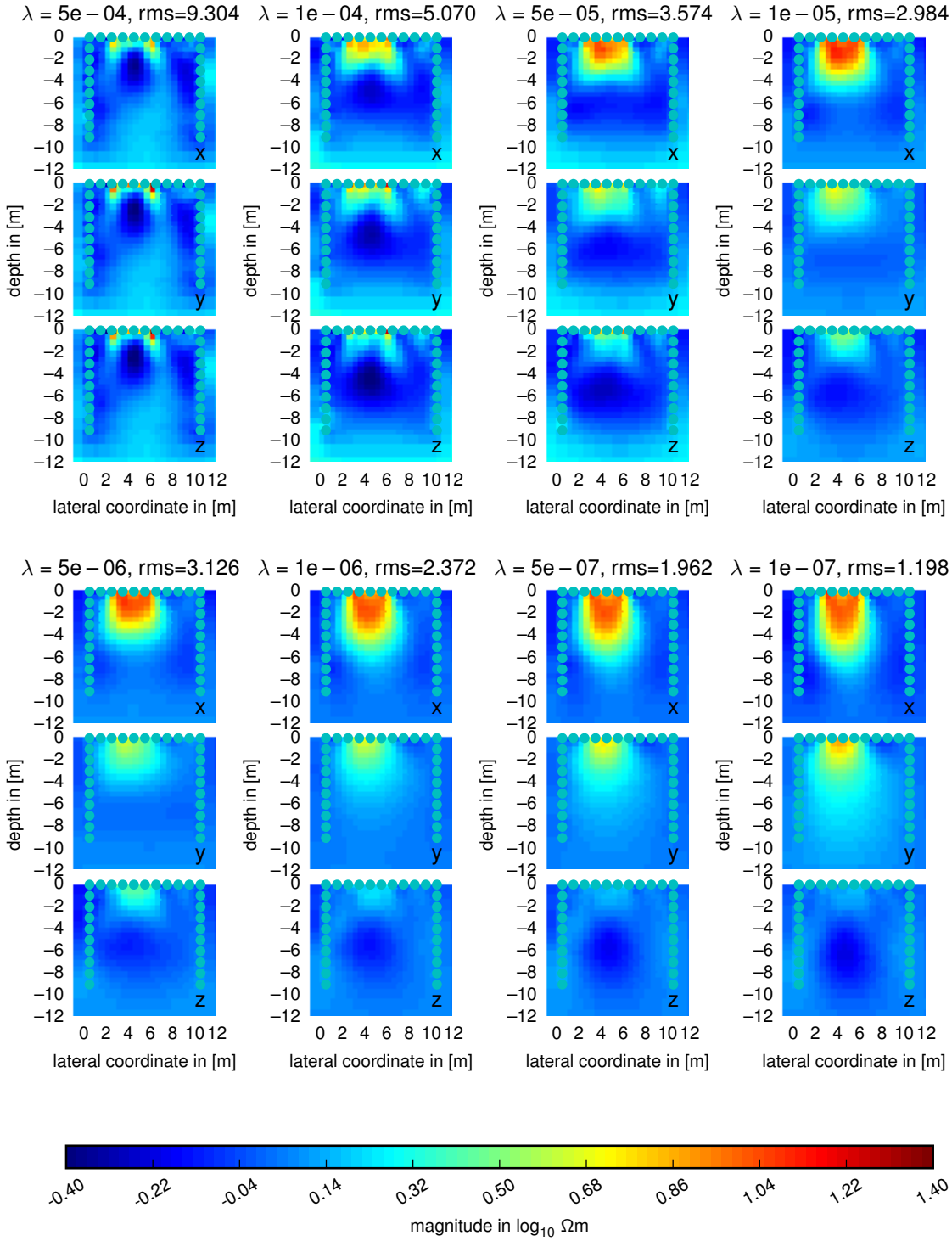

Figure 6.12: Inversion results of the dike model in fig. 6.11 computed with multiple anisotropy lambda values λ_a: $5{\cdot}10^{-4}$ (top left), 10^{-4}, ..., $5{\cdot}10^{-7}$, 10^{-7} (bottom right). For comparison, the depicted sections represent the third iteration step of each inversion and include the corresponding data misfit RMS. In plots for each anisotropy lambda value, the x, y and z resistivity magnitude sections are shown. All inversions use the data from the original model with added Gaussian noise in the range of 1% of the measured data plus 10^{-6} Ω, which is also their target fit (RMS$= 1$). The color range is matched with the original model in fig. 6.11.

location in m		magnitudes in $\log_{10}\Omega m$			phase angles in $mrad$			info
x	z	$\|\rho_x\|$	$\|\rho_y\|$	$\|\rho_z\|$	$\angle\rho_x$	$\angle\rho_y$	$\angle\rho_z$	
-	-	1	1	0	-10	-10	0	model inside dike
3.25	-0.25	1.10	0.75	0.14	-11.2	-13.3	0.98	max. inside dike
4.75	-5.75	0.50	0.29	-0.21	1.7	0.4	3.4	min. inside dike
-	-	0	0	0	0	0	0	model outside dike
1.75	-9.25	-0.01	0.13	0.01	-4.4	3.0	3.2	outside dike

Table 6.2: Inverted resistivities (magnitude: $\|\rho_i\|$, phase angle $\angle\rho_i$) with anisotropy penalty $\lambda_a = 10^{-7}$ of the data recorded over the model in fig. 6.11 at selected points.

results with the largest anisotropy penalty, $\lambda_a = (5\cdot10^{-4}, 10^{-4})$, are strongly constrained to isotropy. In this situation, the algorithm tries to produce isotropic inversions, which is not feasible for this data. For the regarded inversions, the data fit is very bad with RMS values of 9.3 and 5.1. When setting the anisotropy penalty to smaller values, the data gets interpreted more consistently, resulting in a better fit down to 1.2 for $\lambda_a = 10^{-7}$. These sections represent the original model adequately, i.e., the x magnitude reaches a maximum of $10^{1.1}\ \Omega m$ at $x = 3.25\ m, z = -0.25\ m$ (slightly over-estimated), while the z magnitude at the same point is $10^{0.1}\ \Omega m$ (see table 6.2 for a summary). The smallest z magnitude value inside the dike is $10^{-0.2}\ \Omega m$ at $x = 4.75\ m, z = -5.75\ m$. The y magnitude exhibits a weaker agreement with the original model, with a maximum value inside the dike of $10^{0.75}\ \Omega m$. However, the shape of the dike is again represented in the inverted section. For this model, an anisotropy penalty value of less than $\lambda_a = 10^{-5}$ seems to be favorable since the inverted sections sufficiently start reconstructing the model.

A similar interpretation may be made for the phase angle of the inverted sections. Consequently, the inversion algorithm computed almost isotropic sections for the above noted high values of λ_a, i.e., $\lambda_a = (5\cdot10^{-4}, 10^{-4}, 5\cdot10^{-3})$ and more anisotropic sections for the small λ_a values. Also, the latter inverted sections exhibit a decent agreement with the original model. From the perspective of a phase angle interpretation, an anisotropy penalty of λ_a less or equal 10^{-6} seems to be favorable.

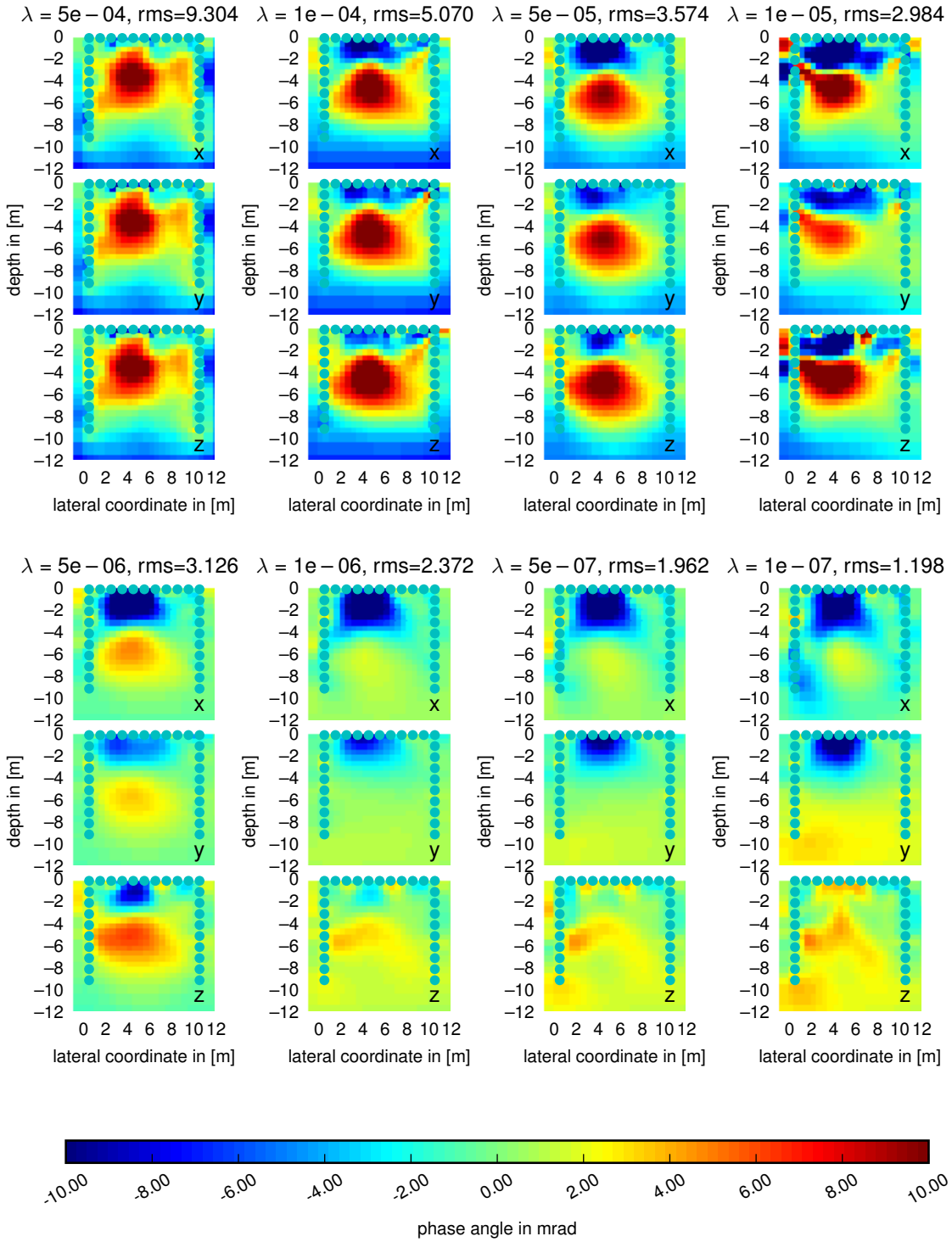

Figure 6.13: Phase angle of the inverted sections of the dike model in fig. 6.11. The assumed phase angle error is 1 mrad. For details, see fig. 6.12

.

6.4.2.2 Subsurface Dike Model - Horizontal Conductivity and Anisotropy Ratio

According to section 5.4.3, the model data in fig. 6.11 can also be inverted targeting the horizontal ($\rho_h = \rho_x = \rho_y$) resistivity and the anisotropy ratio $\lambda_a = \frac{\sigma_x}{\sigma_y}$. In this case, the anisotropy penalty is only set indirectly through favoring a smooth anisotropy section, i.e., spatial smoothness in the horizontal-vertical anisotropy λ_a is the inversion cost function target along with the spatial smoothness of the horizontal resistivity ρ_h. In the case of the regarded algorithm, spatial horizontal resistivity and anisotropy are equally taken into account. The resulting inversion with resistivity magnitude and phase angle in horizontal and vertical direction is shown in fig. 6.14. The plots reveal a good model representation where a block of high resistivity magnitude and low phase angle appears in the images for the horizontal direction. Corresponding with the original model, both resistivity magnitude and phase angle exhibit structures with less deviation from the background. However, in the case of the resistivity magnitude, the original values inside the block $(\rho_h, \rho_v) = (10^1, 10^0)\ \Omega m$ are underestimated in the horizontal direction and overestimated in the vertical direction with the maximum values $(\rho_h, \rho_v) = (10^{0.64}, 10^{0.34})\ \Omega m$. Similar, the phase angle is underestimated in horizontal direction and overestimated in vertical direction with the minimum values $(\varphi_h, \varphi_v) = (-7.3, -4.5)$ mrad. Additionally, an artificial anomaly with positive values of up to $\varphi_v = -5.1$ mrad appears in vertical phase angle section.

6.4.2.3 Subsurface Dike Model II

A model similar to the one in fig. 6.11 is shown in fig. 6.15. In contrast to the section above, this model consists of a homogeneous half-space with an embedded dike with lower resistivity in x and y direction.

The inversion result again correlates with the synthetic data in fig. 6.15 in the shape of the anomaly. Also, the magnitude section exhibits a similar optimal anisotropy penalty of less than $\lambda_a = 10^{-5}$, where the dike is resolved adequately. The phase angle sections again resemble the original model decently. Here, the optimal value for λ_a would also be less than 10^{-5}.

In summary, the inversion algorithm is capable of resolving the initial anisotropic model. Consideration has to be given to the choice of an optimal anisotropy penalty λ_a. The RMS value is generally observed to be higher for large values of λ_a, which might be a consequence of the inherent anisotropy within the data. As was shown in Kenkel *et al.* (2012), isotropic inversion of anisotropic data — which is resembled through large

location in m		magnitudes in $\log_{10}\Omega m$			phase angles in $mrad$			info
x	z	$\|\rho_x\|$	$\|\rho_y\|$	$\|\rho_z\|$	$\angle\rho_x$	$\angle\rho_y$	$\angle\rho_z$	
-	-	0	0	1	0	0	-10	model inside dike
3.25	-0.25	0.06	-0.09	1.09	-0.6	-2.5	-8.9	max. inside dike
4.75	-5.75	0.72	0.79	0.79	-7.0	-6.9	-7.1	min. inside dike
-	-	1	1	1	-10	-10	-10	model outside dike
1.75	-9.25	0.94	0.89	0.74	-9.1	-8.3	-7.0	outside dike

Table 6.3: Inverted resistivities (magnitude: $\|\rho_i\|$, phase angle $\angle\rho_i$) with anisotropy penalty $\lambda_a = 10^{-7}$ of the data recorded over the model in fig. 6.15 at selected points.

anisotropy penalties — leads to artifacts. These artifacts can be observed in the inverted sections and typically result in large RMS values.

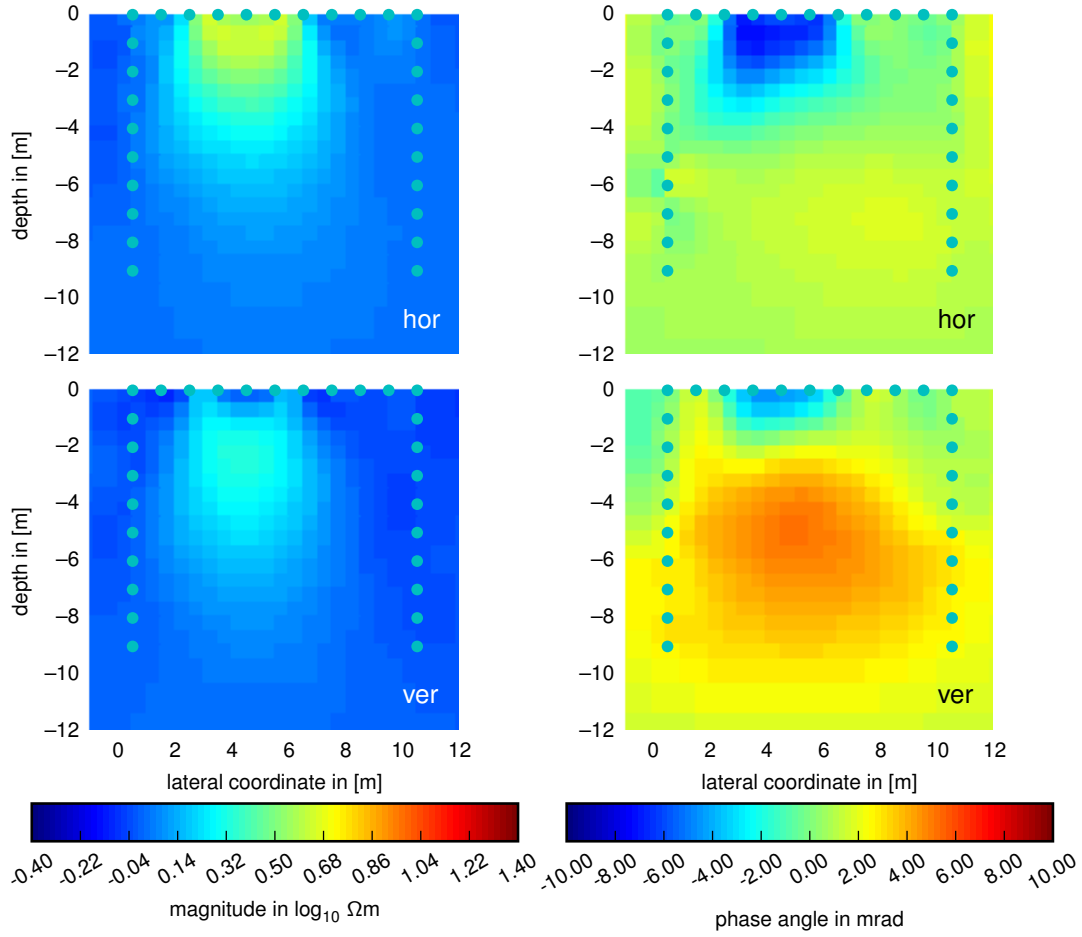

Figure 6.14: Magnitude (left) and phase angle (right) inversion results of the dike model in fig. 6.11 computed with horizontal conductivity and anisotropy ratio. The top and bottom panels represent the horizontal and vertical sections, respectively. All inversions use the data from the original model with added Gaussian noise in the range of 1% of the measured data plus 10^{-6} Ω, which is also their target fit (RMS$= 1$). The color range is matched with the original model in fig. 6.11.

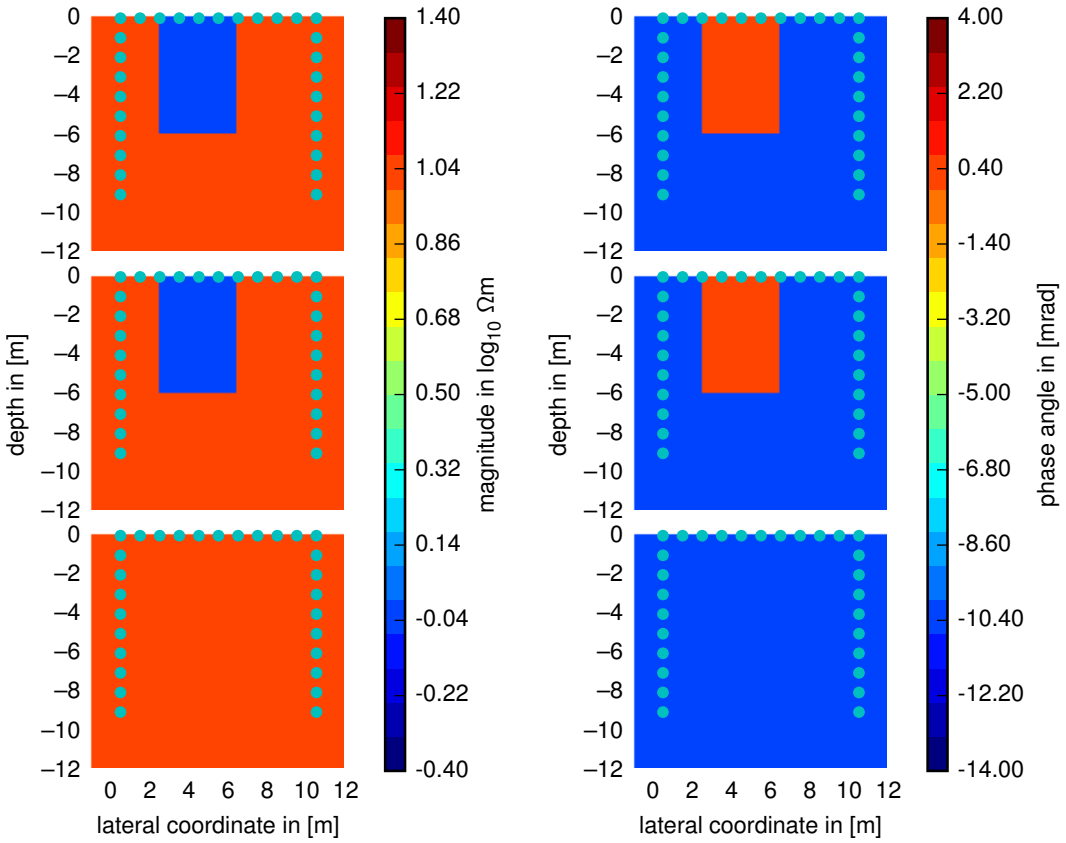

Figure 6.15: Magnitude and phase angle sections of the original model. The resistivity magnitudes are set to isotropic $10^1\ \Omega m$ for the background and to $(10^0, 10^0, 10^1)\ \Omega m$ for the dike structure. The phase angle is set to isotropic -10 mrad at the background and anisotropic $(0, 0, -10)$ mrad inside the dike. For details, see fig. 6.11.

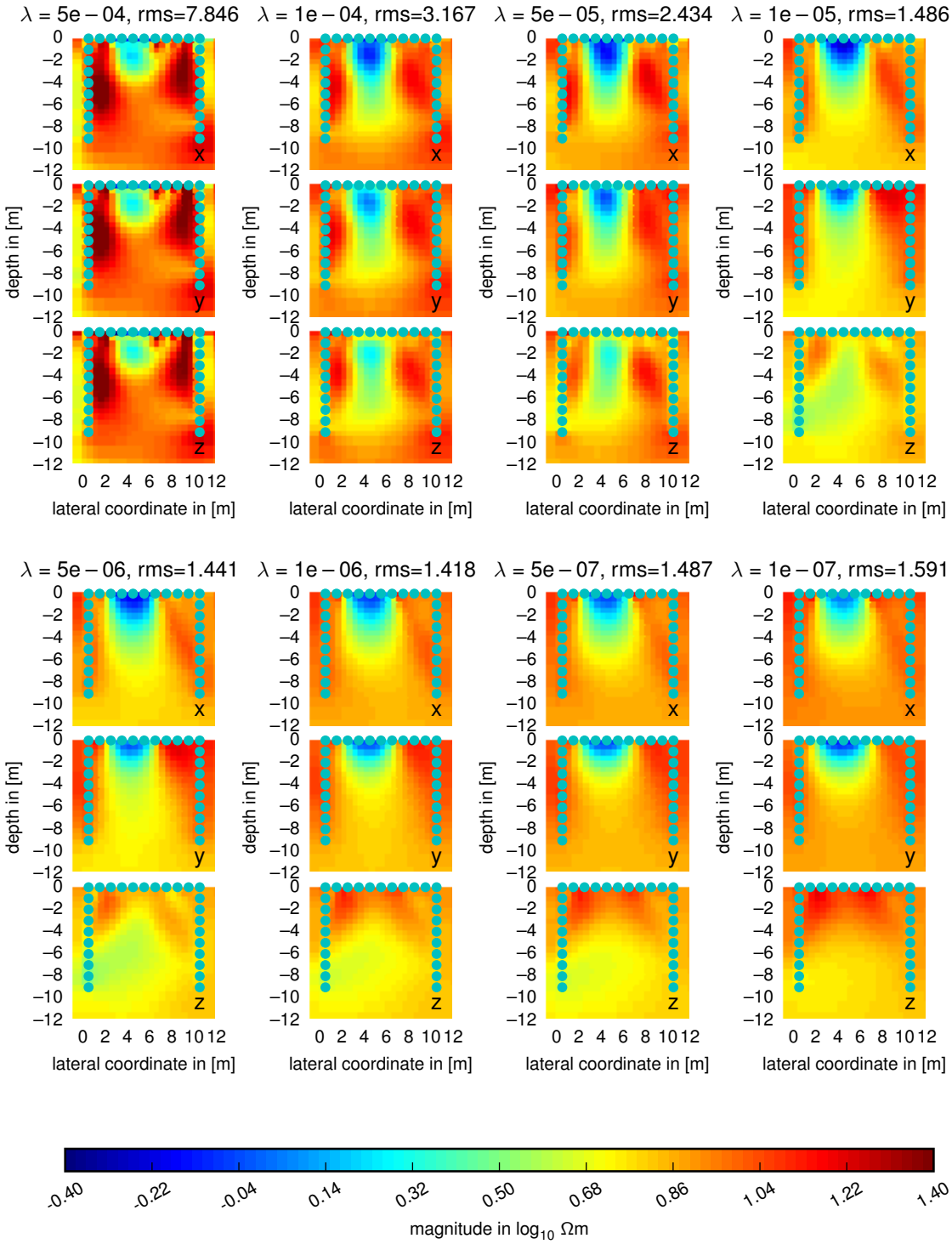

Figure 6.16: Inversion results of the dike model in fig. 6.15 computed with multiple anisotropy lambda values. For details see fig. 6.12.

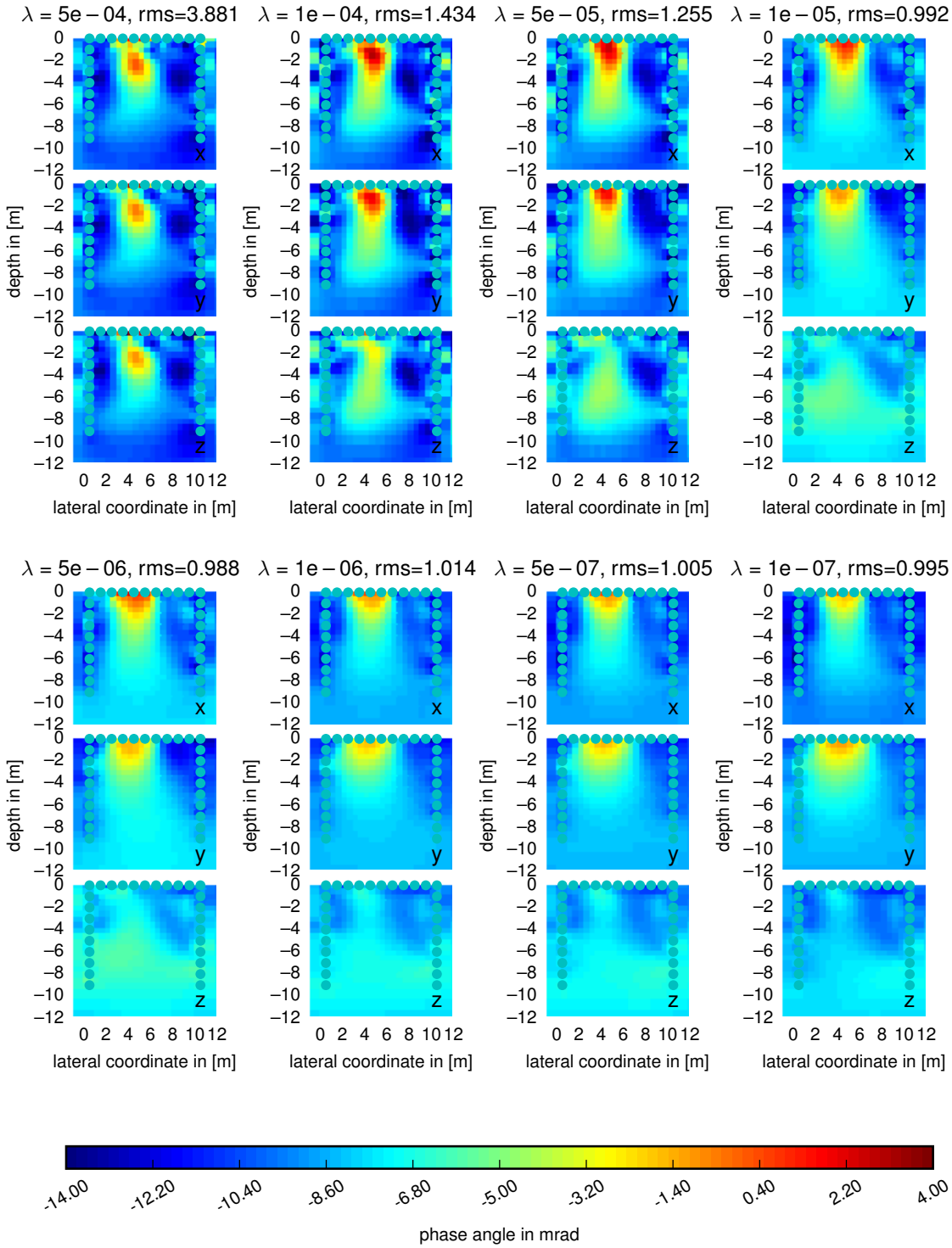

Figure 6.17: Phase angle of the inverted sections of the dike model in fig. 6.11. The assumed phase angle error is 1 mrad. For details see fig. 6.16.

6.4.2.4 Subsurface Dike Model with Selected/Less Data

The original set of setups consists of

- dipole-dipole
- borehole-to-surface and
- cross-borehole

measurements. In this section, each of these individual subsets are computed over the dike model (fig. 6.11) as input data for an inversion. Figures 6.18 exhibit the inverted data as magnitude and phase angle sections. The different subsets offer varying restoration capabilities:

a) The full set of measurements restores the location as well as magnitude and phase angle of the dike in x and z direction. The y magnitude, however, is blurred and appears to contain an average of the x and z values, which could result from the low sensitivity in y direction (see sections 4.3 and 6.1).
b) The borehole-to-surface subset again recovers the location, magnitude and phase angle similar to the full set. Nonetheless, the resistivity magnitudes in x and y direction are underestimated. The z phase angle section contains artifacts, which can be noticed also in the full set inversion (a).
c) The cross-borehole subset inversion offers a blurred reconstruction of the dike model. However, it is capable of locating the anisotropy despite strongly underestimating the x and y resistivity. The phase angle contains heavy artifacts mainly in x and z direction. The bad resolution may be based on the "band" structure of the corresponding sensitivity (see fig. 4.3), which does not allow for any reconstruction of structures in x direction.
d) The dipole-dipole subset inversion meets the original resistivity magnitude and phase angle values close to the electrodes. It overestimates the z resistivity magnitude. Overall, the reconstruction appears limited to the direct vicinity of the electrodes, which could be caused by the shallow penetration depth of dipole-dipole measurements.

Generally, the borehole-to-surface setups offer the best reconstruction capabilities and allow for being closest to the inversion with the full setups set. The reconstructed sections of all setups appear blurred between all the subset's inversions, with the strongest influence being the borehole-to-surface setups, followed by dipole-dipole and cross-borehole setups in descending order.

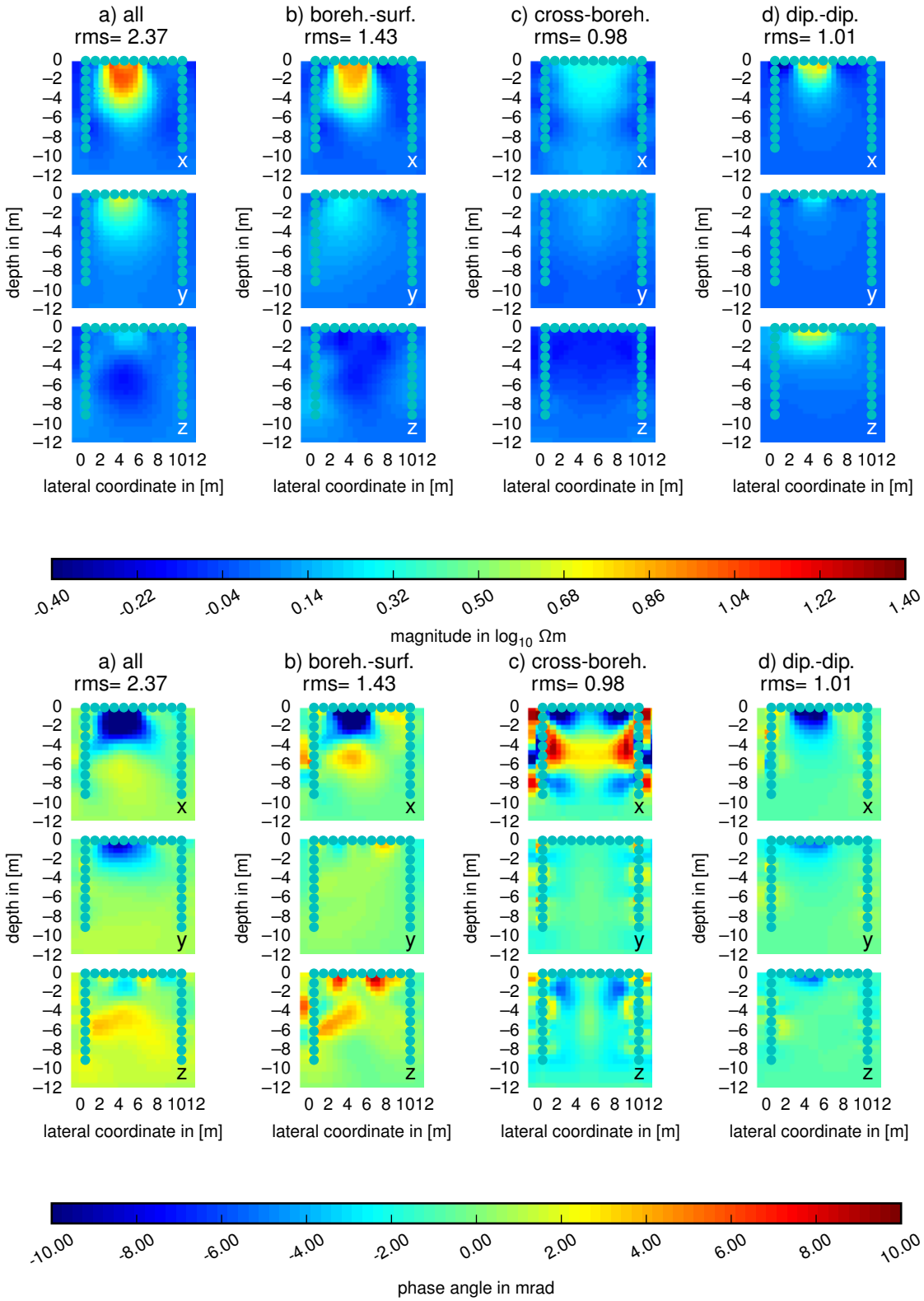

Figure 6.18: Inversion results (top: magnitude, bottom: phase angle) of the dike model in fig. 6.15 computed with different subsets of all measurement setups:

- a full set/all measurements
- b borehole-to-surface setups
- c cross-borehole setups
- d dipole-dipole setups.

All inversions are carried out with an anisotropy lambda of $1E-6$.

6.4.2.5 Surface Electrodes Model I: Horizontal Layer

In this section, a model with surface electrodes is analyzed. The original model is shown in fig. 6.19. It contains a layer with anisotropic complex conductivity magnitude $(10^0, 10^0, 10^1)\ \Omega m$ and phase angle $(0, 0, -10)$ mrad inside an isotropic background with $10^0\ \Omega m, 0$ mrad.

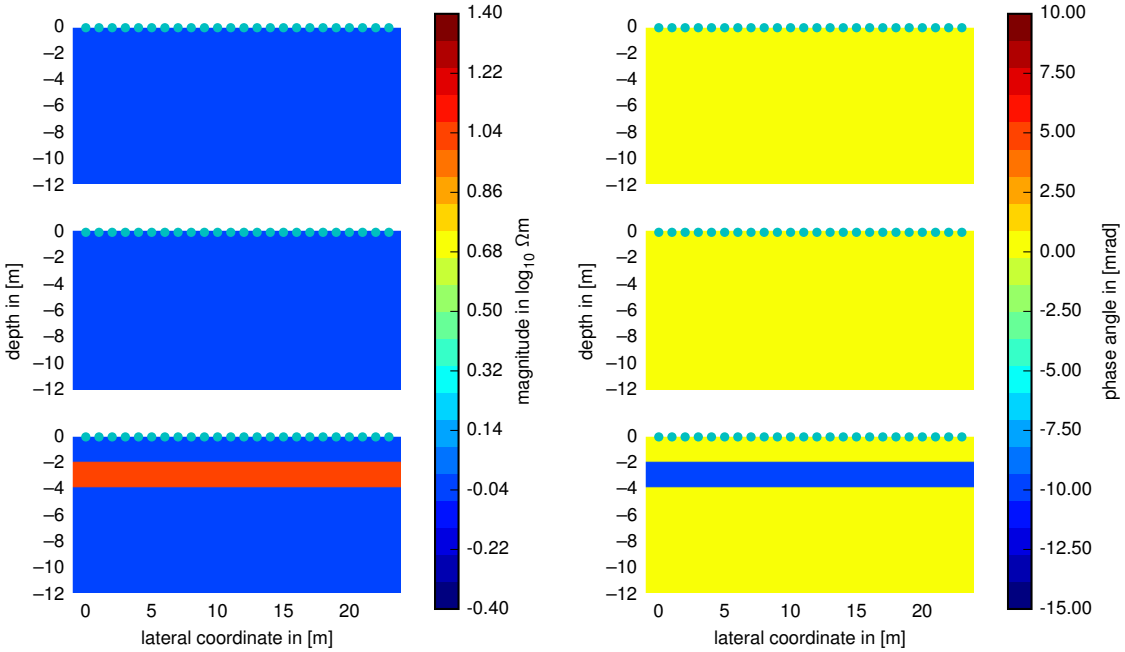

Figure 6.19: Original model of the surface setup with 24 collinear electrodes with 1 m spacing. The synthetic measurements are carried out with all feasible dipole-dipole setups with skip-0 to skip-6 offsets. The inversion target fit was set to 1% relative and 1E-4 Ω absolute error. Gaussian noise of 1% relative and 1E-4 Ω was added to the data.

The inversion results in figs. 6.20 and 6.21 reflect the original model in that the isotropic background is met with good agreement for the magnitude. Yet, only the location of the layer top is correctly interpreted by the algorithm. Starting with the largest value of λ_a, the inverted sections exhibit no anisotropy of the embedded layer. In this case, the strong anisotropy penalty prohibits the successful reconstruction of the original section. On the other hand, smaller λ_a-value allows for more anisotropy, in the

location in m		magnitudes in $\log_{10} \Omega m$			phase angles in $mrad$			info
x	z	$\|\rho_x\|$	$\|\rho_y\|$	$\|\rho_z\|$	$\angle\rho_x$	$\angle\rho_y$	$\angle\rho_z$	
-	-	0	0	1	0	0	-10	model inside layer
11.25	-2.25	0.02	0.31	0.34	6.5	-6.6	-11.2	max. inside layer
0.25	-2.25	0.0	0.18	0.19	-1.9	-3.6	-6.2	min. inside layer
-	-	0	0	0	0	0	-10	model outside layer
0.25	-9.40	0.01	0.00	0.00	-14.0	-6.1	-3.9	outside dike

Table 6.4: Inverted resistivities (magnitude: $\|\rho_i\|$, phase angle $\angle\rho_i$) with anisotropy penalty $\lambda_a = 10^{-7}$ of the data recorded over the model in fig. 6.19 at selected points.

regarded case, a λ_a-value of $1E-7$ produces the visually best inversion result, despite the overestimated y magnitude. Generally, the original magnitude anisotropy is only partially recovered and the layer's extent is at the same time underestimated in lateral size and overestimated in depth (in case the bottom layer boundary is even visible at all). The phase angle sections exhibit reasonable results in terms of reconstruction only at large λ_a values, where two layers (no bottom layer boundary) can be determined. However, no significant anisotropy is recovered and, with smaller λ_a values (e.g., $1E-7$), the phase angle reconstruction becomes erratic and non-interpretable. An overview of critical model values and recovered values is presented in table 6.4.

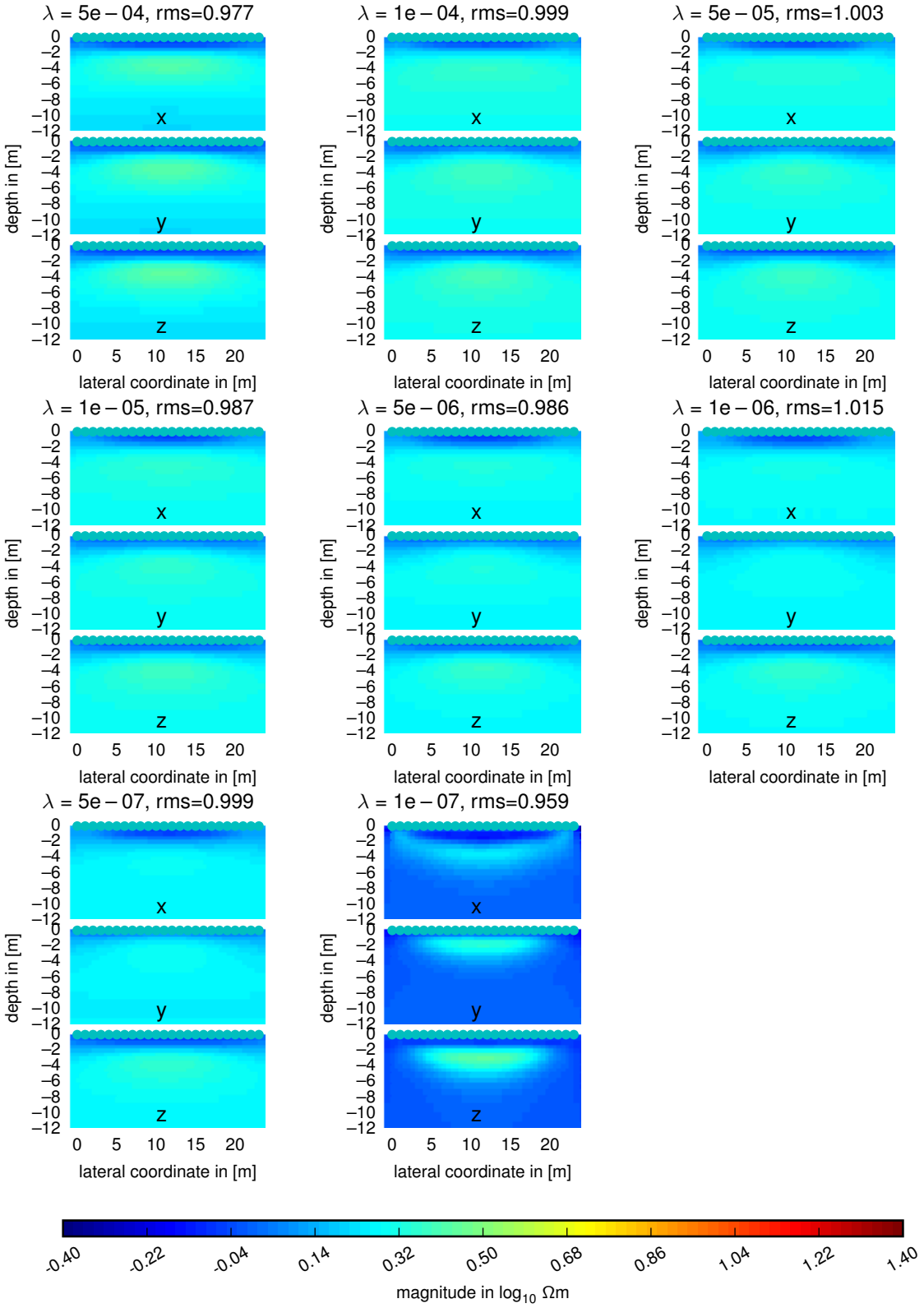

Figure 6.20: Magnitude of the inversion results of the dike model in fig. 6.19 computed with multiple anisotropy lambda values.

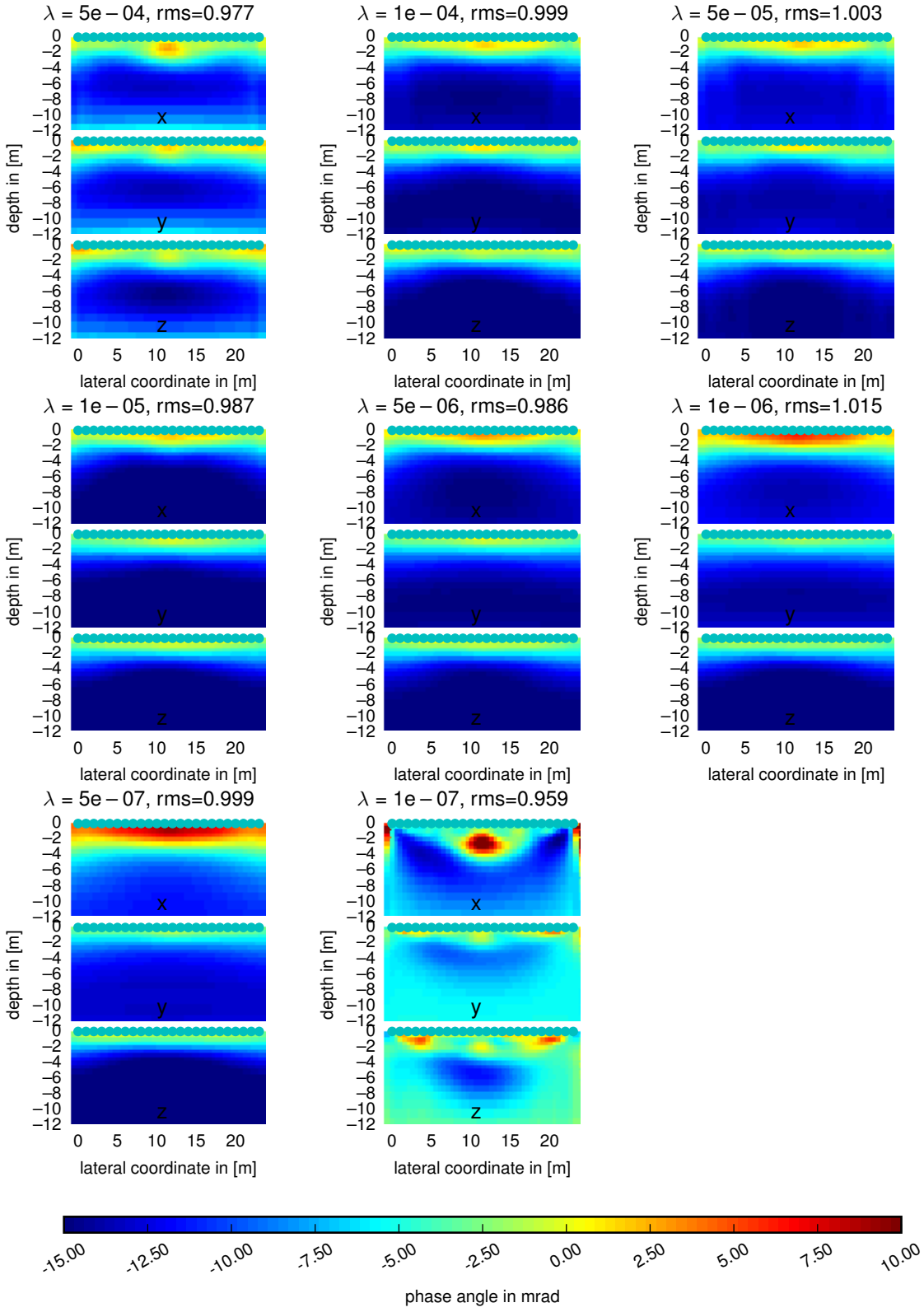

Figure 6.21: Inverted phase angle of the dike model in fig. 6.19. The assumed phase angle error is 1 mrad. For details see fig. 6.20.

6.4.2.6 Surface Electrodes Model II: Dipping Layer

In this section, another model with surface electrodes is analyzed. The original model is shown in fig. 6.22. It contains a dipping layer with anisotropic complex conductivity magnitude $(10^0, 10^0, 10^1)\Omega m$ and phase angle $(0, 0, -10)$ mrad inside an isotropic background with $10^0 \Omega m, 0$ mrad.

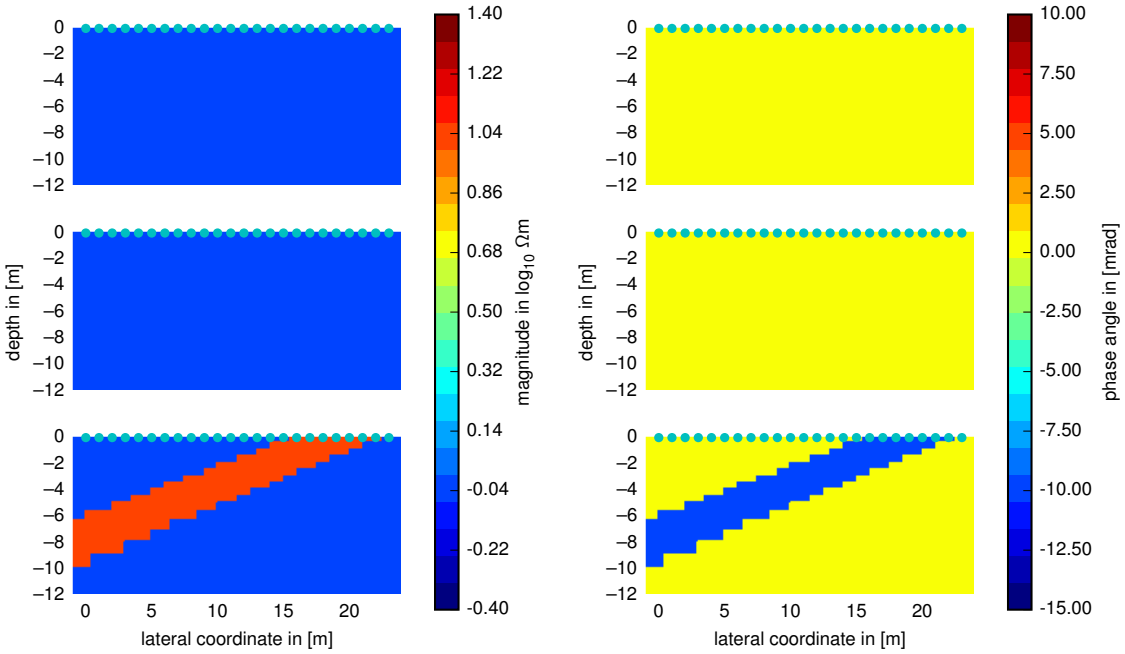

Figure 6.22: Original dipping layer model with a surface setup with 24 collinear electrodes with 1 m spacing. The synthetic measurements are carried out with all feasible dipole-dipole setups with skip-0 to skip-6 offsets. The inversion parameters were set to 1% relative and 1E-4 Ω absolute error. Gaussian noise of 1% relative and 1E-4 Ω was added to the data.

The inversion results in figs. 6.23 and 6.24 reflect the original model in a way that the isotropic background is met with good agreement for the magnitudes (similar to sec 6.4.2.5). Still, only the location of the top layer section — close to the electrodes — is correctly interpreted by the algorithm; the anomaly cannot be recovered at larger depths. Starting with the largest value of λ_a, the inverted sections again exhibit strongly

location in m		magnitudes in $\log_{10} \Omega m$			phase angles in $mrad$			info
x	z	$\|\rho_x\|$	$\|\rho_y\|$	$\|\rho_z\|$	$\angle\rho_x$	$\angle\rho_y$	$\angle\rho_z$	
-	-	0	0	1	0	0	-10	model inside layer
14.25	-2.25	0.11	0.32	0.48	5.0	-6.6	-4.7	max. inside layer
0.25	-7.52	0.01	0.02	0.03	-10.7	-5.0	-4.9	min. inside layer
-	-	0	0	0	0	0	-10	model outside layer
22.75	-7.52	0.01	0.02	0.02	-14.7	-5.9	-3.5	outside dike

Table 6.5: Inverted resistivities (magnitude: $\|\rho_i\|$, phase angle $\angle\rho_i$) with anisotropy penalty $\lambda_a = 10^{-7}$ of the data recorded over the model in fig. 6.22 at selected points.

smoothed edges of the embedded layer and no anisotropy . With smaller λ_a's, magnitude anisotropy is recovered, although the z magnitude remains underestimated, while x and y magnitude are slightly and vastly overestimated, respectively. The phase angle sections exhibit reasonable results in terms of reconstruction only at large λ_a values, where two layers (no bottom layer boundary) can be determined. The dipping of the layer can be identified at the right side of the section. Nonetheless, no significant anisotropy is recovered and, with smaller λ_a values (e.g., $1E-7$), the phase angle reconstruction becomes erratic and non-interpretable. An overview of critical values of the original and the recovered model is presented in table 6.5.

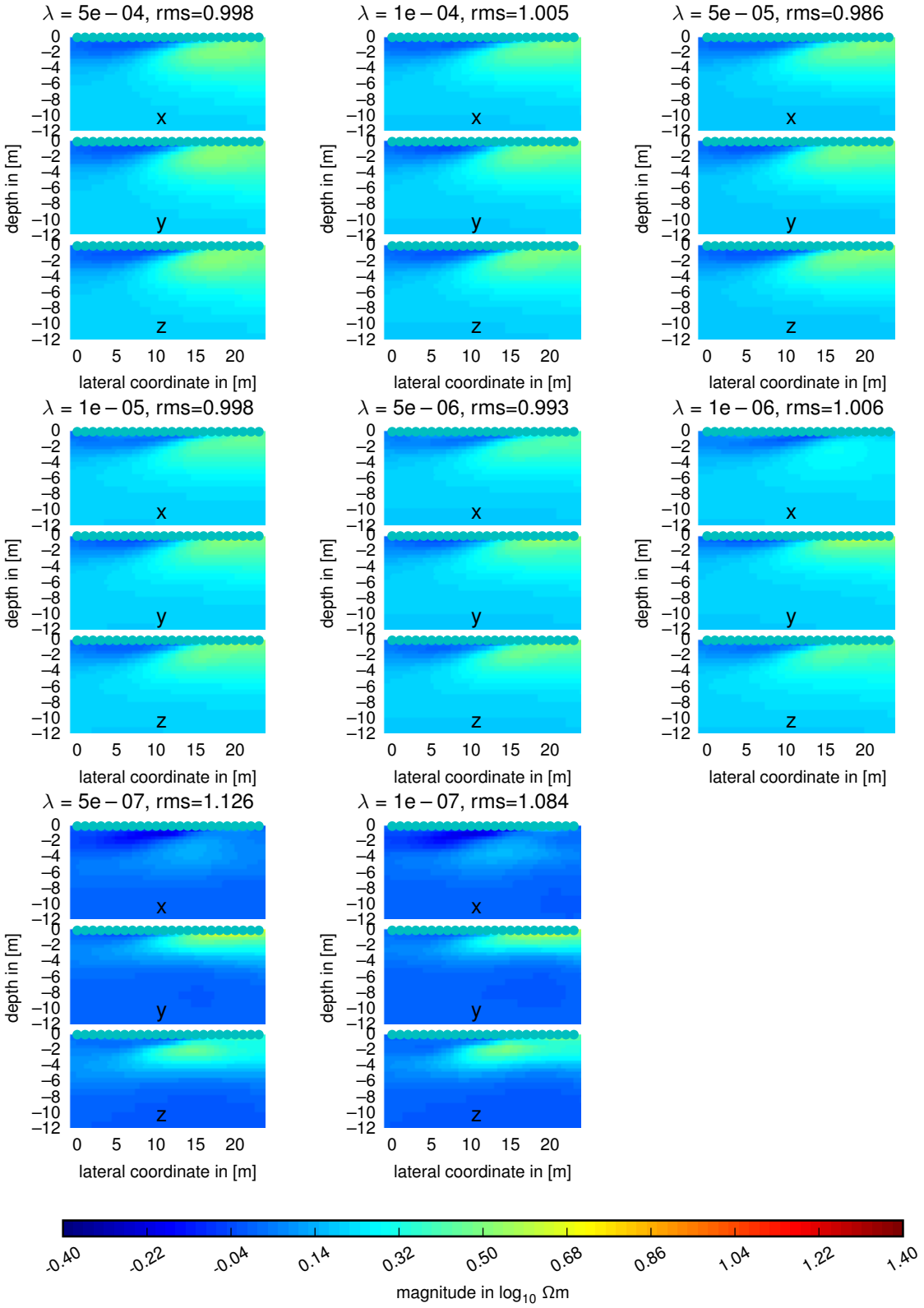

Figure 6.23: Magnitude of the inversion results of the dipping layer model in fig. 6.22 computed with multiple anisotropy lambda values.

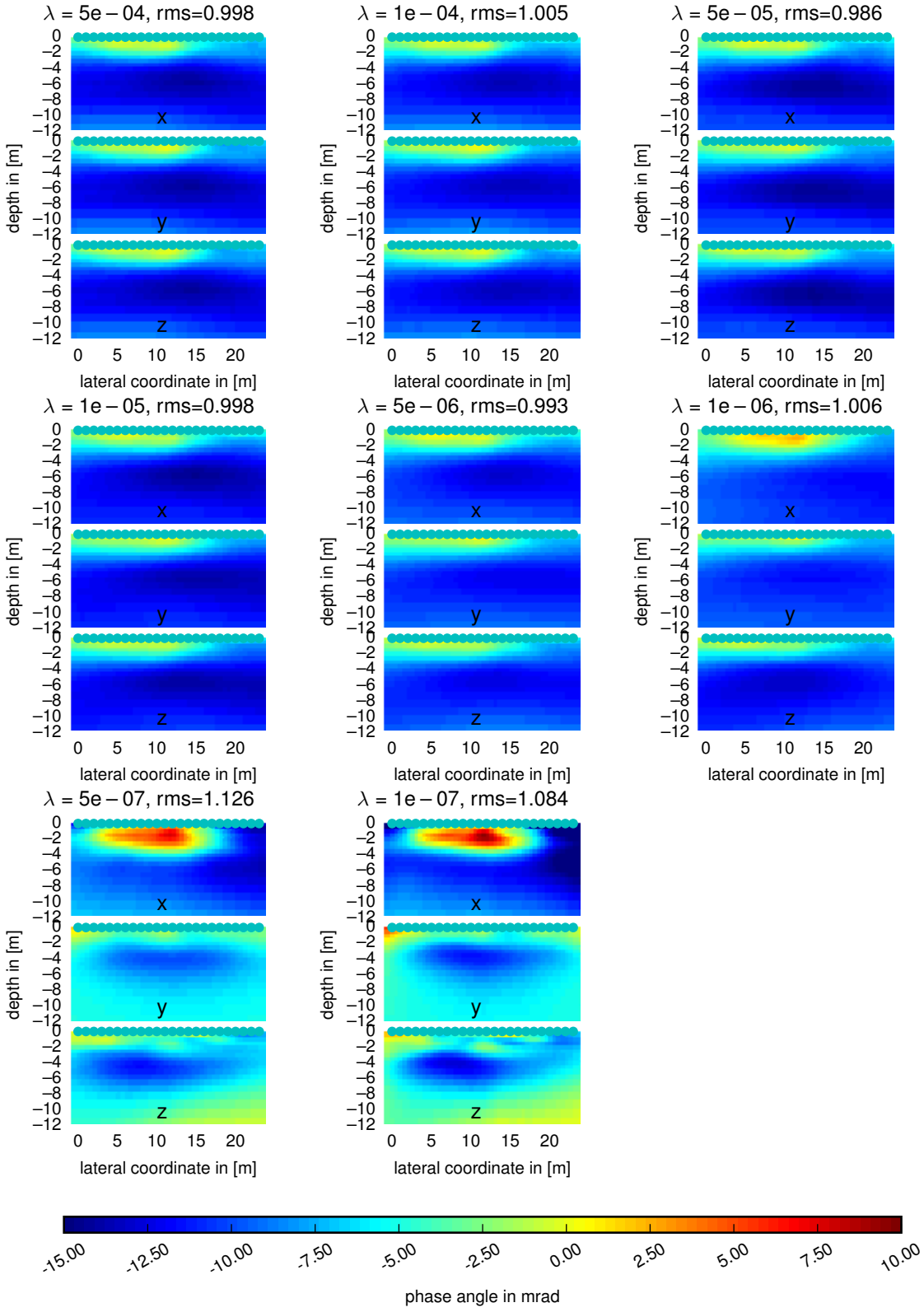

Figure 6.24: Phase angle of the inverted sections of the layer model in fig. 6.22. The assumed phase angle error is 1 mrad. For details, see fig. 6.23

6.4.2.7 Borehole Electrodes Model

In this section, a borehole model with one vertical borehole is considered. The model is depicted in fig. 6.25. The model is constituted of a horizontal layer with anisotropic

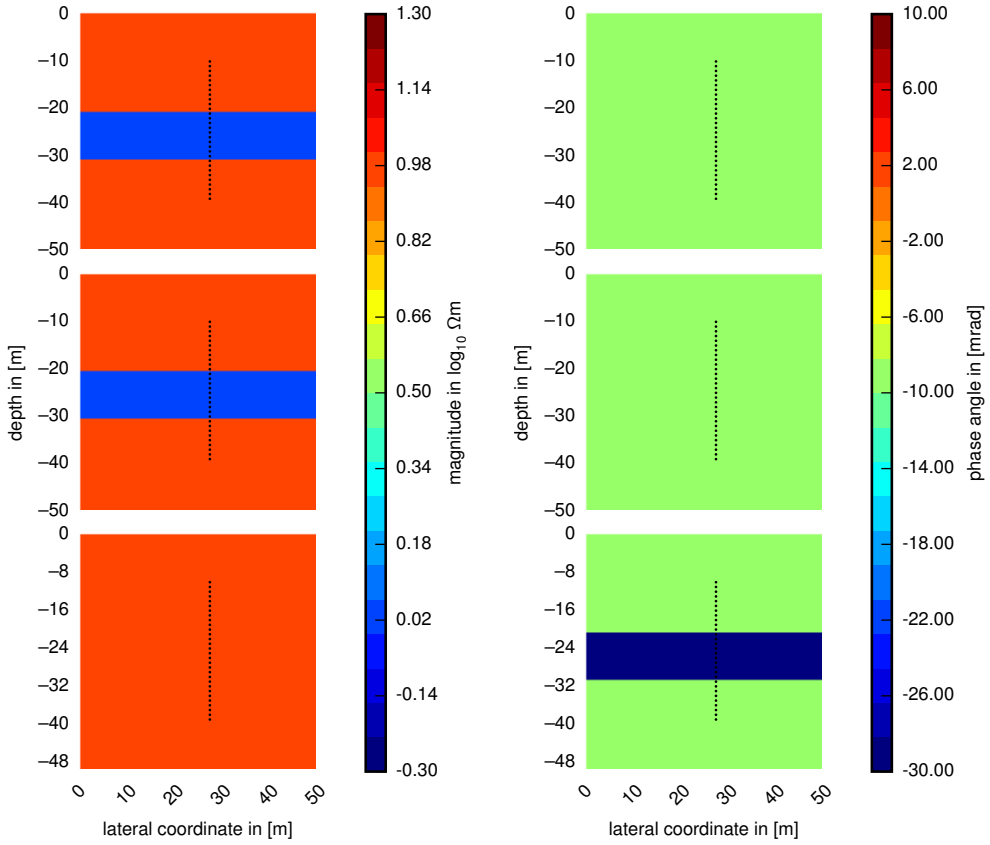

Figure 6.25: Original model of a borehole setup with 30 collinear electrodes with 1 m spacing. The synthetic measurements are carried out with all feasible dipole-dipole setups with skip-0 to skip-8 offsets. The inversion parameters were set to 1% relative and 1E-4 Ω absolute error. Gaussian noise of 1% relative and 1E-4 Ω was added to the data.

resistivity embedded into an isotropic half-space with a resistivity of $10^1 \Omega m$ and a crossing vertical borehole with 30 equidistant electrodes. The model is chosen in such a way that the resistivity is lowered by a factor of 10 in x and y direction ($10^0 \Omega m$). The phase angle is set to isotropic -10 mrad at the background and to $(-10, -10, -20)$ mrad inside the layer.

The inversion results in figs. 6.26 and 6.27 reflect the original model in that the isotropic background and the location of the layer is met with good agreement in the vicinity of the electrodes. Starting with the largest value of λ_a, the inverted sections exhibit no anisotropy. In this case, the strong anisotropy penalty prohibits the successful reconstruction of the original section. On the other hand, a smaller λ_a-value allows for more anisotropy. In the regarded case, a λ_a-value of $1E-7$ produces the most accurate inversion result.

According to the above table, the resistivities in the different directions are recon-

location in m		magnitudes in $\log_{10}\Omega m$			phase angles in $mrad$			info
x	z	$\|\rho_x\|$	$\|\rho_y\|$	$\|\rho_z\|$	$\angle\rho_x$	$\angle\rho_y$	$\angle\rho_z$	
-	-	0	0	1	-10	-10	-20	model inside dike
25.25	-25.75	0.00	0.01	1.01	-23.5	2.3	-37.3	max. inside dike
0.25	-25.75	0.58	0.61	0.84	-16.4	-13.8	-18.7	min. inside dike
-	-	1	1	1	-10	-10	-10	model outside dike
0.25	-47.75	1.77	1.77	1.77	-8.4	-7.5	-7.5	outside dike

Table 6.6: Inverted resistivities (magnitude: $\|\rho_i\|$, phase angle $\angle\rho_i$) with anisotropy penalty $\lambda_a = 10^{-7}$ of the data recorded over the model in fig. 6.25 at selected points.

structed in the vicinity of the electrodes. Obviously, at larger distances from the electrodes, the layer fades into the background due to decreasing sensitivity magnitudes. The phase angle sections reconstruct the background values. However, strong artifacts appear in the x phase angle section, which also overestimates the original phase angles. Also, the z phase angle section strongly overestimates the original model and again exhibits strong artifacts. As an outlier, the y phase angle section displays only small artifacts and represents the original model best (visibly, the original model in this case is homogeneous).

To sum up, the magnitudes in this model can be recovered adequately, although the layer fades at greater distances from the electrodes — this behavior can also be observed with isotropic inversion algorithms and is due to the nature of both the sensitivity patterns and the application of a smoothness-constraint penalty function (see e.g., Kemna (2000)). However, the phase angle sections only insufficiently recover the original sections. A substantial problem to these sections is the existence of strong artifacts.

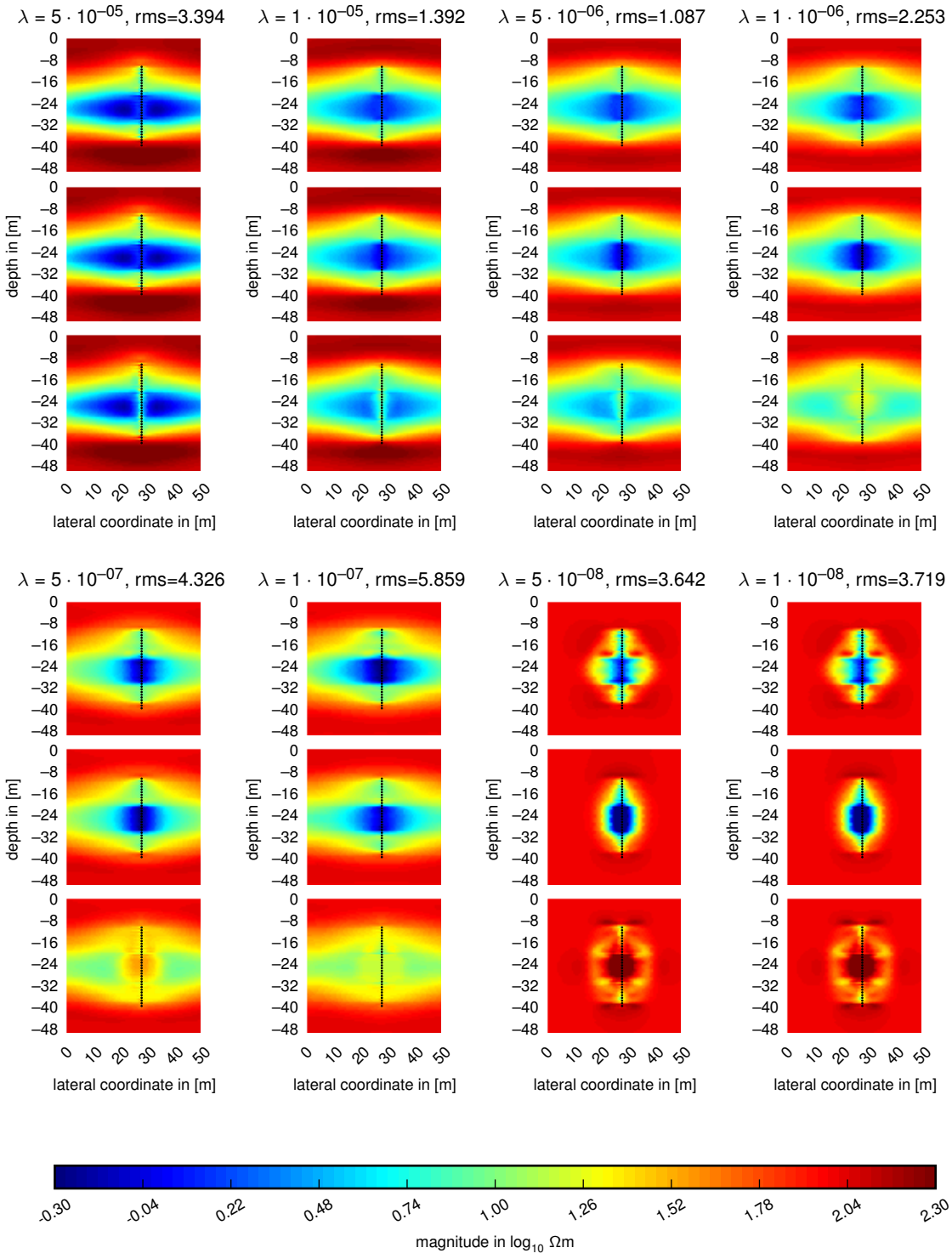

Figure 6.26: Magnitude inversion results of the borehole model in fig. 6.25 computed with multiple anisotropy lambda values.

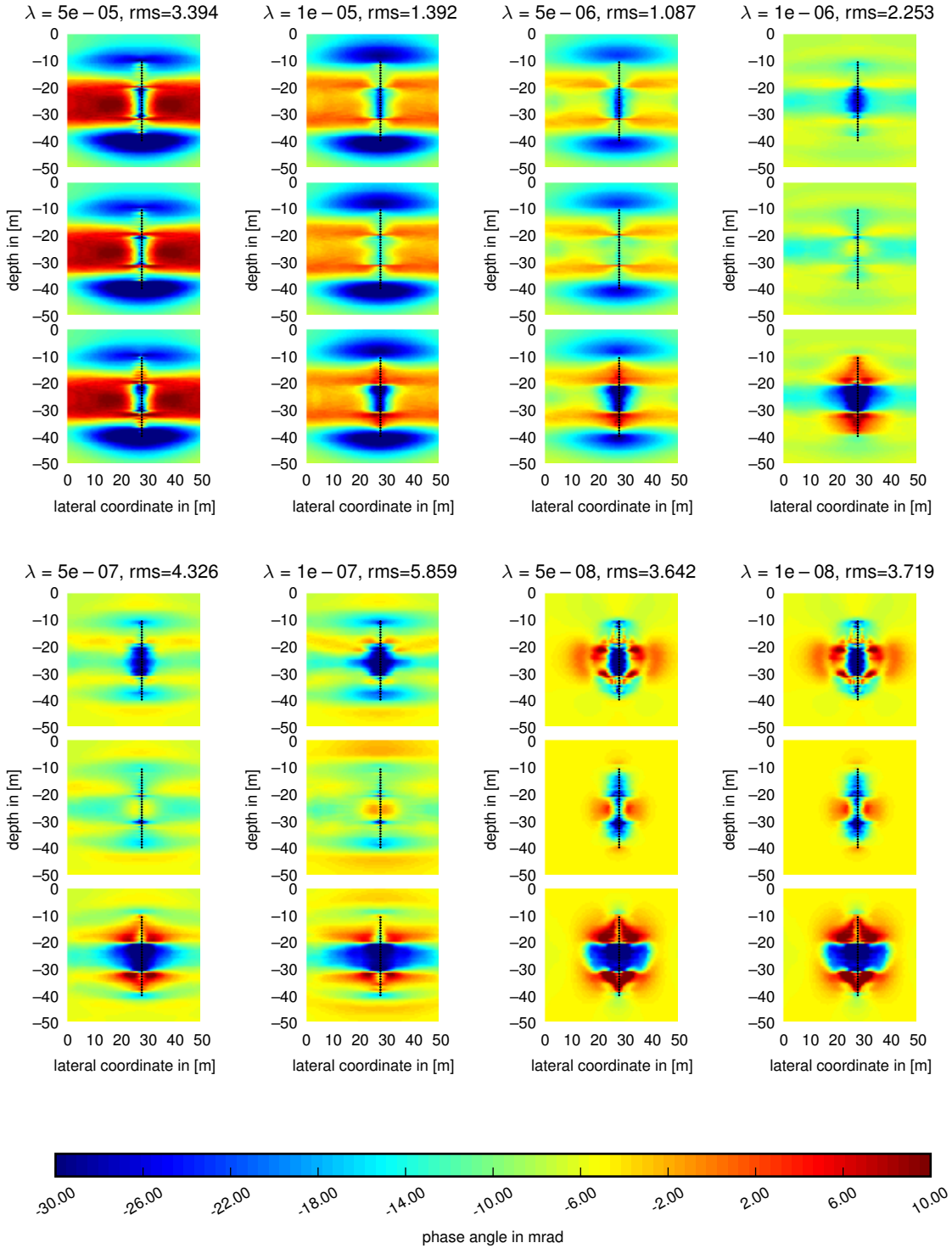

Figure 6.27: Phase angle inversion results of the borehole model in fig. 6.25 computed with multiple anisotropy lambda values.

7

Demonstration on Field Data: Rollesbroich Test Site

7.1 Field Setup

A surface data set was recorded at the Transregio TR32 Rollesbroich test site with a surface setup of 49 electrodes consisting of dipole-dipole skip-0 measurements. The data was recorded with the Radic Research SIP-256C (Radic Research, 2016) device with frequencies covering 4 decades in a range from $39\ \mathrm{mHz}$ to $1000\ \mathrm{Hz}$. Figure 7.1 shows the filtered raw data; here, outliers and defective electrodes were removed. The apparent resistivity magnitude in the left panel exhibit a low-resistive (less than $10^2.7\Omega m$) surface layer with varying thickness above a more resistive and smooth deeper subsurface. The apparent resistivity phase angle* displays a smoother section. Moreover, an area with higher phase angles is visible between pseudo depths of $15\ \mathrm{m}$ to $35\ \mathrm{m}$ and from $55\ \mathrm{m}$ on the lateral coordinate. It may be noted that the apparent resistivity magnitude pseudo section contains many diagonal lines with constantly higher or lower values that are not present in the phase angle pseudo section. However, since the computation of the apparent resistivity implies the configuration factor k (see section 2.2), these "faulty" electrode data may be originated only in slightly misplaced electrodes in the order of centimeters or some coarse ground structures at the surface, which would result in a non-uniform current flow from this electrode.

*Which is identical to the measured phase angle at a given point in the pseudo section.

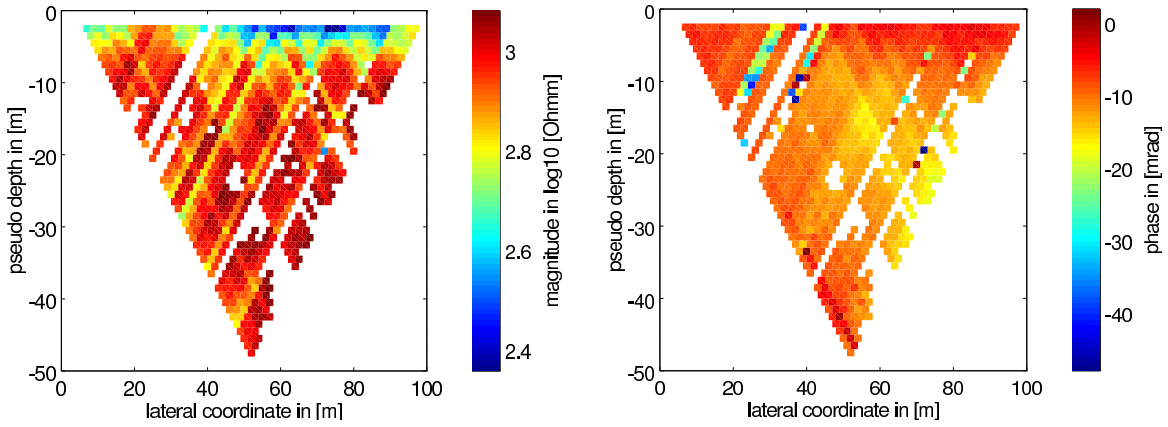

Figure 7.1: Pseudo sections of magnitude and phase angle of the apparent resistivity recorded at the Rollesbroich test site with 49 electrodes and a measurement frequency of 0.625 Hz. In this data set, only dipole-dipole setups with skip-0 were used.

7.2 Inversion Results

The plots in fig. 7.2 and fig. 7.3 exhibit the resistivity magnitude and phase angle of the inverted data that was recorded at the Rollesbroich test site computed with different anisotropy penalties ranging over 3 decades. The magnitudes of the inversions sections in fig. 7.2 are mostly isotropic and reveal a system of two layers with a thin first layer with around $10^{2.0}\ \Omega\mathrm{m}$ and varying thickness from $0.3\ \mathrm{m} - 0.6\ \mathrm{m}$ over a more resistive second layer with resistivities up to $10^{2.5}\ \Omega\mathrm{m}$. At $(\text{lateral } 3.3\ \mathrm{m}, \text{vertical } -0.6\ \mathrm{m})$, $(8\ \mathrm{m}, -0.4\ \mathrm{m})$ and $(10\ \mathrm{m}, -0.4\ \mathrm{m})$, low-resistive structures appear in the more resistive second layer. These structures can either be interpreted as small dike-like structures or as a result of locally poor data quality. Anisotropy is only resolved for the two smallest anisotropy penalty inversions. In the case of $\lambda_a = 1e-6$, the resistivity magnitude in z direction is significantly increased to up to $10^{2.50}\ \Omega\mathrm{m}$, while it is decreased in x direction to as low as $10^{2.47}\ \Omega\mathrm{m}$, resulting in a magnitude ratio of $\frac{\rho_x}{\rho_z} = 0.99$. The sections corresponding to the anisotropy penalty $\lambda_a = 1e-7$ exhibit larger anisotropy. However, they are not considered here because the inversion does not finish with a satisfying RMS value of around 1.0.

The phase angle sections in fig. 7.3 present phase angle values in the range of $-30\ \mathrm{mrad}$ to $> 0\ \mathrm{mrad}$. Generally, a two-layer subsurface can be identified in the sections, where the first layer has a larger thickness in the range of $0.6\ \mathrm{m}$ - $1.3\ \mathrm{m}$ when compared to the magnitude sections. It is noteworthy that the anomalous low-resistivity magnitude areas are not prominent in the phase angle sections. Anisotropy is only resolved for anisotropy penalties of $1e-6$ and smaller. In the inversion with $\lambda_a = 1e-6$, the phase angles in the first and second layer are around $-3\ \mathrm{mrad}$ and $-15\ \mathrm{mrad}$, respectively.

In figures 7.4 and 7.5, anisotropic inversions are carried out for all recorded frequencies in a range of 0.04 Hz - 1000 Hz at a fixed anisotropy penalty of $\lambda_a = 1e-6$. In the case of the magnitude sections in fig. 7.4, both a small decrease of resistivity magnitude with larger frequencies and small anisotropy can be found. More prominent, the phase angle sections exhibit anisotropy throughout all shown inverted sections. Also, their

frequency-dependence is strong with generally lower phase angles at higher frequencies (which is usually described as ”EM coupling” effect, see e.g., Bhattacharya & Srivastava (2016)).

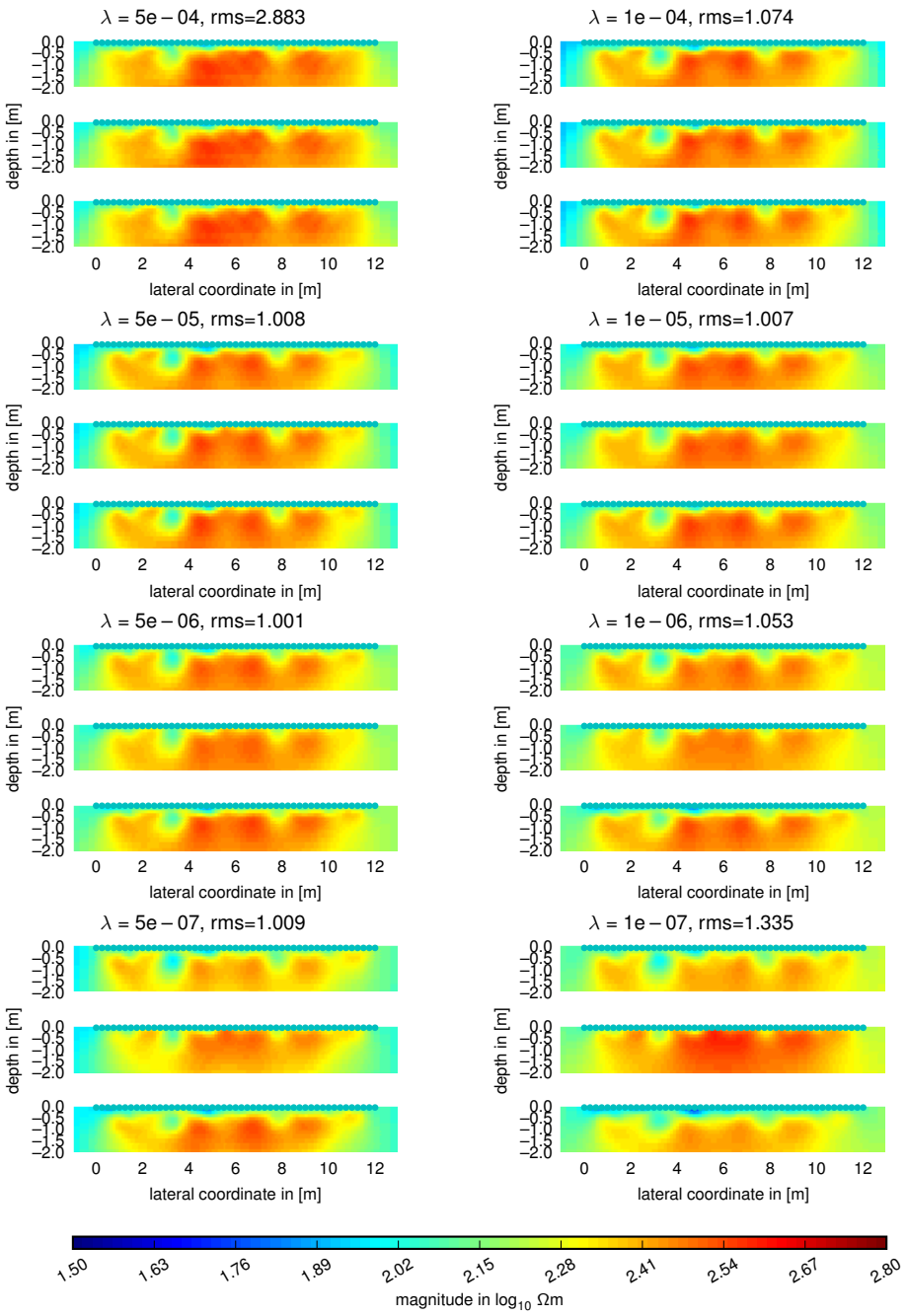

Figure 7.2: Resistivity magnitude of anisotropic inversion results of the raw data in fig. 7.1 (frequency 0.625 Hz) for different anisotropy penalties in the range of $\lambda_a = 5e-4$ to $\lambda_a = 1e-7$. Turquoise dots denote the 49 electrodes. The depicted results represent the 2nd inversion iteration. For the inversion, the assumed data errors were set to 1% relative plus $1e-3\ \Omega$ absolute resistance magnitude error and 1 mrad phase angle error. The starting model was set to homogeneous and isotropic $(100\ \Omega m, -10$ mrad$)$.

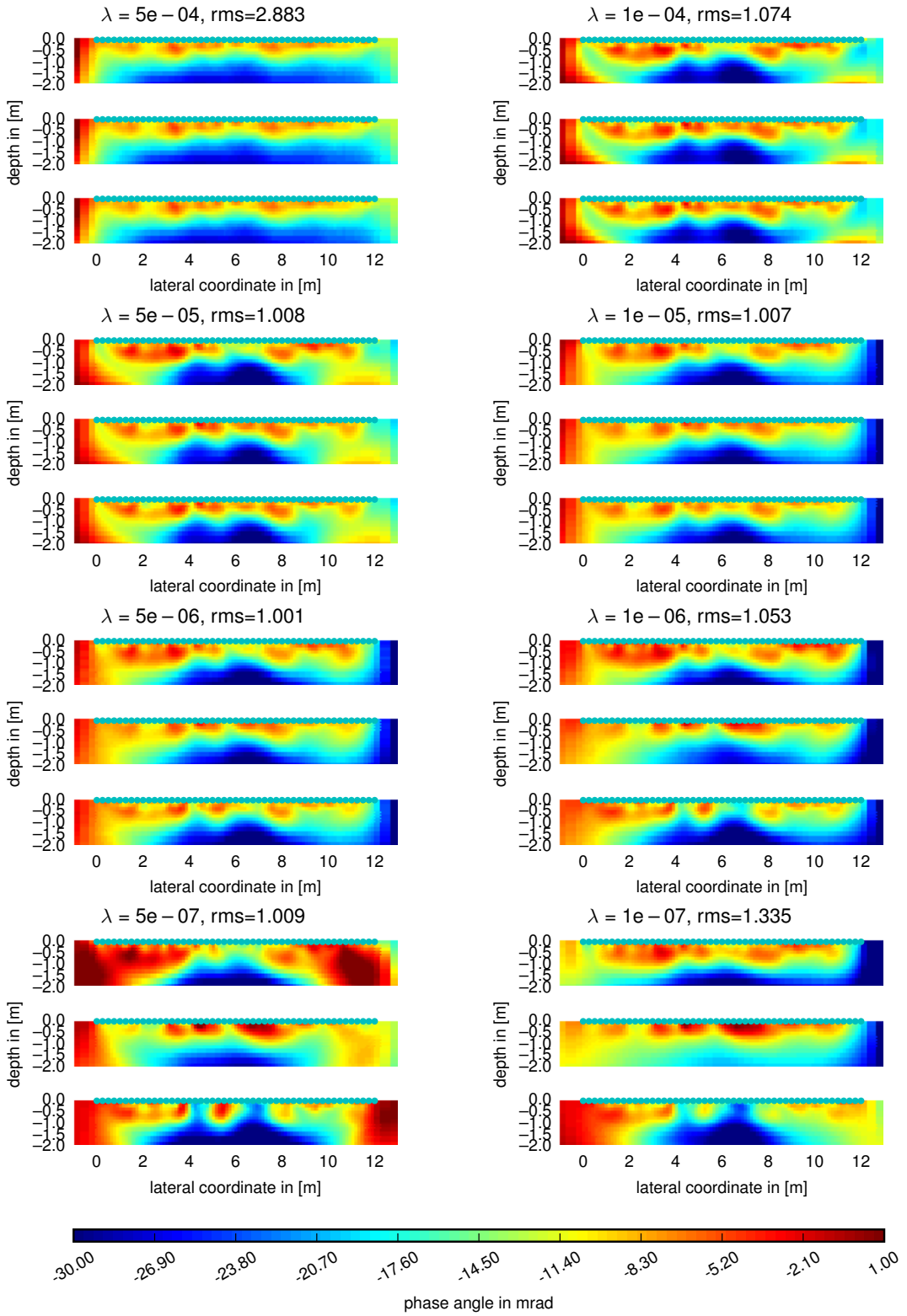

Figure 7.3: Anisotropic resistivity phase angle inversion results of the raw data in fig. 7.1. For details, see fig. 7.2.

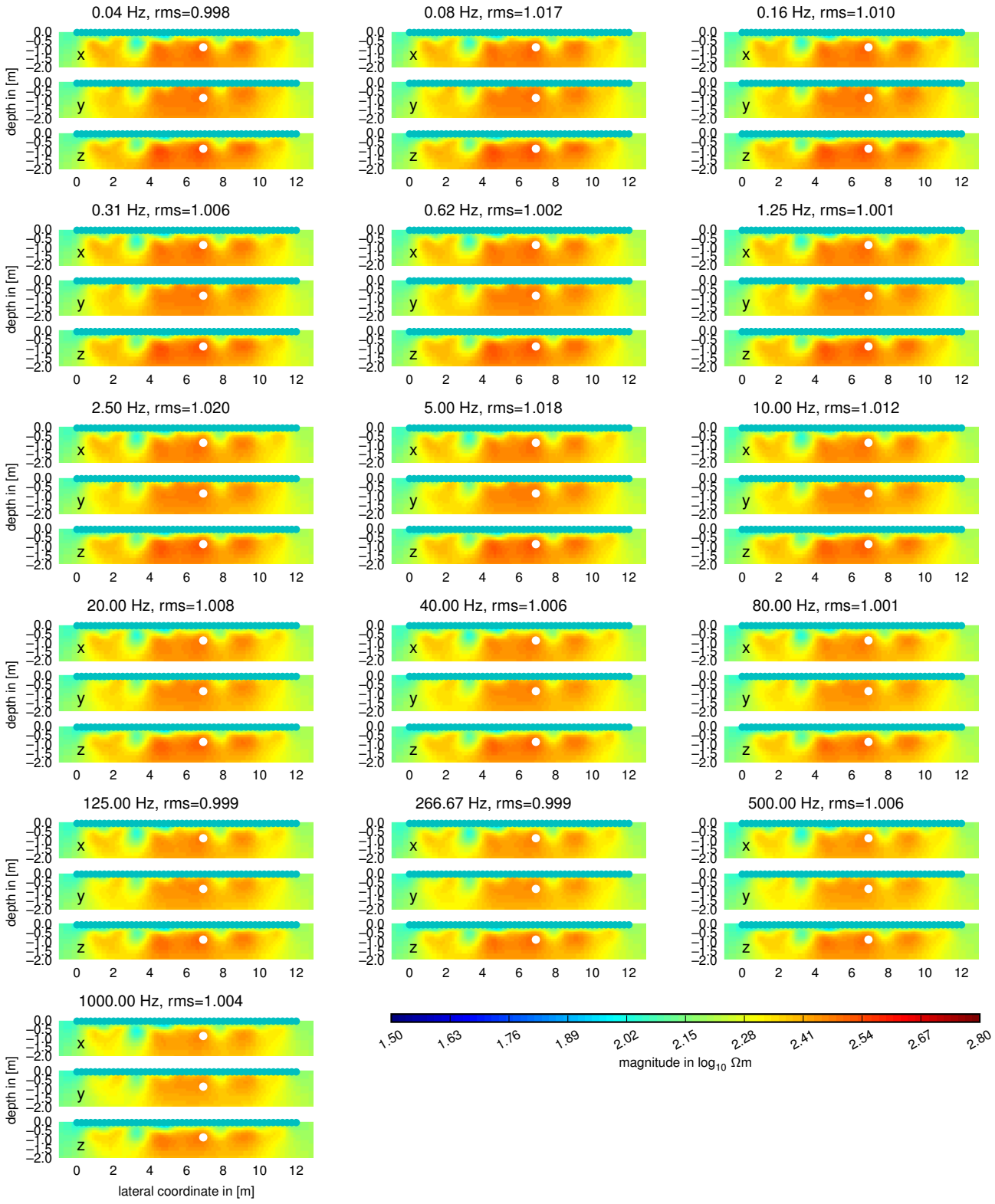

Figure 7.4: Resistivity magnitude of anisotropic inversion results of the raw data in fig. 7.1 for 15 (approximately logarithmic-equally spaced) frequencies in the range of 0.04 Hz to 1000 Hz and a fixed anisotropy penalty $\lambda_a = 1e-6$. The turquoise dots denote the 49 electrodes. The depicted results represent the second inversion iteration for better comparability. The general inversion parameters were 1% relative plus $1e-3\ \Omega$ absolute resistance magnitude error and 1 mrad phase angle error. The starting model was set to homogeneous and isotropic $(100\ \Omega\mathrm{m}, -10\ \mathrm{mrad})$. The white dots represent the location of the collected soil sample (see 7.3) at $x = 6.91$ m and $z = -0.91$ m.

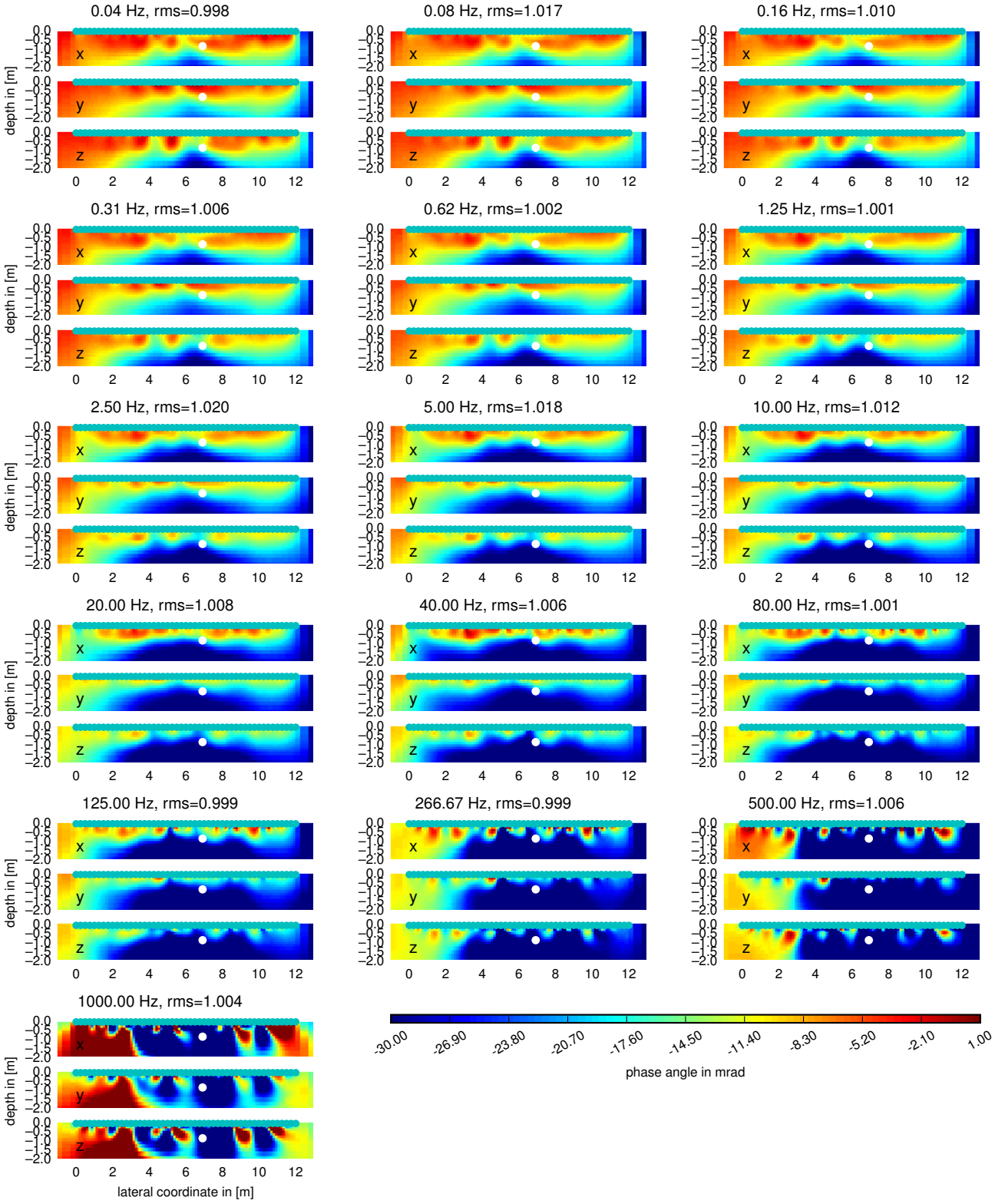

Figure 7.5: Resistivity phase angle of anisotropic inversion results of the raw data in fig. 7.1. For details, see fig. 7.4.

7.3 Comparison with In-Situ Soil Samples

To investigate the quality of the inverted sections, material samples were collected on site. The samples were examined regarding their electrical resistivity and polarization properties, i.e., their resistivity magnitude and phase angle. The samples were collected *in-situ* on site to allow for measuring the anisotropic resistivity in horizontal and vertical direction (only two sample containers were available) at the collection points. Figure 7.6 shows the sample container at the test site, where the first sample was collected in vertical (z) direction through pressing the empty container in the ground. Once pulled out, material sticks inside the container. Later, the resistivity in the direction of the sample container is measured in the laboratory. The second sample was taken in horizontal (x) direction and processed in the same fashion.

At the point of the in-situ measurement, the inversion result can be analyzed for each frequency and plotted side by side with the in-situ data (fig. 7.7). The resistivity magnitudes at the top panel of fig. 7.7 are decreasing with larger frequencies. For both methods (EIT and in-situ measurement), the vertical resistivity is larger than the horizontal resistivity, i.e., $\rho_x/\rho_z < 1$. Also, the comparison of actual recovered conductivity anisotropy ratios yield similar values for both methods. The phase angle in the lower panel of fig. 7.7 shows a ratio of $\varphi_x/\varphi_z > 1$ for the recovered EIT model, while the in situ phase angles show opposite results. However, since the overall differences in phase angles are of the order of $1\mathrm{mrad}$ for frequencies less than $1kHz$, they may be originated in noisy data or erroneous modelling[†].

In summary, the magnitudes of the inverted resistivities are in good agreement with the in-situ measurements in terms of anisotropy ratio and frequency dependence. However, the absolute values of both horizontal and vertical resistivities are significantly different for the measured and recovered models. One possible explanation might be the spatial smoothing in the inversion process, which would flatten out a possible small-scale variation in the real resistivities. On the other hand, the phase angles are not in agreement regarding the anisotropy. Despite this, the depicted phase angles are all very similar (and therefore in a reasonable agreement). Since the regarded phase angles are generally a sensitive quantity, one possible explanation could be a distortion of the sample, e.g., density or texture of the soil sample.

[†]As previously mentioned (3.4.1), the accuracy of the modelling algorithm is in that same magnitude.

Figure 7.6: Sample collection at the Rollesbroich test site. The sample container (white circle) is pressed into the ground and later extracted together with the soil sample.

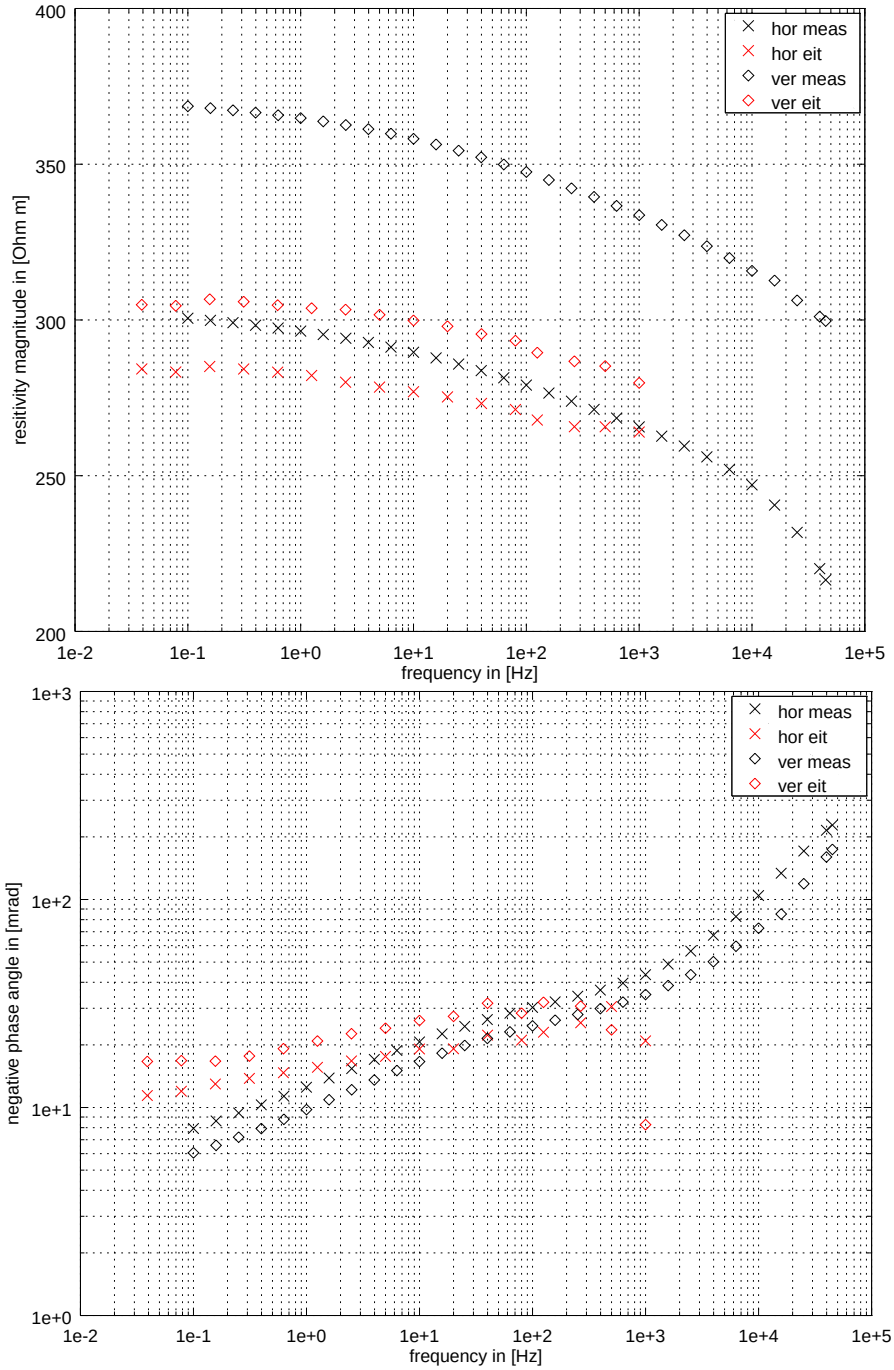

Figure 7.7: Comparison of inverted (red) versus in situ (black) resistivities for horizontal ($\times$) and vertical ($\diamond$) resistivity. Top: resistivity magnitude. Bottom: negative resistivity phase angle

8

Performance

The introduction of anisotropy in the inversion algorithm is represented by a higher use of memory and CPU time. Generally, the required time for a complete inversion is composed of the individual computation times for the modeling steps: the finite element modeling time is approximately quadratic with respect to the number of model cells, i.e., $t_{\text{modeling}} \propto n_{\text{cells}}^2$, see fig. 8.1*.

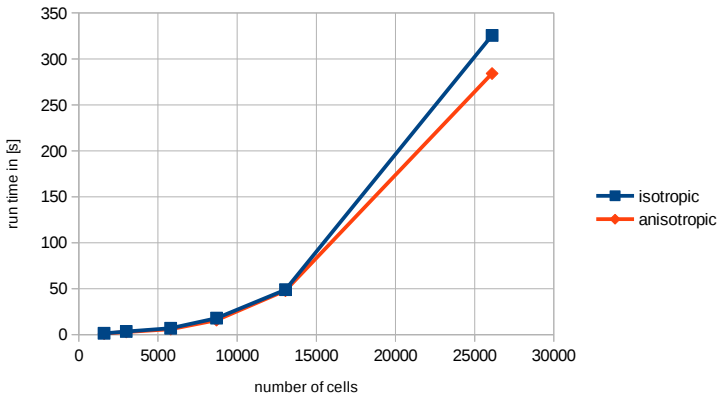

Figure 8.1: Run time versus numbers of cells with the isotropic (blue) and the anisotropic (red) conductivity modeling algorithm.

In 2.5-D mode, `CRMod` utilizes wave-number sampling points to characterize the third dimension. This enables the code to model point source potentials over a 3-D space with the restriction of non-varying conductivities in one direction. For each wave-number k, a system of linear equations is solved. This process is capsuled, because the calculations do not rely on each other. This parallelization potential is used for the following example: basically, the solution of the linear systems for each wave-number is calculated in parallel. The parallelization is done with `OpenMP` for each wave-number. The maximum expected speedup linearly corresponds to the number of wave-numbers or number of CPUs used, whichever might be the smaller number.

Figure 8.2 shows the speedup on multi-core computers for a small grid with 2200 elements and 6 wave-numbers. The results imply a reasonable speedup already with

*The anisotropic modeling code is faster in this case. However, this result could be due to varying CPU workload on this shared user machine.

two processors. The maximum speedup is 1.4. Nonetheless, most of the code is not yet prepared for parallel execution, so the impact is far less then the expected linear factor of 1, especially with increasing number of CPUs.

Figure 8.3 shows the speedup for a large grid with 48000 elements and 15 wave-numbers. In this case, a performance gain exists until the number of CPUs is larger than the number of wave-numbers. The maximum performance gain on a 2 core computer is 2 and 13 on a 32 core computer (corresponding to a linear factor of 0.87). C.2

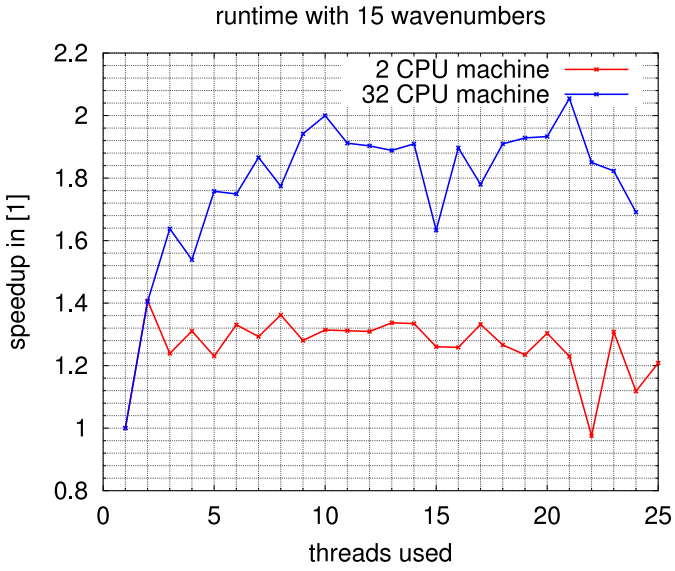

Figure 8.2: Speedup with small grid and 6 wave-numbers.

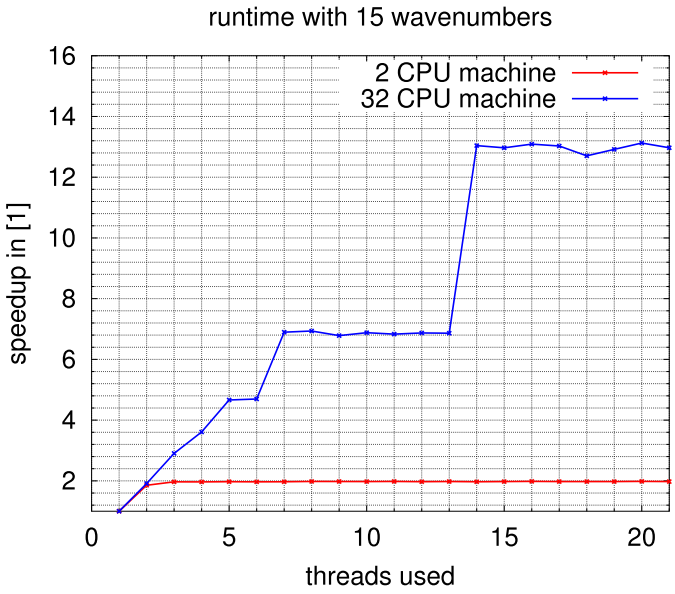

Figure 8.3: Speedup with large grid and 6 wave-numbers.

9

Discussion and Interpretation

The results of the measurement response study reveal individual and distinct patterns for a ”buried” anisotropic anomaly. In the regarded case of measuring with surface electrodes, the x, y and z-anisotropy anomalies can be clearly discriminated from by their response curves. In the case of the synthetic borehole roll-along measurement, the patterns of the situation with current and potential electrodes each in pairs in the boreholes again lead to distinct patterns, whereas the situation in which one current and one potential electrode is placed in one borehole each results in far more similar curves. The shape of the displayed curves can be related to the corresponding sensitivity patterns, which in turn provide them to the inversion algorithm. Therefore, due to the measured data not being identical in shape and strength, it can be stated that the synthetic data holds information regarding the individual conductivity directions even if it is not sufficient for the perfect reconstruction through a potential inversion algorithm.

However, since the ability to resolve anisotropy obviously relies on small differences in recorded data, corresponding noise will be an issue. Regarding the measurement response curves again, this becomes apparent for similar response shapes (like the y and z responses in fig. 6.2), where noise could equal out the differences in the patterns (and in strengths, but to a lesser extent).

Considering individual responses to solely anisotropic magnitude or phase angle anomalies, the results indicate very similar — and similarly distinct — patterns. Despite this, the pattern strengths are generally stronger for magnitudes anomalies when compared to phase angle anomalies. Taking into account that phase angles are generally much more prone to noise (cf. Kemna (2000), chapter ”Numerical Solution”), noise in measured data is even more critical for the reconstruction of phase angles of anisotropic complex conductivities.

As previously presented in Kenkel *et al.* (2012), the attempt of reconstructing anisotropic models with an isotropic inversion algorithm is prone to failure (e.g. the anisotropic model in fig. 6.11 results in the inverted section in fig. 6.7).

The inversions of the model with an (almost) complete surrounding of electrodes (see the model in fig. 6.11) can be tuned for a good model recovery by the standard means of suggested data quality and reached data misfit. In fact, most of the inversions are able to reconstruct the location of the regarded dike structure. When considering the anisotropy control parameter λ — which may also be understood as a connection strength parameter between the individual complex conductivities — the inversion results differ in an explicable manner. First, if the coupling parameter λ is large, very little

anisotropy is allowed, i.e., the anisotropy cost/penalty Ψ_a (see e.g. 5.4.1) is dominant when compared to the model roughness Ψ_m (see Section 5.2, eq. 5.8), resulting in a more isotropic model. A secondary effect here is the comparatively bad reconstruction in conjunction with a large model-data misfit. Altogether, the example with a large λ parameter might be characterized as poor inversion result. Since the model is made up with strong anisotropy, a weaker coupling (smaller λ) should allow for more reasonable results. Indeed, the data-model misfit value drops along with a decreasing λ. The inversion results also visually improve with smaller λ's; the visually best-looking model is reached at a quite small λ value. There, the conductivity magnitudes are accurately reconstructed in x and z direction, while the y conductivity is blurred/averaged between the x and z conductivities. This behavior could be explained by the sensitivities, which exhibit their least values (for both real and imaginary conductivity) in y direction for almost all presented patterns (e.g. fig. 4.1). Thus, least reconstruction information is available to the inversion algorithm from the y conductivity and the reconstruction of this conductivity direction is dominated by the other two (x and z) conductivities. Furthermore, the above descriptions hold for the inverted phase angle sections, where a decent reconstruction is gained for similarly small λ values. It seems interesting that the general reconstruction quality can be better for phase angles when compared to magnitudes. This statement especially holds for the anomaly boundaries, which are much more precise. These sharper edges, however, seem to come at the cost of artifacts (see the bottom right panes in fig. 6.13).

Another expected behavior is confirmed, where only taking into account a subset of the measured data in the first example returns much worse inversion results in terms of reconstruction quality. For instance, the surface-only dipole-dipole subset in fig. 6.4.2.4 is only able to catch the dike anomaly very close to the electrodes and dismisses deeper structures.

Non-working examples can also be found in the synthetic study. In the case of a pure surface setup (like in section 6.4.2.5) in conjunction with a target like a horizontal layer, the inversion is unable to fully recover the original anisotropy, especially phase angle anisotropy, although the target model-data misfit is always reached. The latter point shows that the data does not contain significant information about phase angle anisotropy of the complex conductivity. This becomes apparent in the phase angle sections of the inversion, where, in the process of reducing λ, the sections remain similar until a sudden development of unreasonable artifacts. In summary, measured data needs to contain enough information about anisotropy for a reasonable recovery and this restriction is valid especially for surface-only electrode setups and for phase angle anisotropy.

Clearly, a weak point of the anisotropic inversion is the added ambiguity due to thrice as many conductivities (x, y and z versus isotropic conductivities). In the current state of the algorithm, this ambiguity has to be addressed manually by choosing the anisotropy penalty parameter λ. However, anisotropy also allows for more consistent inversions for instance in situations with layering. Here, a "block" of layers can be described with one anisotropic conductivity, whereas in the isotropic case, each layer needs to be identified individually, which would conflict with the objective of a smooth model. Consequently, an anisotropic description of the subsurface allows for a smoother model, i.e., a more favorable model in terms of model smoothness.

10

Conclusions and Outlook

The objective of this thesis is the implementation and presentation of an *inversion algorithm* for the reconstruction of *anisotropic complex conductivity* sections from measured or synthetic induced polarization data. The objectives include the application of a *modeling algorithm* for anisotropic complex conductivities as well as the derivation of *sensitivities* with respect to anisotropic complex conductivities. In the process, the gained sensitivity expressions are validated against analytical expressions, which were taken and extended from external sources. An additional validation is carried out with the sum of anisotropic sensitivities, which, in the case of an isotropic model, needs to be equal to the corresponding isotropic sensitivities. A variety of *sensitivity patterns* are presented for typical measurement setups including surface and borehole configurations. These patterns can be used to assess optimal measurement setups for a desired target location and anisotropy. Special computations are carried out for *sensitivities with respect to anisotropy ratio*, where a non-vanishing sensitivity with respect to the anisotropy ratio is an indicator for the general *ability to resolve anisotropy*.

The *inversion algorithm* is, based on modeling and sensitivities, derived with support for *three anisotropy-related inversion objectives*. The first objective targets the three individual anisotropic complex conductivities in *x, y and z* direction, representing the most general situation in which no additional assumption is made for the subsurface structure. The second objective targets *vertical layering*, representing typical sedimentary layers. Both of these objectives allow for setting a coupling parameter between the x, y and z or, respectively, the horizontal and vertical conductivity. The third objective targets horizontal conductivity and the ratio of horizontal versus vertical conductivity. In this case, no explicit coupling parameter can be governed. Instead, the objective is a smooth anisotropy ratio throughout the inverted section (along with smooth horizontal conductivity). In contrast to the first two objectives, a strong anisotropy ratio in the whole inverted section is supported by the anisotropy ratio objective function.

The algorithm is validated with *synthetic models*, in which simple structures like a dike or a layer are chosen and "ground truth" is always available for a visual comparison of the final inversion results. In most of the regarded cases, the original model can be reconstructed through the algorithm, although resolution – like in isotropic inversions – depends on the distance to the electrodes. Besides this, the anisotropy coupling parameter can be adjusted in most cases to represent the original model in terms of anomaly location and strength.

As a field demonstration, measured IP data from the Rollesbroich test site is analyzed

and inverted with the presented algorithm. In order to do so, the data is picked from one frequency and inverted for different anisotropy penalties, from which one is chosen for the application to all frequency data. As an attempt to find ground truth, soil samples were collected from beneath the electrodes. These samples allowed to measure the complex electrical conductivity in two directions in the lab. Finally, the inverted and in-situ results are compared, yielding firstly that no strong anisotropy is present and, secondly, inversion and in-situ predict contrary anisotropy values. Despite this, the accordance of inverted and in-situ interpretations is good.

In order to improve the quality and quantity of anisotropic IP inversions, a sort of automatic determination of an *optimal anisotropy penalty value* is crucial. With this, the anisotropic inversion could be applied to any normal IP measurement, regardless whether there actually is anisotropy present. With this optimal anisotropy penalty, the algorithm could be applied to historical data sets of any type to check for possible overlooked anisotropy-related features - which ought to occur very frequently in a variety of measurement settings.

11

Acknowledgement

I like to thank my colleagues for long and illuminating discussions during my work at the Steinmann Institute in Bonn. Special thanks to Christina Witte for proof-reading the whole manuscript.

The presented work with the title ”2-D Anisotropic Inversion of Frequency-Domain Induced Polarization Data” was funded by the SFB/TR32 ”Patterns in Soil-Vegetation-Atmosphere-Systems: Monitoring, Modelling and Data Assimilation”, funded by the German Science Foundation (DFG).

A

Fourier Transform of the Poisson Equation

In this appendix, the individual terms of the Poisson equation (eq. 2.28) will be successively transformed to the Fourier space. The result is a 2D Helmholtz equation. The first term yields

$$\begin{aligned}\int_0^\infty (\partial_x \sigma_x)(\partial_x \phi(y)) \cos(ky) dy &= \partial_x \sigma_x \partial_x \int_0^\infty \phi(y) \cos(ky) dy \\ &= \partial_x \sigma_x \partial_x \widetilde{\phi}(k)\end{aligned} \tag{A.1}$$

with

$$\widetilde{\phi}(k) = \int_0^\infty \phi(y) \cos(ky) dy.$$

Similar, the fourth term results in

$$\int_0^\infty (\partial_z \sigma_z)(\partial_z \phi(y)) \cos(ky) dy = \partial_z \sigma_z \partial_z \widetilde{\phi}(k). \tag{A.2}$$

The second term yields

$$\begin{aligned}\int_0^\infty (\sigma_x \partial_x^2 \phi(y)) \cos(ky) dy &= \sigma_x \partial_x^2 \int_0^\infty \phi(y) \cos(ky) dy \\ &= \sigma_x \partial_x^2 \widetilde{\phi}(k).\end{aligned} \tag{A.3}$$

Similarly, the fifth term results in

$$\int_0^\infty (\sigma_z \partial_z^2 \phi(y)) \cos(ky) dy = \sigma_z \partial_z^2 \widetilde{\phi}(k). \tag{A.4}$$

The third term can be treated by exploiting the symmetries $\phi(y) = \phi(-y)$ and $\widetilde{\phi}(k) = \widetilde{\phi}(-k)$, leading to

$$\begin{aligned}\widetilde{\phi}(k) \int_0^\infty \phi(y)\cos(ky)dy &= \frac{1}{2}\int_{-\infty}^{\infty} \phi(y)\cos(ky)dy \\ &= \frac{1}{2}\int_{-\infty}^{\infty} \phi(y)\,\mathrm{e}^{iky}\,dy\end{aligned} \tag{A.5}$$

and

$$\begin{aligned}\phi(y) &= \frac{2}{\pi}\int_0^\infty \widetilde{\phi}(k)\cos(ky)dy \\ &= \frac{1}{\pi}\int_{-\infty}^{\infty} \widetilde{\phi}(k)\exp^{-iky}\,dk.\end{aligned} \tag{A.6}$$

With

$$\partial_y^2\phi(y) = -\frac{1}{\pi}\int_{-\infty}^{\infty} \widetilde{\phi}(k)k^2\,\mathrm{e}^{-iky}\,dk$$

and

$$\delta(k-k') = \frac{1}{2}\int_{-\infty}^{\infty} \mathrm{e}^{i(k-k')y}\,dy,$$

the third term may be transformed to

$$\begin{aligned}\int_0^\infty \sigma_y\partial_y^2\phi(y)\cos(ky)dy &= \frac{1}{2}\int_{-\infty}^{\infty} \sigma_y(-\frac{1}{\pi}\int_{-\infty}^{\infty} \widetilde{\phi}(k')k'^2\exp^{-ik'y}\,dk')\,\mathrm{e}^{iky}\,dy \\ &= -\frac{1}{2\pi}\int_{-\infty}^{\infty} \widetilde{\phi}(k')k'^2\,\mathrm{e}^{i(k-k')y}\,dk'dy \\ &= -\sigma_y\int_{-\infty}^{\infty} \widetilde{\phi}(k')k'^2\left(\frac{1}{2\pi}\int_{-\infty}^{\infty}\mathrm{e}^{i(k-k')y}\,dy\right)dk' \\ &= -\sigma_y\int_{-\infty}^{\infty} \widetilde{\phi}(k')k'^2\delta(k-k')dk' \\ &= -\sigma_y k^2\widetilde{\phi}(k).\end{aligned} \tag{A.7}$$

Because of $\delta(y-0) = \delta(-y-0)$, the fifth term may be written as

$$\begin{aligned}\int_0^\infty I\delta(x-x_s)\delta(y-y_s)\delta(z-z_s) &= \delta(x-x_s)\delta(z-z_s)\frac{I}{2}\int_{-\infty}^{\infty}\delta(y-0)\cos(ky)dy \\ &= 0.\end{aligned} \tag{A.8}$$

In total, the individual terms form the final Helmholtz equation 3.5 is

$$\begin{aligned} &\partial_x \sigma_x \partial_x \widetilde{\phi}(k) + \sigma_x \partial_x^2 \widetilde{\phi}(k) - \sigma_y k^2 \widetilde{\phi}(k) + \partial_z \sigma_z \partial_z \widetilde{\phi}(k) + \sigma_z \partial_x^2 \widetilde{\phi}(k) \\ &\qquad + \frac{I}{2} \delta(x - x_s) \delta(z - z_s) = 0 \\ \Leftrightarrow\ &\partial_x (\sigma_x \partial_x \widetilde{\phi}(k)) - \sigma_y k^2 \widetilde{\phi}(k) + \partial_z (\sigma_z \partial_z \widetilde{\phi}(k)) + \frac{I}{2} \delta(x - x_s) \delta(z - z_s) = 0. \end{aligned} \tag{A.9}$$

B

Element Types

B.1 Boundary Elements with Linear Ansatz Function

In this appendix, straight boundary elements with a linear ansatz function

$$\widetilde{\phi}(s) \approx c_1^{(j)} + c_2^{(j)} s$$

with $s \in (\partial G)^{(j)}$ and $(j = 1, ..., n_r)$ are considered. The node variables $\widetilde{\phi}_{i_1(j)}, \widetilde{\phi}_{i_2(j)}$ with $(i_1(j), i_2(j) \in \{1, ..., n_k\})$ determine the coefficients $c_1^{(j)}$ and $c_2^{(j)}$ on $(\partial G)^{(j)}$. By this ansatz function it follows (Schwarz, 1991b)

$$\int_{C^{(j)}} \widetilde{\phi}^2 ds = \underline{\widetilde{\boldsymbol{\phi}}}^{(j)^T} \boldsymbol{S}_3'^{(j)} \underline{\widetilde{\boldsymbol{\phi}}}^{(j)} \text{ with } \boldsymbol{S}_3'^{(j)} = \frac{L^{(j)}}{6} \begin{pmatrix} 2 & 1 \\ 1 & 2 \end{pmatrix}, \tag{B.1}$$

with $L^{(j)}$ being the length of the boundary section j and $\underline{\widetilde{\boldsymbol{\phi}}^{(j)}} = (\widetilde{\phi}_{i_1(j)}, \widetilde{\phi}_{i_2(j)})$ being the vector of all node values of the regarded element j. The matrices $\boldsymbol{S}_3'^{(j)}$ can be composed to be linked to a latter implementation into an computer algorithm through expanding them into a $n_k \times n_k$ matrix $S^{(j)}$. In this new matrix, the nodes of element j are identified in the set of all nodes on the total domain G. Consequently, the matrices in eq. B.1 are spread over the larger matrix $S^{(j)}$ in the following manner

$$(S_3^{(j)})_{mn} = \begin{cases} (s'^{(j)}_3)_{\kappa\lambda} & \text{, if } \quad \kappa, \lambda \in \{1, 2\} \text{ with } m = i_\kappa(j) \text{ and } n = i_\lambda(j) \\ 0 & \text{, else.} \end{cases} \tag{B.2}$$

In this case, the vectors $\underline{\widetilde{\boldsymbol{\phi}}}^{(j)}$ translate to

$$\underline{\widetilde{\boldsymbol{\phi}}} = (\widetilde{\phi}_1, \widetilde{\phi}_2, ..., \widetilde{\phi}_{n_k}).$$

It follows that

$$\underline{\widetilde{\boldsymbol{\phi}}}^{(j)^T} \boldsymbol{S}_3'^{(j)} \underline{\widetilde{\boldsymbol{\phi}}}^{(j)} = \underline{\widetilde{\boldsymbol{\phi}}}^T \boldsymbol{S}_3{}^{(j)} \underline{\widetilde{\boldsymbol{\phi}}}. \tag{B.3}$$

B.2 Triangular Elements with Linear Ansatz Function

It is assumed that the regarded subdomain $G^{(j)}$ is a triangle. From eq. 3.11, the following integrals have to be computed:

$$\iint_{G^{(j)}} (\frac{\partial \widetilde{\phi}}{\partial x})^2 dx dz \tag{B.4}$$

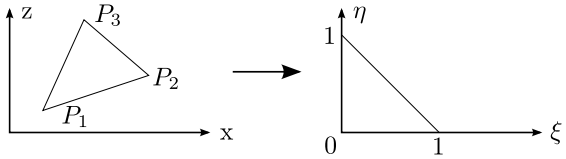

Figure B.1: Transformation of an arbitrary triangle into a unity triangle. Modified after Schwarz (1991b).

$$\iint_{G^{(j)}} (\frac{\partial \widetilde{\phi}}{\partial z})^2 dxdz \tag{B.5}$$

$$\iint_{G^{(j)}} \widetilde{\phi}^2 dxdz \tag{B.6}$$

Every straight triangle can be transformed into an unity triangle (see figure B.1) with

$$\frac{\partial \xi}{\partial x} = \frac{\partial \widetilde{\phi}}{\partial \xi}\frac{\partial \xi}{\partial x} + \frac{\partial \widetilde{\phi}}{\partial \eta}\frac{\partial \eta}{\partial x}$$

and, correspondingly,

$$\frac{\partial \xi}{\partial z} = \frac{\partial \widetilde{\phi}}{\partial \xi}\frac{\partial \xi}{\partial z} + \frac{\partial \widetilde{\phi}}{\partial \eta}\frac{\partial \eta}{\partial z}.$$

Here,

$$\frac{\partial \xi}{\partial x} = \frac{z_3 - z_1}{J} = \xi_x \text{ and} \frac{\partial \eta}{\partial x} = -\frac{z_2 - z_1}{J} = \eta_x$$

and

$$\frac{\partial \xi}{\partial z} = -\frac{x_3 - x_1}{J} = \xi_z \text{ and } \frac{\partial \eta}{\partial z} = \frac{z_2 - z_1}{J} = \eta_z$$

with the Jacobian determinant

$$J = \begin{vmatrix} \frac{\partial x}{\partial \xi} & \frac{\partial y}{\partial \xi} \\ \frac{\partial x}{\partial \eta} & \frac{\partial y}{\partial \eta} \end{vmatrix}. \tag{B.7}$$

Consequently, eq. B.4 yields

$$\begin{aligned}
\iint_{G^{(j)}} (\frac{\partial \widetilde{\phi}}{\partial x})^2 dxdz &= \iint_{G_0} (\frac{\partial \widetilde{\phi}}{\partial \xi}\frac{\partial \xi}{\partial x} + \frac{\partial \widetilde{\phi}}{\partial \eta}\frac{\partial \eta}{\partial x})^2 J d\xi d\eta \\
&= \iint_{G_0} (\widetilde{\phi}_\xi^2 \xi_x^2 + 2\widetilde{\phi}_\xi \widetilde{\phi}_\eta \xi_x \eta_x + \widetilde{\phi}_\eta^2 \eta_x^2) J d\xi d\eta \\
&= a^{(x)} \iint_{G_0} \widetilde{\phi}_\xi^2 d\xi d\eta + 2b^{(x)} \iint_{G_0} \widetilde{\phi}_\xi \widetilde{\phi}_\eta d\xi d\eta \\
&\quad + c^{(x)} \iint_{G_0} \widetilde{\phi}_\eta^2 d\xi d\eta
\end{aligned}$$

with the coefficients

$$\begin{aligned}
a^{(x)} &= J \cdot \xi_x^2 = \frac{(z_3 - z_1)^2}{J} \\
b^{(x)} &= J \cdot \xi_x \eta_x = \frac{-(z_3 - z_1) \cdot (z_2 - z_1}{J} \\
c^{(x)} &= J \cdot \eta_x^2 = \frac{(z_2 - z_1)^2}{J}.
\end{aligned}$$

Likewise, eq. B.5 yields

$$\begin{aligned}\iint_{G^{(j)}}(\frac{\partial\widetilde{\phi}}{\partial z})^2dxdz &= \iint_{G_0}(\frac{\partial\widetilde{\phi}}{\partial\xi}\frac{\partial\xi}{\partial z}+\frac{\partial\widetilde{\phi}}{\partial\eta}\frac{\partial\eta}{\partial z})^2Jd\xi d\eta\\ &= a^{(z)}\iint_{G_0}\widetilde{\phi}_\xi^2d\xi d\eta+2b^{(z)}\iint_{G_0}\widetilde{\phi}_\xi\widetilde{\phi}_\eta d\xi d\eta\\ &+c^{(z)}\iint_{G_0}\widetilde{\phi}_\eta^2d\xi d\eta\end{aligned}$$

with the coefficients

$$\begin{aligned}a^{(z)} &= J\cdot\xi_z^2=\frac{(x_3-x_1)^2}{J}\\ b^{(z)} &= J\cdot\xi_z\eta_z=\frac{-(x_3-x_1)\cdot(x_2-x_1}{J}\\ c^{(z)} &= J\cdot\eta_z^2=\frac{(x_2-x_1)^2}{J}.\end{aligned}$$

With the unity triangle notation, the third integral part (eq. B.6) yields

$$\iint_{G^{(j)}}\widetilde{\phi}^2dxdz=J\iint_{G_0}\widetilde{\phi}^2d\xi d\eta$$

If a linear ansatz

$$\widetilde{\phi}(x,z)=c_1^{(j)}+c_2^{(j)}x+c_3^{(j)}z \tag{B.8}$$

is chosen with the constraining edge nodes $\widetilde{\phi}_{i_1(j)},\widetilde{\phi}_{i_2(j)},\widetilde{\phi}_{i_3(j)}$ with (x_κ,z_κ), $(\kappa=1,2,3)$, then the same ansatz can be formulated on the unity triangle as

$$\widetilde{\phi}(\xi,\eta)=\alpha_1^{(j)}+\alpha_2^{(j)}\xi+\alpha_3^{(j)}\eta.$$

Inserting the ansatz function eq. B.8 into eq. B.4 then yields

$$\begin{aligned}\iint_{G_0}(\frac{\partial\widetilde{\phi}}{\partial x})^2 &= a^{(x)}\iint_{G_0}{\alpha_2^{(j)}}^2d\xi d\eta+2b^{(x)}\iint_{G_0}\alpha_2^{(j)}\alpha_3^{(j)}d\xi d\eta\\ &+c^{(x)}\iint_{G_0}{\alpha_3^{(j)}}^2d\xi d\eta\\ &= a^{(x)}\frac{1}{2}{\alpha_2^{(j)}}^2+2b^{(x)}\alpha_2\alpha_3+c^{(x)}\frac{1}{2}{\alpha_3^{(j)}}^2.\end{aligned}$$

Likewise, the integral in eq. B.5 yields

$$\begin{aligned}\iint_{G_0}(\frac{\partial\widetilde{\phi}}{\partial z})^2 &= a^{(z)}\iint_{G_0}{\alpha_2^{(j)}}^2d\xi d\eta+2b^{(z)}\iint_{G_0}\alpha_2^{(j)}\alpha_3^{(j)}d\xi d\eta\\ &+c^{(z)}\iint_{G_0}{\alpha_3^{(j)}}^2d\xi d\eta\\ &= a^{(z)}\frac{1}{2}{\alpha_2^{(j)}}^2+2b^{(z)}\alpha_2\alpha_3+c^{(z)}\frac{1}{2}{\alpha_3^{(j)}}^2.\end{aligned}$$

The third integral (eq. B.6) yields according to Schwarz (1991b)

$$\begin{aligned}\iint_{G^{(j)}}\widetilde{\phi}^2dxdz &= J\iint_{G_0}\widetilde{\phi}^2d\xi d\eta\\ &= J(\frac{1}{2}\alpha_1^2+\frac{1}{3}\alpha_1\alpha_2+\frac{1}{3}\alpha_1\alpha_3+\frac{1}{12}\alpha_2^2+\frac{1}{12}\alpha_2\alpha_3+\frac{1}{12}\alpha_3^2).\end{aligned}$$

Combined, the total integral over the subdomain element $G^{(j)}$ yields

$$\begin{aligned}
F &= \frac{1}{2}\sigma_x(a^{(x)} \cdot \frac{1}{2}{\alpha_2^{(j)}}^2 + 2b^{(x)}\alpha_2^{(j)}\alpha_3^{(j)} + c^{(x)}\frac{1}{2}{\alpha_3^{(j)}}^2) \\
&\quad + \frac{1}{2}\sigma_z(a^{(z)} \cdot \frac{1}{2}{\alpha_2^{(j)}}^2 + 2b^{(z)}\alpha_2^{(j)}\alpha_3^{(j)} + c^{(z)}\frac{1}{2}{\alpha_3^{(j)}}^2) \\
&\quad + \frac{1}{2}\sigma_y k^2(J(\frac{1}{2}\alpha_1^2 + \frac{1}{3}\alpha_1\alpha_2 + \frac{1}{3}\alpha_1\alpha_3 + \frac{1}{12}\alpha_2^2 + \frac{1}{12}\alpha_2\alpha_3 + \frac{1}{12}\alpha_3^2)) \\
&\quad - \iint_{G^{(j)}} \frac{I}{2}\delta(x - x_s)\delta(z - z_s)\widetilde{\phi}dxdz \\
&= \frac{1}{2}[(\sigma_x a^{(x)} + \sigma_z a^{(z)})\frac{1}{2}{\alpha_2^{(j)}}^2 + (\sigma_x b^{(j)} + \sigma_z b^{(j)})2\alpha_2^{(j)}\alpha_3^{(j)} \\
&\quad + (\sigma_x c^{(x)} + \sigma_z c^{(z)})\frac{1}{2}{\alpha_3^{(j)}}^2] \\
&\quad + \frac{1}{2}\sigma_y k^2(J(\frac{1}{2}\alpha_1^2 + \frac{1}{3}\alpha_1\alpha_2 + \frac{1}{3}\alpha_1\alpha_3 + \frac{1}{12}\alpha_2^2 + \frac{1}{12}\alpha_2\alpha_3 + \frac{1}{12}\alpha_3^2)) \\
&\quad - \iint_{G^{(j)}} \frac{I}{2}\delta(x - x_s)\delta(z - z_s)\widetilde{\phi}dxdz.
\end{aligned}$$

In matrix notation, the above expression can be written as (cf. Schwarz (1991b))

$$\begin{aligned}
F = \frac{1}{2}[&\left(\sigma_x a^{(x)} + \sigma_z a^{(z)}\right)\underline{\boldsymbol{\alpha}}^{(j)^T}\widetilde{\boldsymbol{S}}_1\underline{\boldsymbol{\alpha}}^{(j)} \\
&+ \left(\sigma_x b^{(x)} + \sigma_z b^{(z)}\right)\underline{\boldsymbol{\alpha}}^{(j)^T}\widetilde{\boldsymbol{S}}_2\underline{\boldsymbol{\alpha}}^{(j)} \\
&+ \left(\sigma_x c^{(x)} + \sigma_z c^{(z)}\right)\underline{\boldsymbol{\alpha}}^{(j)^T}\widetilde{\boldsymbol{S}}_3\underline{\boldsymbol{\alpha}}^{(j)}] \\
&+ \frac{1}{2}\sigma_y k^2 J\underline{\boldsymbol{\alpha}}^{(j)^T}\widetilde{\boldsymbol{S}}_4\underline{\boldsymbol{\alpha}}^{(j)} \\
&- \iint_{G^{(j)}} \frac{I}{2}\delta(x - x_s)\delta(z - z_s)\widetilde{\phi}dxdz
\end{aligned}$$

with the vectors $\underline{\boldsymbol{\alpha}}^{(j)} = (\alpha_1^{(j)}, \alpha_2^{(j)}, \alpha_3^{(j)})^T$ and the matrices

$$\widetilde{\boldsymbol{S}}_1 = \frac{1}{2}\begin{pmatrix} 0 & 0 & 0 \\ 0 & 1 & 0 \\ 0 & 0 & 0 \end{pmatrix}, \quad \widetilde{\boldsymbol{S}}_2 = \frac{1}{2}\begin{pmatrix} 0 & 0 & 0 \\ 0 & 0 & 1 \\ 0 & 1 & 0 \end{pmatrix}$$

$$\widetilde{\boldsymbol{S}}_3 = \frac{1}{2}\begin{pmatrix} 0 & 0 & 0 \\ 0 & 0 & 0 \\ 0 & 0 & 1 \end{pmatrix}, \quad \widetilde{\boldsymbol{S}}_4 = \frac{1}{24}\begin{pmatrix} 12 & 4 & 4 \\ 4 & 2 & 1 \\ 4 & 1 & 2 \end{pmatrix}.$$

The back-transform into (x, z) can be seen through (see above):

$$\widetilde{\phi}_1^{(j)} = \alpha_1^{(j)}$$

$$\widetilde{\phi}_2^{(j)} = \alpha_1^{(j)} + \alpha_2^{(j)}$$

$$\widetilde{\phi}_3^{(j)} = \alpha_1^{(j)} + \alpha_3^{(j)}.$$

Explicitly, it is

$$\alpha_1^{(j)} = \widetilde{\phi}_1^{(j)}$$

$$\alpha_2^{(j)} = -\widetilde{\phi}_1^{(j)} + \widetilde{\phi}_2^{(j)}$$
$$\alpha_3^{(j)} = -\widetilde{\phi}_1^{(j)} + \widetilde{\phi}_3^{(j)}$$

or, in matrix-vector notation,

$$\underline{\boldsymbol{\alpha}}^{(j)} = \boldsymbol{A} \cdot \underline{\widetilde{\boldsymbol{\phi}}}^{(j)}$$

with the matrix

$$\boldsymbol{A} = \begin{pmatrix} 1 & 0 & 0 \\ -1 & 1 & 0 \\ -1 & 0 & 1 \end{pmatrix}.$$

In conclusion, the back-transform is

$$\begin{aligned}
&\frac{1}{2}[\left(\sigma_x a^{(x)} + \sigma_z a^{(z)}\right) \underline{\widetilde{\boldsymbol{\phi}}}^{(j)^T} \boldsymbol{A}^T \widetilde{\boldsymbol{S}}_1 \boldsymbol{A} \cdot \underline{\widetilde{\boldsymbol{\phi}}}^{(j)} \\
&\quad + \left(\sigma_x b^{(x)} + \sigma_z b^{(z)}\right) \underline{\widetilde{\boldsymbol{\phi}}}^{(j)^T} \boldsymbol{A}^T \widetilde{\boldsymbol{S}}_2 \boldsymbol{A} \cdot \underline{\widetilde{\boldsymbol{\phi}}}^{(j)} \\
&\quad + \left(\sigma_x c^{(x)} + \sigma_z c^{(z)}\right) \underline{\widetilde{\boldsymbol{\phi}}}^{(j)^T} \boldsymbol{A}^T \widetilde{\boldsymbol{S}}_3 \boldsymbol{A} \cdot \underline{\widetilde{\boldsymbol{\phi}}}^{(j)}] \\
&\quad + \frac{1}{2}\sigma_y k^2 J \underline{\widetilde{\boldsymbol{\phi}}}^{(j)^T} \boldsymbol{A}^T \widetilde{\boldsymbol{S}}_4 \boldsymbol{A} \cdot \underline{\widetilde{\boldsymbol{\phi}}}^{(j)} \\
=&\frac{1}{2}[\left(\sigma_x a^{(x)} + \sigma_z a^{(z)}\right) \underline{\widetilde{\boldsymbol{\phi}}}^{(j)^T} \boldsymbol{S}_1 \cdot \underline{\widetilde{\boldsymbol{\phi}}}^{(j)} \\
&\quad + \left(\sigma_x b^{(x)} + \sigma_z b^{(z)}\right) \underline{\widetilde{\boldsymbol{\phi}}}^{(j)^T} \boldsymbol{S}_2 \cdot \underline{\widetilde{\boldsymbol{\phi}}}^{(j)} \\
&\quad + \left(\sigma_x c^{(x)} + \sigma_z c^{(z)}\right) \underline{\widetilde{\boldsymbol{\phi}}}^{(j)^T} \boldsymbol{S}_3 \cdot \underline{\widetilde{\boldsymbol{\phi}}}^{(j)}] \\
&\quad + \frac{1}{2}\sigma_y k^2 J \underline{\widetilde{\boldsymbol{\phi}}}^{(j)^T} \boldsymbol{S}_4 \cdot \underline{\widetilde{\boldsymbol{\phi}}}^{(j)}
\end{aligned}$$

with the matrices

$$\boldsymbol{S}_1 = \frac{1}{2}\begin{pmatrix} 1 & -1 & 0 \\ -1 & 1 & 0 \\ 0 & 0 & 0 \end{pmatrix}, \quad \boldsymbol{S}_2 = \frac{1}{2}\begin{pmatrix} 2 & -1 & -1 \\ -1 & 0 & 1 \\ -1 & 1 & 0 \end{pmatrix}$$
$$\boldsymbol{S}_3 = \frac{1}{2}\begin{pmatrix} 1 & 0 & -1 \\ 0 & 0 & 0 \\ -1 & 0 & 1 \end{pmatrix}, \quad \boldsymbol{S}_4 = \frac{1}{24}\begin{pmatrix} 2 & 1 & 1 \\ 1 & 2 & 1 \\ 1 & 1 & 2 \end{pmatrix}.$$

This equation may be concatenated:

$$\begin{aligned}
&\frac{1}{2}\underline{\widetilde{\boldsymbol{\phi}}}^{(j)^T} \boldsymbol{S}_1'^{(j)} \underline{\widetilde{\boldsymbol{\phi}}}^{(j)} \\
&+ \frac{1}{2}\underline{\widetilde{\boldsymbol{\phi}}}^{(j)^T} \boldsymbol{S}_2'^{(j)} \underline{\widetilde{\boldsymbol{\phi}}}^{(j)}
\end{aligned} \tag{B.9}$$

with the combined matrices

$$\begin{aligned}
\boldsymbol{S}_1'^{(j)} =&(\sigma_x a^{(x)} + \sigma_z a^{(z)})\boldsymbol{S}_1 + (\sigma_x b^{(x)} + \sigma_z b^{(z)})\boldsymbol{S}_2 \\
&+ (\sigma_x c^{(x)} + \sigma_z c^{(z)})\boldsymbol{S}_3 \\
\boldsymbol{S}_2'^{(j)} =&\sigma_y k^2 J \boldsymbol{S}_4.
\end{aligned} \tag{B.10}$$

The above computed 3×3 matrices $\boldsymbol{S}_1'^{(j)}$ and $\boldsymbol{S}_2'^{(j)}$ may be written as $n_k \times n_k$ matrices (see section B.1).

C

Mixed Boundary Conditions in the Case of Anisotropy

According to Telford *et al.* (1990), the equipotential lines in the case of horizontal-vertical anisotropy (with conductivities σ_h and σ_v,respectively) are ellipsoids:

$$\phi(\vec{r}) = \frac{I}{2\pi\sqrt{\sigma_h\sigma_v}}\frac{1}{|\vec{r}|}. \tag{C.1}$$

To account for the elliptical potentials, the transformations

$$x = \sqrt{\sigma_x}\alpha \quad \text{and} \quad z = \sqrt{\sigma_z}\epsilon \tag{C.2}$$

$$\frac{\partial}{\partial_x} = \frac{1}{\sqrt{\sigma_x}}\frac{\partial}{\partial_\alpha} \qquad \partial_z = \frac{1}{\sqrt{\sigma_z}}\partial_\epsilon \tag{C.3}$$

and

$$k = \frac{1}{\sqrt{\sigma_y}}\kappa. \tag{C.4}$$

can be applied to yield

$$\partial_\alpha^2\widetilde{\phi} + \partial_\epsilon^2\widetilde{\phi} - \kappa^2\widetilde{\phi} + I\delta(\alpha - \alpha_s)\delta(\epsilon - \epsilon_s) = 0. \tag{C.5}$$

In this transformed space, the boundary condition is

$$\partial_n\phi + \beta^*\phi = 0 \tag{C.6}$$

and the now isotropic analytical potential can be written as

$$\widetilde{\phi}_p(\kappa, r') = \frac{I}{2\pi}K_0(\kappa r') \tag{C.7}$$

$$r' = \sqrt{(\alpha - \alpha_s)^2 + (\epsilon - \epsilon_s)^2}. \tag{C.8}$$

Inserting this into eq. C.6 yields

$$\begin{aligned} &\partial_n K_0(\kappa r) + \beta K_0(\kappa r) = 0 \\ \Leftrightarrow\ &\beta = \kappa \cdot g \end{aligned} \tag{C.9}$$

with

$$g = \frac{K_1(\kappa r)\partial_n r}{K_0(\kappa r)}. \tag{C.10}$$

The derivative in normal direction can be expressed as

$$\partial_n r = (\vec{\nabla} r)\vec{n}. \tag{C.11}$$

It is important to note that, here, the derivatives $\vec{\nabla}$ as well as the normal vector resides in the $(\alpha, \kappa, \epsilon)$ space. The back-transformation in the (α, k, ϵ) space can be accomplished by

$$\kappa = \sqrt{\sigma_y} k \tag{C.12}$$

$$g = \frac{K_1(\sqrt{\sigma_y} k r)\partial_n r}{K_0(\sqrt{\sigma_y} k r)}. \tag{C.13}$$

Back-transformation into the (x, k, z) space with

$$\alpha = \frac{1}{\sqrt{\sigma_x}} x \quad \text{and} \quad \epsilon = \frac{1}{\sqrt{\sigma_z}} z \tag{C.14}$$

$$\partial_\alpha = \sqrt{\sigma_x}\partial_x \quad \text{and} \quad \partial_\epsilon = \sqrt{\sigma_z}\partial_z \tag{C.15}$$

yields

$$r = \sqrt{\alpha^2 + \epsilon^2} \tag{C.16}$$

$$= \sqrt{\frac{1}{\sigma_x} x^2 + \frac{1}{\sigma_z} z^2} \tag{C.17}$$

$$\begin{aligned} \partial_n r =& \sqrt{\sigma_x}\partial_x \sqrt{\frac{1}{\sigma_x} x^2 + \frac{1}{\sigma_z} z^2} \cdot \sqrt{\sigma_x} n_x + \\ & \sqrt{\sigma_z}\partial_z \sqrt{\frac{1}{\sigma_x} x^2 + \frac{1}{\sigma_z} z^2} \cdot \sqrt{\sigma_z} n_z \\ =& \sigma_x \partial_x \sqrt{\frac{1}{\sigma_x} x^2 + \frac{1}{\sigma_z} z^2} n_x + \\ & \sigma_z \partial_z \sqrt{\frac{1}{\sigma_x} x^2 + \frac{1}{\sigma_z} z^2} n_z \\ =& \frac{1}{\sqrt{\frac{1}{\sigma_x} x^2 + \frac{1}{\sigma_z} z^2}} \cdot \left(\sqrt{\sigma_x} x n_x + \sqrt{\sigma_z} z n_z\right). \end{aligned} \tag{C.18}$$

Inserting this yields

$$r_- = \sqrt{\frac{1}{\sigma_x}(x)^2 + \frac{1}{\sigma_z}(z)^2} \tag{C.19}$$

$$r_+ = \sqrt{\frac{1}{\sigma_x}(x)^2 + \frac{1}{\sigma_z}(z)^2} \tag{C.20}$$

$$\begin{aligned}\partial_n r =&\sqrt{\sigma_x}\partial_x\sqrt{\frac{1}{\sigma_x}(x)^2+\frac{1}{\sigma_z}(z)^2}+\\ &\sqrt{\sigma_z}\partial_z\sqrt{\frac{1}{\sigma_x}(x)^2+\frac{1}{\sigma_z}(z)^2}.\end{aligned} \tag{C.21}$$

This result may be tested with setting all $\sigma_{x,y,z}$. It follows that

$$r =\frac{1}{\sqrt{\sigma}}\sqrt{(x)^2+(z)^2}. \tag{C.22}$$

This complies to the known isotropic computations where the conductivity needs to be multiplied:

$$\begin{aligned}\partial_n r =&\sqrt{\sigma_x}\partial_x\sqrt{(x)^2+(z)^2}+\\ &\sqrt{\sigma_z}\partial_z\sqrt{(x)^2+(z)^2}\end{aligned} \tag{C.23}$$

$$K_1\left(\sqrt{\sigma}kr\right) = K_1\left(k\sqrt{(x)^2+(z)^2}\right) \tag{C.24}$$

$$K_0\left(\sqrt{\sigma}kr\right) = ... \tag{C.25}$$

Inserting this into the β formula

$$\beta =\kappa g \tag{C.26}$$

$$=\sqrt{\sigma}k\cdot\frac{K_1(\sqrt{\sigma}kr)\partial_n r}{K_0(\sqrt{\sigma}kr)} \tag{C.27}$$

$$=\sqrt{\sigma}k\frac{K_1\left(k\sqrt{x^2+z^2}\right)\partial_n r}{K_0\left(...\right)} \tag{C.28}$$

$$=\sqrt{\sigma}k\left(\frac{K_1\left(...\right)\left(\sqrt{\sigma}\partial_x\sqrt{x^2+z^2}+...\right)+}{K_0\left(...\right)}\right) \tag{C.29}$$

$$=\sigma k\frac{K_1(...)\partial_x\sqrt{x^2+z^2}+...}{K_0(...)}. \tag{C.30}$$

Eventually, this falls back to the isotropic case.

C.1 Principle of Reciprocity with anisotropic complex conductivity distribution

In this appendix it is shown that – according to the derviation an notation of Friedel (2000) for the isotropic DC case – the principle of reciprocity is also true in the case of an anisotropic complex conductivity distribution.

Let ϕ_A and ϕ_M be the complex electric potential distributions due to the source current densities $\mathbf{j}_A$ and $\mathbf{j}_M$, respectively, in a medium with anisotropic complex conductivity distribution σ. The corresponding Poisson equations are

$$\nabla\cdot\mathbf{j}_A = -\nabla\cdot\left(\boldsymbol{\sigma}\nabla\phi_A\right), \nabla\cdot\mathbf{j}_M = -\nabla\cdot\left(\boldsymbol{\sigma}\nabla\phi_M\right). \tag{C.31}$$

From eq. C.31, one obtains

$$\nabla\cdot\left(\phi_M\mathbf{j}_A-\phi_A\mathbf{j}_M\right)=\phi_M\nabla\cdot\mathbf{j}_A-\left(\nabla\phi_M\right)\boldsymbol{\sigma}\left(\nabla\phi_A\right)-\phi_A\nabla\cdot\mathbf{j}_M+\left(\nabla\phi_A\right)\boldsymbol{\sigma}(\nabla\phi_M). \quad \text{(C.32)}$$

Since the conductivity tensor $\boldsymbol{\sigma}$ is symmetric, one finds (using Einstein's summation convention)

$$\begin{aligned}\left(\nabla\phi_M\right)\boldsymbol{\sigma}\left(\nabla\phi_A\right)&=\left(\partial_{x_i}\phi_M\right)\sigma_{ij}\left(\partial_{x_j}\phi_A\right)\\&=\left(\partial_{x_i}\phi_M\right)\sigma_{ji}\left(\partial_{x_j}\phi_A\right)\\&=\left(\partial_{x_j}\phi_M\right)\sigma_{ij}\left(\partial_{x_i}\phi_A\right)\\&=\left(\nabla\phi_A\right)\boldsymbol{\sigma}\left(\nabla\phi_M\right)\end{aligned} \quad \text{(C.33)}$$

and thus eq. C.32 simplifies to

$$\nabla\cdot\left(\phi_M\mathbf{j}_A-\phi_A\mathbf{j}_M\right)=\phi_M\nabla\cdot\mathbf{j}_A-\phi_A\nabla\cdot\mathbf{j}_M. \quad \text{(C.34)}$$

Integrating eq. C.34 over the considered domain Ω and applying Gauss' Law yields

$$\begin{aligned}\int_\Omega\left(\phi_M\nabla\cdot\mathbf{j}_A-\phi_A\nabla\cdot\mathbf{j}_M\right)dV&=\int_\Omega\nabla\cdot\left(\phi_M\mathbf{j}_A-\phi_A\mathbf{j}_M\right)dV\\&=\int_{\partial\Omega}\left(\phi_M\mathbf{j}_A-\phi_A\mathbf{j}_M\right)\mathbf{n}dA\end{aligned} \quad \text{(C.35)}$$

where $\mathbf{n}$ is the normal vector of the surface element dA on the boundary $\partial\Omega$ of the considered domain. If the boundary is assumed to be infinitely far away from the current sources, the integral on the right-hand side of eq. C.35 vanishes (since $|\phi_M\mathbf{j}_A|$ and $|\phi_A\mathbf{j}_M|$ fall off with $\left(\frac{1}{r}\cdot\frac{1}{r^2}\right)$ while the total surface A grows only with r^2, where r is the average distance to the boundary). Assuming point current sources at $\mathbf{r}_A$ and $\mathbf{r}_M$ with strengths I_A and I_M, respectively, i.e., $\nabla\mathbf{j}_A=I_A\delta\left(\mathbf{r}-\mathbf{r}_A\right),\nabla\mathbf{j}_M=I_M\delta\left(\mathbf{r}-\mathbf{r}_M\right)$, one therefore obtains

$$\int_\Omega\left(\phi_MI_A\delta\left(\mathbf{r}-\mathbf{r}_A\right)-\phi_AI_M\delta\left(\mathbf{r}-\mathbf{r}_M\right)\right)dV=0 \quad \text{(C.36)}$$

and thus, with the properties of the Dirac delta function, ultimately

$$\begin{aligned}\phi_M\left(\mathbf{r}_A\right)I_A-\phi_A\left(\mathbf{r}_M\right)I_M&=0\\\Leftrightarrow\frac{\phi_M\left(\mathbf{r}_A\right)}{I_M}&=\frac{\phi_A\left(\mathbf{r}_M\right)}{I_A}.\end{aligned} \quad \text{(C.37)}$$

Equation C.37 states that the potential ϕ_M at point $\mathbf{r}_A$due to the current I_M at $\mathbf{r}_M$, normalized by I_M, is equal to the potential ϕ_A at point $\mathbf{r}_M$ due to the current I_A at $\mathbf{r}_A$, normalized by I_A, which is referred to as the principle of reciprocity. Extension to a four-electrode measurement configuration is obtained by means of superposition.

C.2 Sensitivity with respect to anisotropy ratio

The sensitivity $\frac{\partial Z}{\partial\lambda_{kl}},(k,l)\in\{x,y,z\}$ with respect to the anisotropy ratio $\lambda_{kl}=\frac{\sigma_k}{\sigma_l}$ can be written as

$$\frac{\partial Z}{\partial\lambda_{kl}}=\frac{\partial Z}{\partial\sigma_k}\frac{\partial\sigma_k}{\partial\lambda_{kl}}+\frac{\partial Z}{\partial\sigma_l}\frac{\partial\sigma_l}{\partial\lambda_{kl}} \quad \text{(C.38)}$$

Because of $\frac{\partial \lambda_{kl}}{\partial \sigma_k} = \frac{1}{\sigma_l}$ and $\frac{\partial \lambda_{kl}}{\partial \sigma_l} = -\frac{1}{\sigma_k}\lambda_{kl}^2$ one obtains

$$\frac{\partial Z}{\partial \lambda_{kl}} = \sigma_l \frac{\partial Z}{\partial \sigma_k} - \frac{\sigma_k}{\lambda_{kl}^2}\frac{\partial Z}{\partial \sigma_l} \tag{C.39}$$

Bibliography

ANDERSON, L., & KELLER, G. 1964. A study in induced polarization. *Geophysics*, **29**(5), 848–864.

BAKER, A. 2013. Simplicity. *In:* ZALTA, E. N. (ed), *The Stanford Encyclopedia of Philosophy*, fall 2013 edn. Metaphysics Research Lab, CSLI, Stanford University.

BÜCKER, M. 2011. *Die Membranpolarisation als Ursache des IP-Effekts in porösen Medien*. Masters thesis, Technische Universität Braunschweig.

BHATTACHARYA, B., & SRIVASTAVA, S. 2016. *Geoelectric methods: Theory and application*. McGraw-Hill Education.

BHATTACHARYYA, P. K., & PATRA, H. 1968. *Direct current geoelectric sounding: principles and interpretation*. Elsevier Pub. Co.

BLASCHEK, R. 2006. *Aspekte der Inversion von Daten der spektralen induzierten Polarisation*. Ph.D. thesis, Technische Universität Braunschweig.

BLEIL, D. F. 1953. Induced polarization: A method of geophysical prospecting. *Geophysics*, **18**(3), 636–661.

COGGON, J. 1971. Electromagnetic and electrical modeling by the finite element method. *Geophysics*, **36**(1), 132–155.

COLE, K. S., & COLE, R. H. 1941. Dispersion and absorption in dielectrics I. Alternating current characteristics. *The Journal of Chemical Physics*, **9**(4), 341–351.

CONSTABLE, S. C. 1987. Occam's inversion: A practical algorithm for generating smooth models from electromagnetic sounding data. *Geophysics*, **52**(3), 289–289.

COURANT, R., & HILBERT, D. 1924. *Methoden der mathematischen Physik, Volume 1*. Verlag von Justus Springer, Berlin.

COURANT, R., *et al.*. 1943. Variational methods for the solution of problems of equilibrium and vibrations. *Bull. Amer. Math. Soc*, **49**(1), 1–23.

DAKHNOV, V. N., LATISHOVA, G., & RYAPOLOV, A. 1952. Well logging by means of induced polarization (electrolytic logging) (translated by Keller, G. V.). *Promislovaya Geofizika*, 46–82.

FRIEDEL, S. 2000. *Über die Abbildungseigenschaften der geoelektrischen Impedanztomographie unter Berücksichtigung von endlicher Anzahl und endlicher Genauigkeit der Messdaten*. Ph.D. thesis, Universität Leipzig, Fakultät für Physik und Geowissenschaften.

GREENHALGH, S., ZHOU, B., GREENHALGH, M., MARESCOT, L., & WIESE, T. 2009. Explicit expressions for the Fréchet derivatives in 3D anisotropic resistivity inversion. *Geophysics*, **74**(3), F31–F43.

GREENHALGH, S., WIESE, T., & MARESCOT, L. 2010. Comparison of dc sensitivity patterns for anisotropic and isotropic media. *Journal of Applied Geophysics*, **70**(2), 103 – 112.

GÜNTHER, T., RÜCKER, C., & SPITZER, K. 2006. Three-dimensional modelling and inversion of DC resistivity data incorporating topography - II. inversion. *Geophysical Journal International*, **166**(2), 506–517.

HART, D., & RUDMAN, A. J. 1997. Least-squares fit of an ellipse to anisotropic polar data: Application to azimuthal resistivity surveys in karst regions. *Computers & Geosciences*, **23**(2), 189 – 194.

HERWANGER, J., PAIN, C., BINLEY, A., DE OLIVEIRA, C., & WORTHINGTON, M. 2004. Anisotropic resistivity tomography. *Geophysical Journal International*, **158**(2), 409–425.

HILL, D. 1972. A laboratory investigation of electrical anisotropy in Precambrian rocks. *Geophysics*, **37**(6), 1022–1038.

HÖRDT, A., BLASCHEK, R., KEMNA, A., & ZISSER, N. 2007. Hydraulic conductivity estimation from induced polarisation data at the field scale — the Krauthausen case history. *Journal of Applied Geophysics*, **62**(1), 33–46.

J. D. KLEIN, P. R. M. 1997. The petrophysics of electrically anisotropic reservoirs. *Society of Petrophysicists and Well-Log Analysts*.

JACKSON, J. D. 2006. *Klassische Elektrodynamik*. Walter de Gruyter.

JOHNSON, T. C., VERSTEEG, R. J., WARD, A., DAY-LEWIS, F. D., & REVIL, A. 2010. Improved hydrogeophysical characterization and monitoring through parallel modeling and inversion of time-domain resistivity and induced-polarization data. *Geophysics*, **75**(4), WA27–WA41.

JUPP, D. L. B., & VOZOFF, K. 1975. Stable iterative methods for the inversion of geophysical data. *Geophysical Journal International*, **42**(3), 957–976.

KARAOULIS, M., REVIL, A., WERKEMA, D., MINSLEY, B., WOODRUFF, W., & KEMNA, A. 2011. Time-lapse three-dimensional inversion of complex conductivity data using an active time constrained (ATC) approach. *Geophysical Journal International*, **187**(1), 237–251.

KELLER, G., & FRISCHKNECHT, F. 1966. *Electrical Methods in Geophysical Prospecting*. First edn. Pergamon Press Inc.

KEMNA, A. 1995. *Tomographische Inversion des spezifischen Widerstandes in der Geoelektrik*. Diploma thesis, Universität zu Köln.

KEMNA, A. 2000. *Tomographic Inversion of Complex Resistivity - Theory and Application*. Ph.D. thesis, Ruhr-Universität Bochum.

KEMNA, A., & BINLEY, A. 1996. Complex electrical resistivity tomography for contaminant plume delineation. *Pages 196–199 of: Proceedings of the 2nd meeting on environmental and engineering geophysics*.

KEMNA, A., BINLEY, A. M., & SLATER, L. 2004. Cross-borehole IP imaging for engineering and environmental applications. *Geophysics*, **69**(1), 97–107.

KENKEL, J. 2011. *2D-SIP-Modellierung mit anisotropen Widerständen*. Diploma thesis, Technische Universität Braunschweig.

KENKEL, J., & KEMNA, A. 2017. Sensitivity of 2-d complex resistivity measurements to subsurface anisotropy. *Geophysical Journal International*, **208**(2), 1043–1057.

KENKEL, J., HÖRDT, A., & KEMNA, A. 2012. 2D modelling of induced polarization data with anisotropic complex conductivities. *Near Surface Geophysics*, **10**(6), 533–544.

KNÖDEL, K. 2005. *Geophysik*. Springer-Verlag, Berlin.

LABRECQUE, D. J., MILETTO, M., DAILY, W., RAMIREZ, A., & OWEN, E. 1996. The effects of noise on Occam's inversion of resistivity tomography data. *Geophysics*, **61**(2), 538–548.

LOKE, M., DAHLIN, T., & RUCKER, D. 2014. Smoothness-constrained time-lapse inversion of data from 3D resistivity surveys. *Near Surface Geophysics*, **12**(1), 5–24.

MARSHALL, D. J., & MADDEN, T. R. 1959. Induced polarization, a study of its causes. *Geophysics*, **24**(4), 790–816.

MCGILLIVRAY, P., & OLDENBURG, D. 1990. Methods for calculating Fréchet derivatives and sensitivities for the non-linear inverse problem: A comparative study. *Geophysical Prospecting*, **38**(5), 499–524.

MOYSEY, S. M., & LIU, Z. 2012. Can the onset of macropore flow be detected using electrical resistivity measurements? *Soil Science Society of America Journal*, **76**(1), 10–17.

NGUYEN, F., GARAMBOIS, S., CHARDON, D., HERMITTE, D., BELLIER, O., & JONGMANS, D. 2007. Subsurface electrical imaging of anisotropic formations affected by a slow active reverse fault, Provence, France. *Journal of Applied Geophysics*, **62**, 338 – 353.

ORISTAGLIO, M., & WORTHINGTON, M. 1980. Inversion of surface AND borehole electromagnetic data for two-dimensional electrical conductivity models. *Geophysical Prospecting*, **28**(4), 633–657.

PAIN, C. C., HERWANGER, J. V., SAUNDERS, J. H., WORTHINGTON, M. H., & DE OLIVEIRA, C. R. 2003. Anisotropic resistivity inversion. *Inverse Problems*, **19**(5), 1081.

PARASNIS, D. 1986. *Principles of applied geophysics*. 4th edition edn. Cambridge University Press.

PARKER, R. L. 1984. The inverse problem of resistivity sounding. *Geophysics*, **49**(12), 2143–2158.

PELTON, W., RIJO, L., & SWIFT JR, C. 1978a. Inversion of two-dimensional resistivity and induced-polarization data. *Geophysics*, **43**(4), 788–803.

PELTON, W., WARD, S., HALLOF, P., SILL, W., & NELSON, P. H. 1978b. Mineral discrimination and removal of inductive coupling with multifrequency IP. *Geophysics*, **43**(3), 588–609.

PORTNIAGUINE, O., & ZHDANOV, M. S. 1999. Focusing geophysical inversion images. *Geophysics*, **64**(3), 874–887.

RADIC RESEARCH. 2016. *SIP256C*. URL `http://www.radic-research.de/Instruments.htm`, [Online; accessed 30-December-2016].

RODI, W. L. 1976. A technique for improving the accuracy of finite element solutions for magnetotelluric data. *Geophysical Journal International*, **44**(2), 483–506.

SASAKI, Y. 1989. Two-dimensional joint inversion of magnetotelluric and dipole-dipole resistivity data. *Geophysics*, **54**(2), 254–262.

SCHWARZ, H. R. 1991a. *FORTRAN-Programme zur Methode der finiten Elemente*. Springer.

SCHWARZ, H. R. 1991b. *Methode der finiten Elemente*. Teubner Studienbücher, Stuttgart.

TELFORD, W. M., SHERIFF, R. E., & GELDART, L. P. 1990. *Applied Geophysics*. Second edn. Cambridge University Press.

TIKHONOV, A., & ARSENIN, V. Y. 1977. *Solution of ill-posed problems*. Winston & Sons, Washington.

TIPLER, P. A., M, B., FLIEGNER, D., JEDYNAK, A., MARTER, B., MARX, M., MEIGEN, T., PAUL, W., & ZILLGITT, M. 2000. *Physik*. Spektrum Akademischer Verlag.

TRIPP, A., HOHMANN, G., & SWIFT JR, C. 1984. Two-dimensional resistivity inversion. *Geophysics*, **49**(10), 1708–1717.

WALLACE, P. R. 1947. The band theory of graphite. *Physical Review*, **71**(9), 622.

WARD, S., RYU, J., GLENN, W., HOHMANN, G., DEY, A., & SMITH, B. 1974. Electromagnetic methods in conductive terranes. *Geoexploration*, **12**(2), 121 – 183.

WINCHEN, T., KEMNA, A., VEREECKEN, H., & HUISMAN, J. A. 2009. Characterization of bimodal facies distributions using effective anisotropic complex resistivity: A 2D numerical study based on Cole-Cole models. *Geophysics*, **74**(3), A19–A22.

WONG, J., & STRANGWAY, D. W. 1981. Induced polarization in disseminated sulfide ores containing elongated mineralization. *Geophysics*, **46**(9), 1258–1268.

YIN, C., & WEIDELT, P. 1999. Geoelectrical fields in a layered earth with arbitrary anisotropy. *Geophysics*, **64**(2), 426–434.

ZISSER, N., & NOVER, G. 2009. Anisotropy of permeability and complex resistivity of tight sandstones subjected to hydrostatic pressure. *Journal of Applied Geophysics*, **68**(3), 356–370.

ZOHDY, A. A., ANDERSON, L., & MUFFLER, L. 1973. Resistivity, self-potential, and induced-polarization surveys of a vapor-dominated geothermal system. *Geophysics*, **38**(6), 1130–1144.

Publikationsliste

Publikationen

Kenkel, J., Kemna, A., *Sensitivity of 2-D complex resistivity measurements to subsurface anisotropy*, Geophysical Journal International 2016 208 (2), Seiten 1043-1057

Kenkel, J., Hördt, A., Kemna, A., *2D modelling of induced polarization data with anisotropic complex conductivities*, Near Surface Geophysics 10, 2012, Seiten 533-544

Kenkel, J., Hördt, A., Kemna, A., *2D-SIP-Modellierung mit anisotropen Widerständen*, Kolloquiumsband des Kolloquiums elektromagnetische Tiefenforschung (EMTF) in Potsdam, 2009

Lupi, M., Suski Ricci, B., Kenkel, J., Ricci, T., Fuchs, F., Miller, S. A., Kemna, A., *Subsurface fluid distribution and possible seismic precursory signal at the Salse di Nirano mud volcanic field, Italy*. Geophysical Journal International 2015 204, Seiten 907-917

Vorträge

Bücker, M., Kenkel, J., Hördt, A., Hanstein, T., *Einfluss von Bathymetrie auf marine CSEM-Messungen im Zeitbereich*, Präsentation auf der Tagung der Deutschen Geophysikalischen Gesellschaft (DGG), Kiel, 2009

Kenkel, J., *2D-SIP-Modellierung mit anisotropen Leitfähigkeiten*, Präsentation auf der Tagung der Deutschen Geophysikalischen Gesellschaft (DGG), Bochum, 2010

Kenkel, J., Hördt, A., *Zweidimensionale SIP-Modellierung mit anisotroper Leitfähigkeit*, Poster beim Kolloquium elektromagnetische Tiefenforschung (EMTF) in Potsdam, 2009

Kenkel, J., Kemna, A., *Anisotropie in der 2D-Modellierung komplexer Widerstände*, Poster beim Kolloquium elektromagnetische Tiefenforschung (EMTF) in Bucha, 2011

Kenkel, J., Martin, R., Kemna, A., *2D modelling of IP data with anisotropic complex conductivities*, Präsentation auf der Tagung der Deutschen Geophysikalischen Gesellschaft (DGG), Hamburg, 2012

Kenkel, J., Martin, R., Kemna, A., *2D inversion of induced polarization data with anisotropic complex conductivities*, Poster beim HOBE-Meeting (HOBE – Center for Hydrology. hobecenter.dk), 2012

Kenkel, J., Martin, R., Kemna, A., *Anisotropic 2D Modelling of Induced Polarization Data*, Poster beim Hydrogeophysics Workshop in Boise, USA, 2012

Kenkel, J., Kemna, A., *Anisotrope Inversion von Daten der induzierten Polarisation*, Präsentation auf der Tagung der Deutschen Geo-

physikalischen Gesellschaft (DGG), Leipzig, 2013

Kenkel, J., Martin, R., Kemna, A., *Anisotropic Inversion of Spectral Induced Polarization (SIP) Signatures*, Präsentation und Extended Abstract auf der Tagung der European Association of Geoscientists and Engineers (EAGE), Bochum, 2013

Kenkel, J., Kemna, A., *Anisotropic Inversion of Induced Polarization (IP) Data*, Poster auf der Tagung der Deutschen Geophysikalischen Gesellschaft (DGG), Karlsruhe, 2014

Kenkel, J., Kemna, A., *Anisotropic complex conductivity inversion*, Poster und Extended Abstract beim IP Workshop, Ile d'Oleron, 2014

Kenkel, J., Kemna, A., *Sensitivity of IP Surface Measurements to Subsurface Anisotropy*, Poster auf der Tagung der Deutschen Geophysikalischen Gesellschaft (DGG), Hannover, 2015